

NMR Investigations and Feedback Estimation of Ergotropy : Applications in Quantum Battery and Entanglement Certification

विद्या वाचस्पति की
उपाधि की अपेक्षाओं की आंशिक पूर्ति में प्रस्तुत शोध प्रबंध

A thesis submitted in partial fulfillment of the requirements of
the degree of Doctor of Philosophy

द्वारा / By
जितेन्द्र जोशी / Jitendra Joshi

पंजीकरण सं. / Registration No.: 20193699

शोध प्रबंध पर्यवेक्षक / Thesis Supervisor:
प्रोफ. टी.एस.महेश / Prof. T. S. Mahesh



भारतीय विज्ञान शिक्षा एवं अनुसंधान संस्थान पुणे
INDIAN INSTITUTE OF SCIENCE EDUCATION AND RESEARCH
PUNE

2025

Certificate

Certified that the work incorporated in the thesis entitled “**NMR Investigations and Feedback Estimation of Ergotropy : Applications in Quantum Battery and Entanglement Certification**” submitted by **Jitendra Joshi** was carried out by the candidate, under my supervision. The work presented here or any part of it has not been included in any other thesis submitted previously for the award of any degree or diploma from any other university or institution.

Date: June 24, 2025



Prof. T.S. Mahesh

(Supervisor)

Declaration

Name of Student: Jitendra Joshi

Reg. No.: 20193699

Thesis Supervisor: Prof. T.S. Mahesh

Department: Physics

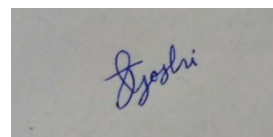
Date of joining program: August 1, 2019

Date of Pre-Synopsis Seminar: Nov 29, 2024

Title of Thesis: NMR Investigations and Feedback Estimation of Ergotropy : Applications in Quantum Battery and Entanglement Certification

I declare that this written submission represents my ideas in my own words and where others ideas have been included, I have adequately cited and referenced the original sources. I also declare that I have adhered to all principles of academic honesty and integrity and have not misrepresented or fabricated or falsified any idea/data/fact/source in my submission. I understand that violation of the above will be cause for disciplinary action by the Institute and can also evoke penal action from the sources which have thus not been properly cited or from whom proper permission has not been taken when needed.

Date: June 24, 2025



Jitendra Joshi
(20193699)

To my family

Acknowledgments

I want to express my gratitude to everyone who has helped make my PhD feasible as it nears its conclusion. I want to start by expressing my gratitude to Prof. T. S. Mahesh, my supervisor, for all of his help and advice during this period. His extensive knowledge of quantum information processing and NMR, along with his general enthusiasm for research and education, have served as a consistent source of motivation. Not only does he assist students when they are completely stuck, but he is always open to learning, sharing, and accepting new ideas.

I would next like to express my gratitude to Dr. B. Prasanna Venkatesh and Dr. Shouvik Datta, who have served on my research advisory committee, for their insightful critiques, talks, and advice over the years. It has been really enlightening to work with collaborators Drs. Manik Banik and Mir Alimuddin, particularly with Dr. Mir, who provided me with extensive understanding of the Many-Body entanglement theory. I had no experience with NMR when I started my PhD. I would want to express my gratitude to my lab seniors, Dr. V. R. Krithika, Dr. Rupak Bhattacharya, Dr. Priya Batra, and Dr. Soahm Pal, for their assistance in getting me started and for always being accessible to help with experiments or conceptual comprehension. I was directed through my first NMR experiments and shown how to use the spectrometer by Dr. Krithika, Prof. Mahesh, and Dr. Sandeep Mishra. I also want to express my gratitude to Arijit, Conan, Vishal, Harshanth, Deepesh, Hari, and Vishal, my other group members, for fostering such a vibrant and intellectually engaging environment. My deepest appreciation goes out to Mr. Nitin Dalvi, Mr. Karan and Dr. Sandeep Mishra, the technical personnel, for always keeping the spectrometers operating at peak efficiency and for their assistance with any technical problems. Additionally, I would want to thank Mr. Prabhakar and Mrs. Dhanashree, the department staff, for frequently going above and beyond to assist us students with administrative work.

My family's encouragement and support throughout have my eternal gratitude. I would want to sincerely thank the many philosophers, whose lives and works have offered solace and inspiration during some of the most struggling moments. Lastly, I acknowledge the financial support provided by CSIR, India and I-HUB, which made this research possible.

Abstract

Quantum-level energy storage and usage is gaining significant interest among scientific communities with a newly introduced concept in quantum thermodynamics, namely ergotropy. Ergotropy quantifies the maximum amount of work that can be extracted unitarily from an energy-storing quantum device. Ergotropy is a core concept used in quantum batteries, and since it can help certify entanglement, it connects quantum thermodynamics with quantum information. With long coherence times, strong spin-spin interactions, and precise and intricate control over quantum dynamics, the nuclear spin qubits offer an excellent testbed for studying such quantum concepts.

By manipulating qubit energy across different parts of star-topology spin systems, we experimentally realize quantum batteries, monitor their ergotropy, establish the quantum speedup, achieve asymptotic charging, and demonstrate a charger-battery-load circuit. We show that measuring specific variants of ergotropy can help certify bipartite entanglement in multiqubit systems without explicitly knowing their quantum states. In particular, the criteria depend on the difference in optimal global and local works extractable from an isolated quantum system under global and local interactions, respectively. As a proof of principle, we demonstrate entanglement certification on nuclear spin registers with up to 10 qubits.

Finally, we propose and experimentally demonstrate a feedback-based algorithm (FQErgo) for estimating ergotropy. This method also transforms an arbitrary initial state to its passive state, which allows no further unitary work extraction, providing a practical way for unitary energy extraction and for preparing passive states. By numerically analyzing FQErgo on random initial states, we confirm the successful preparation of passive states and estimation of ergotropy, even in the presence of drive errors. Finally, we implement FQErgo on two- and three-qubit NMR registers, prepare their passive states, and accurately estimate their ergotropy.

Synopsis

We report on the use of nuclear spins in NMR architecture to research quantum battery and many body entanglement in this thesis. There are four chapters in the thesis, each of which is briefly summarised below.

Chapter 1 – Introduction

We start this chapter by introducing the fundamentals of quantum information processing, starting with qubits, quantum gates, density operators, and ending with measurements. Further, we describe quantum correlations and a newly introduced concept, ergotropy. Finally, we focus on the experimental setting by describing the NMR experimental test bed and its potential applications to quantum information processing problems before rounding up this chapter.

Chapter 2 – Nuclear spins as quantum battery

In this chapter, we experimentally investigate various aspects of quantum batteries with the help of nuclear spin systems in a star-topology configuration. We first carry out numerical analysis to study how charging a quantum battery depends on the relative purity factors of charger and battery spins. By experimentally characterizing the state of the battery spin undergoing charging, we estimate the battery energy as well as the ergotropy, the maximum amount of work that is unitarily available for extraction. The experimental results thus obtained establish the quantum advantage in charging the quantum battery. We propose using the quantum advantage, gained via quantum correlations among chargers and the battery, as a measure for estimating the size of the correlated cluster. We develop a simple iterative method to realize asymptotic charging that avoids the oscillatory behavior of charging and discharging. Finally, we introduce a load spin and realize a charger-battery-load circuit and experimentally demonstrate battery energy consumption after varying the duration of battery storage, for up to 2 min.

Chapter 3 – Verification of many-body entanglement in NMR

In this chapter, we propose a set of entanglement criteria for multi-qubit systems that can be easily verified by measuring certain thermodynamic quantities. In particular, the criteria depend on the difference in optimal global and local works extractable from an isolated quantum system under global and local interactions, respectively. As a proof of principle, we demonstrate the proposed scheme on nuclear spin registers of up to 10 qubits using the Nuclear Magnetic Resonance architecture. We prepare noisy Bell-diagonal state and noisy Greenberger-Horne-Zeilinger class of states in star-topology systems and certify their entanglement through our thermodynamic criteria. Along the same line, we also propose an entanglement certification scheme in many-body systems when only partial or even no knowledge about the state is available.

Chapter 4 – Maximal work extraction from nuclear spins using FQErgo

In this chapter, we propose and experimentally demonstrate a feedback-based algorithm (FQErgo) for estimating ergotropy. This method also transforms an arbitrary initial state to its passive state, which allows no further unitary work extraction. FQErgo applies drive fields whose strengths are iteratively adjusted via certain expectation values, conveniently read using a single probe qubit. Thus, FQErgo provides a practical way for unitary energy extraction and for preparing passive states. By numerically analyzing FQErgo on random initial states, we confirm the successful preparation of passive states and estimation of ergotropy, even in the presence of drive errors. Finally, we implement FQErgo on two- and three-qubit NMR registers, prepare their passive states, and accurately estimate their ergotropy.

Chapter 5 – Closing Remarks and Outlook

In this chapter, we conclude the thesis by summarizing key findings and discussing future research directions.

List of Publications

1. **Jitendra Joshi** and T. S. Mahesh, *Experimental investigation of a quantum battery using star-topology NMR spin systems*, [Phys. Rev. A 106, 042601 \(2022\)](#). [Thesis Chapter 2].
2. **Jitendra Joshi**, Mir Alimuddin, T S Mahesh and Manik banik, *Experimental verification of many-body entanglement using thermodynamic quantities*, [Phys. Rev. A 109, L020403\(2024\)](#). [Thesis Chapter 3].
3. **Jitendra Joshi** and T S Mahesh, *Maximal work extraction unitarily from an unknown quantum state: Ergotropy estimation via feedback experiments*, [arXiv:2409.04087 \(2024\)](#). [Thesis Chapter 4].

Contents

Certificate	iii
Declaration	i
Acknowledgments	v
Abstract	vii
Synopsis	ix
List of Publications	xi
1 Introduction	1
1.1 Quantum information processing	3
1.1.1 Qubits	3
1.1.1.1 One-qubit system	3
1.1.1.2 N-qubit system	4
1.1.2 Quantum logic gates	5
1.1.2.1 One qubit gates as rotation	5
1.1.2.2 N-qubit gates	6
1.1.3 Density operator	7
1.1.3.1 Mixed states	7
1.1.3.2 Bloch-sphere representation for mixed states	8
1.1.3.3 Density operator formalism	8
1.1.3.4 Elements of density operator	9

1.1.3.5	Reduced density operator	10
1.1.4	Measurement	10
1.1.4.1	Projective measurements	11
1.1.4.2	POVM	11
1.2	Quantum correlations	12
1.2.1	Quantum discord	12
1.2.2	Entanglement	15
1.2.2.1	Entropy as an entanglement measure	15
1.2.2.2	Negativity as an entanglement measure	16
1.3	Ergotropy	16
1.3.1	Passive states	18
1.3.2	Ergotropy gap	19
1.4	NMR experimental setup	20
1.4.1	Nuclear spin as a qubit	20
1.4.1.1	Qubit interactions	23
1.4.1.2	Relaxation	24
1.4.1.3	Chemical shift	25
1.4.1.4	PFG (Pulsed Field Gradient)	25
1.5	NMR based quantum information processing	26
1.5.1	Qubit manipulation	26
1.5.2	NMR Quantum gates	27
1.5.2.1	Single qubit gates	27
1.5.2.2	Multi-qubit gates	29
1.5.3	PPS (Pseudo-Pure States)	29
1.5.4	Measurement in NMR	31
1.6	Thesis Summary	33
2	Nuclear spins as quantum battery	34
2.1	Introduction	35
2.2	Objectives	36
2.3	Theory	36

2.3.1	Quantum Battery	36
2.3.2	star-topology network	40
2.4	Experiments	43
2.4.1	Establishing quantum advantage	43
2.4.2	Determining size of the correlated cluster	46
2.4.3	Asymptotic charging	47
2.4.4	Quantum Charger-Battery-Load (QCBL) Circuit	48
2.4.5	Effects of Dissipation on Quantum Battery Performance	50
2.5	Summary and outlook	51
3	Verification of many-body entanglement in NMR	53
3.1	Introduction	53
3.2	Objectives	55
3.3	Theory	55
3.3.1	Majorization based entanglement criteria	55
3.3.2	A: State dependent thermodynamic criteria of entanglement	57
3.3.3	B: State independent thermodynamic criteria of entanglement	61
3.3.3.1	Two-qubit system	62
3.3.3.2	Three-qubit system	63
3.3.3.3	Ten-qubit system	66
3.4	Experiments	68
3.4.1	Experiment I: Two-qubit Bell diagonal states	68
3.4.2	Experiment I-b: Two-qubit Werner state	75
3.4.3	Experiment II: Multi-qubit systems	78
3.4.3.1	Three-qubit system	81
3.4.3.2	Ten-qubit system	82
3.4.4	Experiment III: Global vs Global-Local Separability bounds	82
3.5	Conclusions and outlook	86
4	Maximal work extraction from nuclear spins using FQErgo	88
4.1	Introduction	88

4.1.1	Objectives	90
4.2	Theory	90
4.2.1	Unitary extraction of work, passive state, and ergotropy	90
4.2.2	FQErgo: A feedback algorithm for ergotropy estimation	91
4.2.3	FQErgo using a probe qubit	93
4.3	Numerical simulations	93
4.3.1	Single qubit system	93
4.3.2	Two qubit system	96
4.3.3	Speed analysis	97
4.4	Experiments	98
4.4.1	Single-qubit ergotropy	98
4.4.2	Two-qubit ergotropy	100
4.5	Summary and outlook	103
5	Closing Remarks and Outlook	115
	References	119

CHAPTER 1

Introduction

Laser technology and transistors were pivotal in sparking the transformative advancements of the digital era, revolutionizing electronics and paving the way for innovations like computers, communication devices, and modern cell phones. These technologies enabled rapid development in a variety of fields, including entertainment, business, and education, fundamentally changing how we interact with the world around us. However, when it comes to quantum systems, the complexity of their underlying physics presents significant challenges [1]. Even the most powerful supercomputers in existence today struggle to replicate many of the basic quantum mechanical phenomena observed in nature, which are essential to understanding the behavior of particles at the atomic and subatomic levels. This limitation is a significant barrier to advancements in quantum mechanics, which has the potential to revolutionize many aspects of technology and science.

In the 1980s, two pioneering scientists, Yuri Manin and Richard Feynman, proposed a groundbreaking idea about the potential of quantum simulators [1]. They suggested that using a quantum system to simulate another quantum system would be far more efficient than relying on traditional Turing computers. The immense complexity of quantum phenomena meant that simulating these processes with classical computational methods would require an impractical amount of time and resources. This insight led to the notion of quantum computers, which could, in theory, use the principles of quantum mechanics to solve problems that are otherwise intractable for classical computers. This idea was revolutionary, and over the next several decades, it gained significant traction.

By the 1990s, researchers began to explore the vast potential of quantum simulators in more detail. A number of notable works emerged, such as the Deutsch-Jozsa algorithm [2], which provided a way to determine whether an n -bit function was constant or balanced, and Grover's search algorithm [3], which greatly improved the efficiency of searching an unstructured database. Ben-

nett and Brassard's creation of the BB84 quantum cryptography protocol [4] also introduced a secure method of communication based on the principles of quantum mechanics, which has profound implications for data security. Meanwhile, Shor's algorithm [5] demonstrated that quantum computers could potentially factor large numbers in polynomial time, which has significant applications in cryptography and data encryption.

In 1997, quantum computing reached a major milestone with the first experimental realization of quantum computing, achieved through nuclear magnetic resonance (NMR) experiments led by Cory et al. [6] and Gershenfeld et al. [7]. This success opened the door to a new era of experimental quantum computing, which has since expanded into several promising areas. Quantum computing designs now span across diverse approaches, including photonic systems [8–11], ultracold atoms [12–14], quantum dots [15–17], trapped ions [18, 19], and superconducting qubits [20, 21]. These designs all leverage different aspects of quantum mechanics to perform computations that classical computers cannot, offering exciting possibilities for the future of computation and technology.

At present, the field of quantum computing is advancing rapidly, with significant investments from major tech companies such as IBM [22], Google [23], and several emerging startups like D-Wave, IonQ, and Rigetti [24–27]. The race to develop practical quantum computers is on, and these companies are pushing the boundaries of what is possible with current quantum technologies. The second quantum revolution is already well underway, and its impact on both science and industry is likely to be far-reaching. As quantum technologies become more refined and accessible, industries ranging from pharmaceuticals to energy could benefit from advancements that were once thought to be decades away. The integration of quantum computing with other technologies, such as machine learning and artificial intelligence, could also yield transformative results. Quantum systems could offer unprecedented levels of speed and efficiency in solving complex problems, driving innovation across virtually all sectors of society.

The following sections will explore the fundamental principles of quantum information processing in detail. Additionally, they will discuss how these principles can be integrated with nuclear magnetic resonance (NMR) architecture to further advance the capabilities of quantum systems.

1.1 Quantum information processing

In this section, we briefly look into the building blocks of quantum information.

1.1.1 Qubits

1.1.1.1 One-qubit system

A binary digit, or bit with value 0 or 1, is the fundamental unit of classical information. This may be physically achieved in any system that has two separate states, such as two voltage nodes, two different operating regions of a transistor, or the alignment of a magnetic material. In classical computing, these bits are subjected to logical operations, which result in a string of bit values as the output. Qubits, the equivalent of bits in quantum mechanics, are basically represented by two-level quantum systems that can be realised in a variety of ways, including spin states of electrons or nuclei or polarisation states of photons. The ground state of a two-level system $|g\rangle$ or $|0\rangle$ corresponds to logical 0 and the excited state $|e\rangle$ or $|1\rangle$ corresponds to logical 1. Surprisingly, qubits may exist in both states simultaneously, resulting in a strange quantum phenomenon called quantum superposition, which is impossible to explain classically. The general state of a qubit in the two-dimensional Hilbert space can hence be described in terms of the superposition of orthogonal basis states $|0\rangle$ and $|1\rangle$ as [28]

$$|\psi\rangle = c_1|0\rangle + c_2|1\rangle, \quad (1.1)$$

where the complex coefficients $\{c_1, c_2\}$ must satisfy normalization $|c_1|^2 + |c_2|^2 = 1$. The qubit is precisely in state $|0\rangle$ for $c_1 = 1$, state $|1\rangle$ for $c_2 = 1$, and in a superposition for $c_1 \neq 0 \neq c_2$. Often called the computational basis states, the states $|0\rangle$ and $|1\rangle$ can be expressed in matrix form as $|0\rangle = \begin{bmatrix} 1 \\ 0 \end{bmatrix}$ and $|1\rangle = \begin{bmatrix} 0 \\ 1 \end{bmatrix}$, producing a general state in the form $|\psi\rangle = \begin{bmatrix} c_1 \\ c_2 \end{bmatrix}$.

By equivalently expressing Eq. 1.1 in the form

$$|\psi\rangle = \cos(\theta/2)|0\rangle + e^{i\phi} \sin(\theta/2)|1\rangle, \quad (1.2)$$

which geometrically represents a point on a sphere of unit radius known as the Bloch sphere,

allows us to represent a generic single qubit state as shown in Fig. 1.1. The polar and azimuthal angles, $\theta \in [0, \pi]$ and $\phi \in [0, 2\pi]$, respectively, cover all locations on the sphere with $c_1 = \cos(\theta/2)$ and $c_2 = e^{i\phi} \sin(\theta/2)$ clearly normalizing the state in Eq. 1.2.

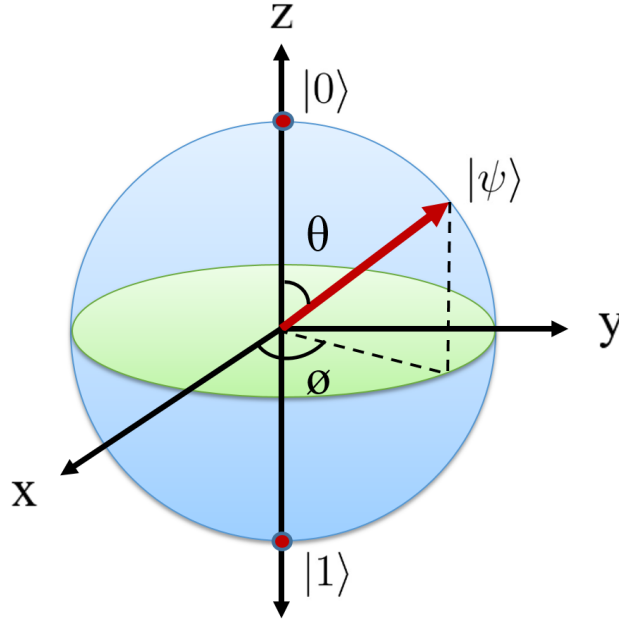


Figure 1.1: Bloch sphere representation of a qubit in a state $|\psi\rangle$.

1.1.1.2 N-qubit system

Most general N-qubit pure state can be written as

$$|\Psi\rangle = \sum_j c_j |\phi_{1j}\rangle \otimes |\phi_{2j}\rangle \otimes \dots \otimes |\phi_{Nj}\rangle \quad (1.3)$$

where $|\phi_{ij}\rangle$ refers to i th qubit in j th term of the superposition, and c_j are the complex coefficient normalized to unity. For instance, if we consider $|\phi_{ij}\rangle$ to be only $\{|0\rangle, |1\rangle\}$ then the N-qubit system state can be created from a tensor product of single-qubit basis states as $|\phi\rangle = \prod_N \otimes |i\rangle$ for $i = 0, 1$, and the related Hilbert space dimension grows exponentially as 2^N as the number of qubits N rises. For example, $|0\rangle^{\otimes N}$ yields the N-qubit composite state $|00\dots 0\rangle$. Thus extending the notion of Eq. 1.1 one can write

$$|\Psi\rangle = c_1 |00\dots 0\rangle + c_2 |00\dots 1\rangle + c_3 |00\dots 1\dots 0\rangle + \dots + c_N |10\dots 0\rangle + \dots + c_{2^N} |11\dots 1\rangle, \quad (1.4)$$

where the states $|\phi\rangle = \prod_N \otimes |i\rangle$ for $i = 0, 1$ span the basis and coefficients fulfil the condition $\sum_{i=1}^{2^N} |c_i|^2 = 1$. Like Bloch sphere for the single qubit case it is very difficult to envision such pure states of N-qubit system geometrically.

1.1.2 Quantum logic gates

In conventional technologies, physical devices called logic gates—such as NOT, OR, NOR, and so forth—are used to process information. Quantum gates are used in a similar way to process information in quantum technology. Unitary operators working on qubits to change an initial state into a desired end state are known as quantum gates. If a qubit starts in an initial state $|\psi\rangle$, then the application of the unitary operator U transfers it to

$$|\psi'\rangle = U|\psi\rangle \quad (1.5)$$

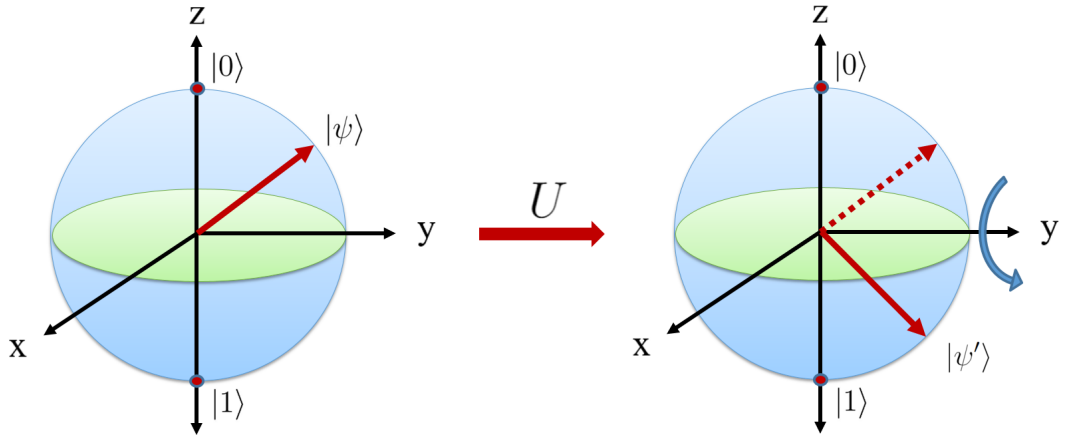


Figure 1.2: Bloch sphere representation of a unitary operation on a single qubit in a state $|\psi\rangle$.

Some basic single and N-qubit gates are discussed below.

1.1.2.1 One qubit gates as rotation

The transformation of a one-qubit state from $|\psi\rangle = c_1|0\rangle + c_2|1\rangle$ to $|\psi'\rangle = c'_1|0\rangle + c'_2|1\rangle$ is nothing but a rotation in the Bloch sphere about a direction $\vec{a} = a_x\hat{x} + a_y\hat{y} + a_z\hat{z}$ by an angle θ . One can use Pauli spin matrix vector $\vec{\sigma} = \sigma_x\hat{x} + \sigma_y\hat{y} + \sigma_z\hat{z}$ to realise a general rotation operator as

$$R_{\vec{a}}(\theta) = \exp\left(\frac{-i\theta\vec{a} \cdot \vec{\sigma}}{2}\right) = \cos\left(\frac{\theta}{2}\right) \mathbb{1} - i \sin\left(\frac{\theta}{2}\right) (\vec{a} \cdot \vec{\sigma}). \quad (1.6)$$

where $\sigma_x = \begin{bmatrix} 0 & 1 \\ 1 & 0 \end{bmatrix}$, $\sigma_y = \begin{bmatrix} 0 & -i \\ i & 0 \end{bmatrix}$, and $\sigma_z = \begin{bmatrix} 1 & 0 \\ 0 & -1 \end{bmatrix}$.

For example, the rotation operator for $\theta = 180^\circ$ about the x -axis has the matrix form $R_x(\pi) = \begin{bmatrix} 0 & 1 \\ 1 & 0 \end{bmatrix}$ up to a phase factor. This operator acts as the quantum counterpart of a NOT gate, giving us the transformation $|0\rangle \rightarrow |1\rangle$ and vice-versa. Similarly, distinct transformations are produced by π rotations around the y and z axes.

The Hadamard gate

$$H = \frac{1}{\sqrt{2}} \begin{bmatrix} 1 & 1 \\ 1 & -1 \end{bmatrix} \quad (1.7)$$

which produces superposition of states as $|0\rangle \rightarrow \frac{|0\rangle+|1\rangle}{\sqrt{2}}$ and $|1\rangle \rightarrow \frac{|0\rangle-|1\rangle}{\sqrt{2}}$ and the phase gate

$$R_\phi = \begin{bmatrix} 1 & 0 \\ 0 & e^{i\phi} \end{bmatrix}. \quad (1.8)$$

which leaves $|0\rangle$ intact while selectively giving a phase to the state $|1\rangle \rightarrow e^{i\phi}|1\rangle$ are some of the important gates that are widely used for quantum operations.

1.1.2.2 N-qubit gates

N-qubit gates are operations performed simultaneously on more than one qubit. One of the most important two-qubit gates is the *controlled-not gate*, or CNOT. This gate changes the state of the target qubit (T) conditional to the state of the control qubit (C). The operation proceeds the following way: First, if the control qubit is in state $|0\rangle$, then the target qubit is unperturbed; second if the control qubit is in state $|1\rangle$, then a NOT gate is applied on the target qubit. Hence, under the action of this gate (in the computational basis), lets take our first qubit to be control and the second qubit as target, then the states $\{|00\rangle, |01\rangle\}$ remain unchanged, while $|10\rangle \rightarrow |11\rangle$ and $|11\rangle \rightarrow |10\rangle$. The matrix form of this gate, where the first qubit is the control qubit and second

qubit is the target, is given by

$$U_{\text{CNOT}} = \begin{bmatrix} 1 & 0 & 0 & 0 \\ 0 & 1 & 0 & 0 \\ 0 & 0 & 0 & 1 \\ 0 & 0 & 1 & 0 \end{bmatrix}. \quad (1.9)$$

Any Hamiltonian evolution may be described as a combination of gates in the universal set formed by single qubit gates and the two-qubit CNOT gate [28]. TOFFOLI and SWAP gates are two other often used multi-qubit gates [28].

1.1.3 Density operator

1.1.3.1 Mixed states

Till now we were dealing with a single state vector of the form $|\Psi\rangle = c_1|00\dots 0\rangle + c_2|00\dots 1\rangle + \dots + c_{2^N}|11\dots 1\rangle$. If all systems in an ensemble are prepared in the same way and in the same condition, they are said to be in a pure state $|\Psi\rangle$. Conversely, if the ensemble represents a statistical mixture of distinct pure states, then no one state vector $|\Psi\rangle$ can adequately characterise the state of the entire system. Any measurement in such a combination will have a different result throughout the whole ensemble depending on which sub-ensemble is being sampled. In order to describe such a system, it is necessary to use the density operator formalism, which is written as

$$\rho = \sum_i \lambda_i |\lambda_i\rangle \langle \lambda_i|, \quad (1.10)$$

where $\{|\lambda_i\rangle\}$ are pure states, and the probabilities λ_i add to 1. For example, a general mixture of a single-qubit system in the computational basis states can be given by $\rho = \lambda|0\rangle\langle 0| + (1-\lambda)|1\rangle\langle 1| + \alpha|0\rangle\langle 1| + \alpha^*|1\rangle\langle 0|$. Here, the probability of a measurement yielding outcome corresponding to $|0\rangle$ is λ and that of $|1\rangle$ is $(1-\lambda)$. It is significant to remember that a mixed state's probability distribution of measurements differs significantly from a (pure) superposition state's. Depending on the system's level of mixedness, mixed states for a single qubit can reside at any radius from the Bloch sphere's surface to its core. The identity operator $\mathbb{1}/2^N$, which is located at the centre of the N -dimensional hypersphere (for multi-qubit systems) or the Bloch sphere (for single qubit systems), indicates the maximum mixed state of N qubits.

1.1.3.2 Bloch-sphere representation for mixed states

A general single-qubit state, whether pure or mixed, can be written in terms of the density matrix

$$\rho = \frac{1}{2}(I + \vec{r} \cdot \vec{\sigma}),$$

where $\vec{\sigma} = (\sigma_x, \sigma_y, \sigma_z)$ are the Pauli matrices and $\vec{r} = (r_x, r_y, r_z)$ is the Bloch vector

- Pure states satisfy $\|\vec{r}\| = 1$, placing them on the *surface* of the Bloch sphere.
- Mixed states satisfy $\|\vec{r}\| < 1$, so they correspond to points inside the sphere—forming the *Bloch ball*

The *purity* of the state is quantified by

$$\text{Tr}(\rho^2) = \frac{1}{2}(1 + \|\vec{r}\|^2),$$

so that $\text{Tr}(\rho^2) = 1$ for pure states and $\text{Tr}(\rho^2) < 1$ for mixed states, with the maximally mixed state $\rho = \frac{1}{2}I$ at the center ($\|\vec{r}\| = 0$)

Geometrically, the Bloch vector \vec{r} encodes both the directional qubit structure and the degree of statistical mixture:

unitary (coherent) evolutions \rightarrow rotations of \vec{r} , non-unitary (noisy) dynamics \rightarrow shrinkage inward.

This provides a clear visual representation of decoherence and state purity in qubit dynamics where any point inside of the Bloch sphere shown in Fig. 1.1 represents a mixed state.

1.1.3.3 Density operator formalism

The development of quantum systems is frequently described and studied using the density operator formalism. For a pure state $|\psi\rangle$, a density operator or matrix is defined as

$$\rho = |\psi\rangle\langle\psi|, \tag{1.11}$$

Nevertheless, the majority of natural systems exhibit mixed states, which are statistical mixes of several pure states $\{|\lambda_i\rangle\}$, which can only be represented by density operator

$$\rho = \sum_i \lambda_i |\lambda_i\rangle \langle \lambda_i|, \text{ with } \sum_i \lambda_i = 1. \quad (1.12)$$

having following properties.

(i) $\text{tr}(\rho) = 1$ which guarantees normalization, i.e. all probabilities sum up to 1.

(ii) ρ is a positive operator with non-negative eigenvalues.

From the above, it follows that ρ is always Hermitian, i.e., $\rho^\dagger = \rho$. While $\text{tr}(\rho) = 1$ for both pure and mixed states, only pure states have $\text{tr}(\rho^2) = 1$, whereas mixed states have $\text{tr}(\rho^2) < 1$. The identity matrix $\rho = \mathbb{1}/2$ represents the maximally mixed state with $\text{tr}(\rho^2) = 1/2$. Hence $\text{tr}(\rho^2)$ is often termed as *purity* of a quantum state. The representation of the density matrix can have infinite possibilities, as it depends on the choice of the basis. For instance, take a single-qubit ensemble in the maximally mixed state $\rho = \mathbb{1}/2$. A situation like this may occur if the ensemble has equal amounts of $\{|0\rangle\langle 0|, |1\rangle\langle 1|\}$ or $\{|+\rangle\langle +|, |-\rangle\langle -|\}$, or any number of other potential combinations. Therefore, given a density matrix it is impossible to determine the ensemble distribution in a unique way.

1.1.3.4 Elements of density operator

The physical significance of density operator can be better understood by looking at the element of the density operator. For a pure state in an orthonormal basis

$$\rho_{rs} = \langle r|\rho|s\rangle = \sum_{k,l} c_k c_l^* \langle r|k\rangle \langle l|s\rangle = c_r c_s^*, \quad (1.13)$$

and for a mixed state

$$\rho_{rs} = \sum_i \lambda_i \langle r|\lambda_i\rangle \langle \lambda_i|s\rangle = \sum_i \lambda_i \sum_{k,l} c_k^i c_l^{i*} \langle r|k\rangle \langle l|s\rangle = \overline{c_r c_s^*}, \quad (1.14)$$

where $\overline{c_r c_s^*}$ denotes the ensemble average. In the eigenbasis of Hamiltonian, the diagonal element

$$\rho_{rr} = \overline{|c_r|^2} \quad (1.15)$$

represents the *population* of the state $|r\rangle$. The off-diagonal element

$$\rho_{rs} = \overline{c_r c_s^*} \quad (1.16)$$

is called *coherence*, because it indicates a coherent superposition of state $|r\rangle$ and $|s\rangle$.

1.1.3.5 Reduced density operator

Many quantum systems of interest comprise of two or more subsystems, say 1,2,...N. Such systems are described in the composite Hilbert space $H_1 \otimes H_2 \otimes \dots H_N$, where H_i is a subsystem Hilbert space of dimension d_i . In such cases, it might sometimes be more interesting to study the properties of a subsystem than the whole. A subsystem ρ_A can be obtained from the parent composite system ρ_{AB} by the *partial trace* operation which is defined as

$$\rho_A = \text{tr}_B (\rho_{AB}), \quad (1.17)$$

if the composite density operator ρ_{AB} can be expressed in the eigenbases of subsystems A and B as $\rho_{AB} = \sum_{i,j,k,l} c_{ijkl} |a_i\rangle\langle a_j| \otimes |b_k\rangle\langle b_l|$. By performing the trace over subsystem B, we get

$$\rho_A = \sum_{i,j,k,l} c_{ijkl} |a_i\rangle\langle a_j| \text{tr}(|b_k\rangle\langle b_l|) = \sum_{i,j,k,l} c_{ijkl} |a_i\rangle\langle a_j| \langle b_k|b_l\rangle = \sum_{i,j,k} c_{ijkk} |a_i\rangle\langle a_j|. \quad (1.18)$$

Similarly we can obtain reduced density matrix $\rho_B = \text{tr}_A (\rho_{AB}) = \sum_{i,k,l} c_{iikl} |b_k\rangle\langle b_l|$. The above definition of reduced density matrices can be verified to hold true since it correctly explains the outcomes of measurement observables on a subsystem of the composite system [28]. The reduced states of a pure state composite system can reveal information about quantum correlations - like entanglement present in the system. A separable pure state will give rise to a reduced state that is also pure, thereby satisfying the condition $\text{tr}(\rho_A^2) = 1 = \text{tr}(\rho_B^2)$. An entangled state on the other hand is not separable, and results in a mixed reduced state with $\text{tr}(\rho_{A/B}^2) < 1$.

1.1.4 Measurement

We must conduct measurements on a quantum system in order to obtain information on observables like position, spin, momentum, etc. However, the measurement process itself, such as

flashing photons, alters the system and leads to its collapse (probabilistically) to an observable eigenstate. Furthermore, even if the development of the combined system and measuring device may be unitary, such protocols need connecting the system with a suitable measuring device, which results in non-unitary (system) dynamics. Measurement phenomena on quantum systems are described by a collection of positive semi-definite operators $\{M_m\}$ [28] which act on a state $|\psi\rangle$ to give an outcome m described by the post-measurement state

$$|m\rangle = \frac{M_m|\psi\rangle}{\sqrt{p_m}}, \text{ with the probability } p_m = \langle\psi|M_m^\dagger M_m|\psi\rangle. \quad (1.19)$$

Since the sum of probabilities of all possible outcomes must add to one, i.e., $\sum_m p_m = 1$, so the completeness constraint is automatically applied to the measurement operators such that $\sum_m M_m^\dagger M_m = \mathbb{1}$.

1.1.4.1 Projective measurements

Projective measurements are special cases of general measurements M when the measurement operators are Hermitian and orthogonal projectors. The spectral decomposition of this Hermitian operator gives the eigenstates $\{|m\rangle\}$ with eigenvalues $\{\lambda_m\}$, and the projective measurement operator is defined as the *projector* (P_m) of these eigenstates [28]. Hence,

$$M = \sum_m \lambda_m |m\rangle\langle m| = \sum_m \lambda_m P_m. \quad (1.20)$$

Since the eigenbasis is orthonormal and complete, the projectors are orthogonal to one another, i.e., $P_m P_n = \delta_{mn} P_m$, and $\sum_m P_m = \mathbb{1}$. The action of the projector corresponding to an outcome $|m\rangle$ on a general state $|\psi\rangle$ is given by

$$|\psi_m\rangle = \frac{P_m|\psi\rangle}{\sqrt{p_m}}, \text{ with probability } p_m = \langle\psi|P_m|\psi\rangle. \quad (1.21)$$

1.1.4.2 POVM

Positive Operator-Valued Measure (POVM) is a more versatile measurement system that relaxes the need for measurement operators to be orthogonal to one another [28]. A measure whose val-

ues are positive semi-definite operators on a Hilbert space is known as a positive operator-valued measure (POVM) in functional analysis and quantum information science. Quantum measurements defined by POVMs are a generalisation of quantum measurements described by PVMs (also known as projective measurements), and POVMs are a generalisation of projection-valued measures (PVM). To put it roughly, a POVM is comparable to a PVM in the same way as a mixed state is to a pure one. POVMs are required to explain how a projective measurement on a larger system affects a subsystem, much as mixed states are required to specify the state of a subsystem of a larger system. They are described using measurement operators as $F_m = M_m^\dagger M_m$, which follow the criteria (a) operators F_m are positive, and (b) satisfy completeness condition via $\sum_m F_m = \mathbb{1}$. Hence, given a POVM operator F_m , the corresponding probability of outcome m for a system in state $|\psi\rangle$ is $p(m) = \langle\psi|F_m|\psi\rangle$.

1.2 Quantum correlations

One crucial and distinctive aspect of quantum mechanics is quantum correlations. To put it simply, there are subsystem links that prevent measurement findings from each subsystem from being described as distinct, non-overlapping values [29]. Numerous quantum computing and information processing tasks have demonstrated the importance of such quantum correlations, particularly entanglement [30, 31]. Of the many quantum correlations, we will briefly describe some types of quantum correlations and their quantifiers that are used in this work.

1.2.1 Quantum discord

Quantum discord is a different non-classical connection that has been extensively researched [32–36]. This correlation is characterised in terms of the mutual information in a bipartite system and was first proposed by Zurek et. al. [37] in 2001. The correlation measure of discord filters out all classical correlations present in the system, and quantifies only quantum correlations.

Let's start with the famous Shannon entropy, $H(X)$, which is a measure of a system's classical information content and is given by

$$H(X) = - \sum_i p_i \log_2(p_i) \quad (1.22)$$

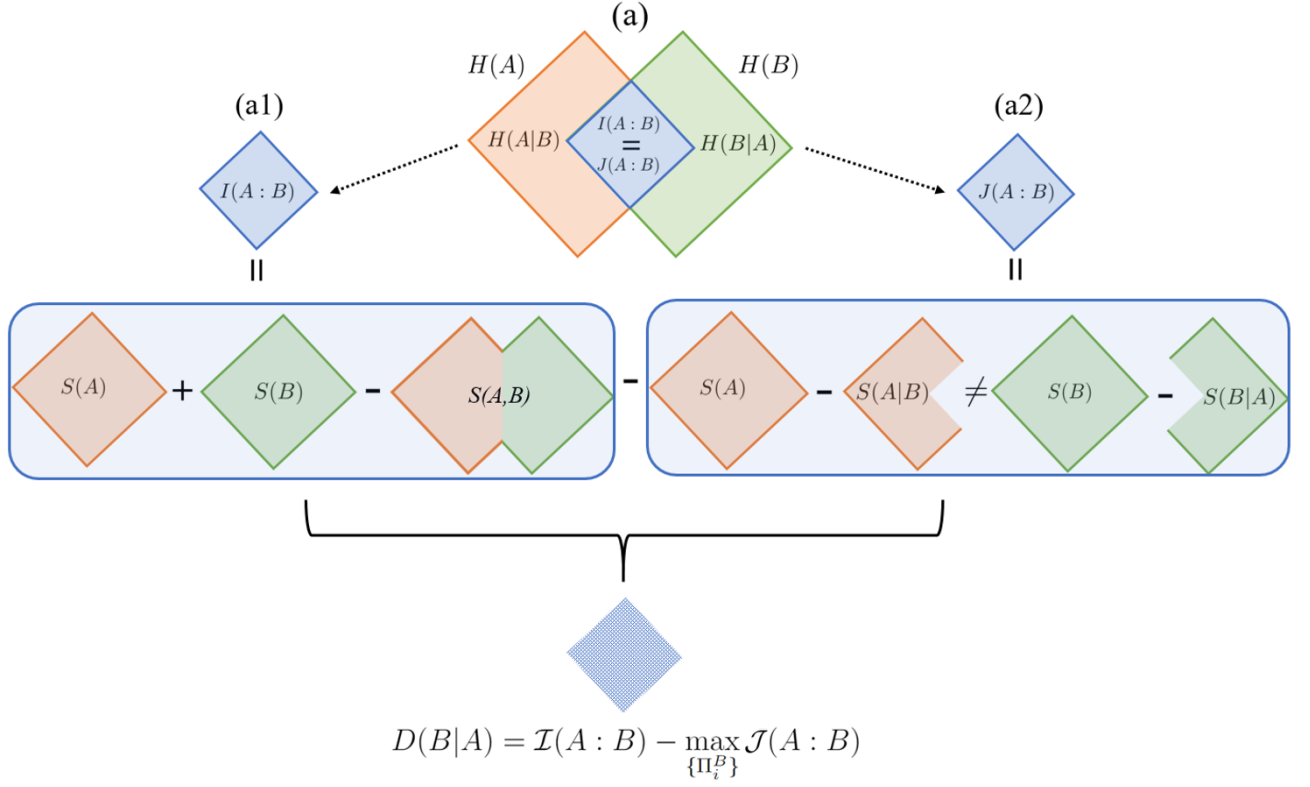


Figure 1.3: For the (a) classical situation, mutual information is computed in two distinct ways: conditional measurements yield $J(A : B) = H(A) - H(A|B)$, and Shannon entropies of subsystems yield $I(A : B) = H(A) + H(B) - H(A, B)$. It is $I(A : B) = J(A : B)$ in this instance. In terms of von Neumann entropy, the quantum mechanical definition states that (a1) $\mathcal{I}(A : B) = S(A) + S(B) - S(A, B)$ contains both classical and quantum correlations, and (a2) conditional measurement yields $\mathcal{J}(A : B) = S(A) - S(A|B)$, which, when maximized over all measurement bases \prod_i^B of subsystem B , gives the total classical correlations in the system. Quantum discord results from the difference between the two definitions of quantum mechanics.

where $\{p_i\}$ is the probability distribution of the possible outcomes of X . The common information that two subsystems A and B share is then referred to as mutual information. It is shown by the blue-colored area of intersection in Fig. 1.3(a). It is measured mathematically as

$$I(A : B) = H(A) + H(B) - H(A, B).$$

Alternatively, one can use conditional entropy $H(A|B) = H(A, B) - H(B) = H(A) - I(A : B)$, which quantifies the information content unique to A and not shared with B . Hence, mutual

information can also be given by

$$J(A : B) = H(A) - H(A|B).$$

Note that this definition requires measurement of the subsystem B [38] since

$$H(A|B) = \sum_j p(b_j) H(A|B = b_j), \text{ with}$$

$$H(A|B = b_j) = - \sum_i p(A = a_i|B = b_j) \log_2 p(A = a_i|B = b_j).$$

Definitions $I(A : B)$ and $J(A : B)$ are classically equivalent, and give identical values of mutual information, as shown in Fig. 1.3(a). However, this is not the case for quantum systems.

In the quantum scenario, information content in a density matrix ρ is quantified by the von Neumann entropy $S(\rho) = -\text{Tr}(\rho \log_2 \rho)$. For a bipartite quantum system AB , the mutual information between A and B can be defined analogous to $I(A : B)$ as

$$\mathcal{I}(A : B) = S(A) + S(B) - S(AB), \quad (1.23)$$

where $S(A)$, $S(B)$ and $S(AB)$ are von Neumann entropies of subsystems A , B , and the composite system AB respectively. This definition is depicted in the top panel in Fig. 1.3(a1). The alternative definition of mutual information is given by

$$\mathcal{J}(A : B) = S(A) - S(A|B), \quad (1.24)$$

where the conditional entropy $S(A|B) = \sum_j p_j^B S(A|B = b_j)$ is the entropy of subsystem A conditional to a measurement on subsystem B giving a result b_i from the possible outcomes of B , with probability p_j^B [37]. This is displayed in Fig. 1.3(a2).

The estimates of $\mathcal{J}(A : B)$ can vary depending on the choice of measurement bases, while $\mathcal{I}(A : B)$ is independent of measurement basis. Consequently, The (minimum) difference between the two ways of evaluating mutual information in Eq. 1.23 and Eq. 1.24 gives the *quantum correlations* present in the system, and is called quantum discord. For orthonormal bases $\{\Pi_i^B\}$

on subsystem B , discord is given by [37]

$$D(B|A) = \mathcal{I}(A : B) - \max_{\{\Pi_i^B\}} \mathcal{J}(A : B), \quad (1.25)$$

1.2.2 Entanglement

In order to understand entanglement, we have to first understand the concept of separability. A pure quantum state is said to be separable if, in the constituent orthonormal bases $\{|a_i\rangle\}$ and $\{|b_j\rangle\}$ of subsystems A and B respectively, $|\psi_{AB}\rangle = \sum_i a_i |a_i\rangle \otimes \sum_j b_j |b_j\rangle$ [39]. In such a case, the reduced states are also pure, and are given simply by $|\psi_A\rangle = \sum_i a_i |a_i\rangle$ and $|\psi_B\rangle = \sum_j b_j |b_j\rangle$. The definition of separability can be extended to mixed states as

$$\rho_{AB} = \sum_i c_i \rho_i^A \otimes \rho_i^B, \quad \text{with } \sum_i c_i = 1, \quad (1.26)$$

which is essentially a convex sum of tensor product states of constituent subsystems. If a bipartite quantum state cannot be expressed as a separable (or product) state, it is said to be entangled [39].

There are multiple quantifiers of entanglement in bipartite systems designed based on whether the composite state of the system is pure or mixed to start with. For a pure state $\rho_{AB} = |\psi_{AB}\rangle\langle\psi_{AB}|$, if the reduced states ρ_A, ρ_B are mixed, then the composite state is necessarily entangled. Hence, purity of reduced states acts as an quantifier for entanglement in pure composite states, and is also referred to as linear entropy. A related measure of entanglement in pure states is the entanglement entropy (which is used in this thesis and is explained in further detail below). For mixed states, measures of entanglement include concurrence, negativity and logarithmic negativity which is defined based on partial transposition (PPT) criterion [40].

1.2.2.1 Entropy as an entanglement measure

The degree of quantum entanglement between two subsystems that make up a two-part composite quantum system is measured by the entropy of entanglement, also known as entanglement entropy. A reduced density matrix $\rho_A = \text{tr}_B[\rho_{AB}]$ expressing knowledge of the state of a subsys-

tem may be obtained given a pure bipartite quantum state of the composite system ρ_{AB} . For each subsystem, the von Neumann entropy $S(\rho)$ of the reduced density matrix equals the entropy of entanglement. The von Neumann entropy is given by

$$S(\rho) = -\text{tr}(\rho \log_2 \rho) \equiv -\sum_i \lambda_i \log_2 \lambda_i, \quad (1.27)$$

where $\{\lambda_i\}$ are the nonzero eigenvalues of ρ . The von Neumann entropy of a pure state is always zero. As mentioned previously, if the reduced state of a system $\rho_A = \text{tr}_B[\rho_{AB}]$ after partial trace is pure, then the composite state is not entangled. For such a state, $S(\rho_A) = 0 = S(\rho_B)$. However, if the reduced state is mixed, then it implies that the parent composite state is entangled. Unfortunately, entanglement entropy cannot be used as a measure if the composite system is a mixed state.

1.2.2.2 Negativity as an entanglement measure

One of the many easily calculable metric of quantum entanglement in quantum mechanics is negativity. It is an indicator that comes from the PPT separability requirement [40]. It has been demonstrated to be an entanglement monotone [41], making it a suitable entanglement measure even for the mixed states. Negativity is given by

$$N(\rho_{AB}) = \frac{||\rho_{AB}^{TA}|| - 1}{2}, \quad (1.28)$$

where ρ_{AB}^{TA} is the partial transpose of the composite state ρ_{AB} with respect to subsystem A and $||X|| = \text{tr}|X| = \text{tr}\sqrt{X^\dagger X}$ is the trace norm or the sum of the singular values of the operator X . Although this concept does not appear in later chapters, it is widely used as an entanglement measure.

1.3 Ergotropy

Here, we explain “*ergotropy*”[42], a recently presented idea in quantum thermodynamics. According to thermodynamics, the energy and entropy of a system that is initially out of equilibrium and connected to work sources determine the maximum amount of work that the system may pro-

duce. The majority of macroscopic systems exhibit thermodynamic behaviour, evolving close to a Gibbs state while maintaining nearly constant entropy in response to slowly changing external potentials [43]. Conversely, a quantum system experiences a unitary change when exposed to time-dependent external potentials that characterise work sources, and the density matrix cannot become Gibbsian when beginning from an arbitrary initial state since it has constant eigenvalues during such a development. In these situations, the maximum quantity of work that the system may generate is no longer determined by entropy, hence the concept of ergotropy [42] is introduced, which is simply “*the maximum amount of work that can be extracted unitarily from an originally isolated quantum system*”. The basis for ergotropy is given by the property of majorization [44], which asserts that more major states produce more work [43].

Consider a finite system S that can exchange work with external macroscopic sources. This system is thermally isolated but may involve energy exchanges between its parts. The evolution of its density operator $\rho(t)$ is then generated by a Hamiltonian $H(t) = H + V(t)$, where the time dependence of $V(t)$ accounts for work transfer. We call cyclic a process in which S , originally isolated, is coupled at the time $t = 0$ to external sources of work, and decouples from them at the time τ [45]. Thus, the driving variables of the sources are cyclic, and the potential $V(t)$ vanishes before $t = 0$ and after τ : $V(0) = V(\tau) = 0$. However, S need not return to its initial state at the time τ . With the initial state $\rho(0) = \rho_0$ and the system Hamiltonian H being given, we look for the maximum work W_{max} that may be extracted from S for arbitrary $V(t)$. For finite systems, not only is the entropy $S(\rho)$ conserved during the evolution, but so are all the eigenvalues of ρ . In contrast to thermodynamic systems, finite systems keep memory of their initial state and do not involve any relaxation mechanism. One may therefore expect that the maximal amount of work W_{max} extracted from S is generally smaller than the larger systems that evolve in the thermodynamic limit, i.e. $W_{th} = E(\rho_0) - TS(\rho_0) + T \ln Z$ [42], this is the familiar difference of free energy between the initial and final state, both evaluated with the final temperature T , where $Z = \text{tr}(e^{-\beta H})$.

The evolution of ρ is unitary, so that $\rho(\tau) = U\rho_0U^\dagger$. We look for the minimum of the final energy $E_f = \text{tr}(U\rho_0U^\dagger H)$ over all unitary operators U . The variations in U can be parameterized as $\delta U = \delta XU$, where δX is an arbitrary infinitesimal anti-Hermitian operator. Hence, we find $\delta E_f = \text{tr}(\delta XU\rho_0U^\dagger H - U\rho_0U^\dagger \delta XH) = \text{tr}(\delta X[\rho(\tau), H])$. In order to have a stationary E_f ,

$\rho(\tau)$ should commute with H and have the same eigenvalues as ρ_0 . Let the spectral resolutions of ρ_0 and H_0 be

$$\begin{aligned}\rho_0 &= \sum_j \lambda_j |\lambda_j\rangle\langle\lambda_j|, \text{ where } \lambda_{j+1} \geq \lambda_j, \text{ and} \\ H &= \sum_k e_k |e_k\rangle\langle e_k| \text{ where } e_{k+1} \leq e_k.\end{aligned}\tag{1.29}$$

where we descend the eigenvalues for ρ_0 and ascend for H_0 with their corresponding eigenvectors. With such configuration, the minimum of E_f becomes $\sum_j \lambda_j e_j$, which can be easily grasped as: the largest occupation fraction λ_1 finally occupies the lowest level, the second largest the second lowest, and so on. It is reached for

$$\rho(\tau) = \sum_j \lambda_j |e_j\rangle\langle e_j| \tag{1.30}$$

which is stationary since it commutes with H . Finally, we are now in a position to formulate our maximum extractable work as

$$W_{max} = E_0 - E_f = \text{tr}(\rho_0 H) - \text{tr}(\rho(\tau) H). \tag{1.31}$$

1.3.1 Passive states

Before ergotropy was introduced, the idea of passive states was widely accepted as gibbs states at all temperatures are passive [43, 46], but it gained prominence after that. If the equilibrium states of a general quantum system are characterized by the condition saying that the systems are unable to perform mechanical work in cyclic (unitary) processes. This condition is called “*passivity*,” which is suggested by the second principle of thermodynamics. In simpler words, a passive state ρ^p of a general quantum system initialized as ρ_0 is defined as “a state from which no further work can be extracted by any unitary means”. Thus, ergotropy for the passive state will be zero $W_{max} = 0$, which directly implies $\rho^p = \rho(\tau)$ Eq. 1.30. For instance, let us consider a

three-level system initialized as

$$\rho_0 = \lambda_1 |\lambda_1\rangle\langle\lambda_1| + \lambda_2 |\lambda_2\rangle\langle\lambda_2| + \lambda_3 |\lambda_3\rangle\langle\lambda_3| \quad \text{with, } \lambda_1 \geq \lambda_2 \geq \lambda_3$$

$$H = e_1 |e_1\rangle\langle e_1| + e_2 |e_2\rangle\langle e_2| + e_3 |e_3\rangle\langle e_3| \quad \text{with, } e_1 \leq e_2 \leq e_3.$$

Let $|\lambda_1\rangle = \frac{|e_1\rangle + |e_3\rangle}{\sqrt{2}}$, $|\lambda_2\rangle = |e_2\rangle$ and $|\lambda_3\rangle = \frac{|e_1\rangle - |e_3\rangle}{\sqrt{2}}$, following these values if we write ρ_0 and H in energy eigenbasis, we have

$$\rho_0 = \begin{bmatrix} (\lambda_1 + \lambda_3)/2 & 0 & (\lambda_1 - \lambda_3)/2 \\ 0 & \lambda_2 & 0 \\ (\lambda_1 - \lambda_3)/2 & 0 & (\lambda_1 + \lambda_3)/2 \end{bmatrix}, H = \begin{bmatrix} e_1 & 0 & 0 \\ 0 & e_2 & 0 \\ 0 & 0 & e_3 \end{bmatrix} \quad (1.32)$$

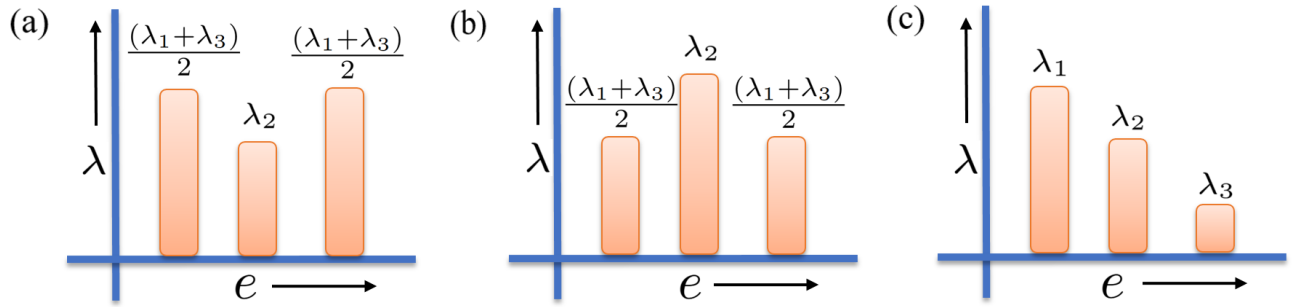


Figure 1.4: (a) and (b) represents the possible population occupation of the initial state ρ_0 with increasing energy. (c) shows the passive state ρ^p population occupation.

For all possible values of λ_1 , λ_2 and λ_3 the initial state ρ_0 does not appear to be in any form of ascending or descending order in population with increasing energy as shown in Fig. 1.4(a) and (b), which means there exists a unitary transformation that will transform ρ_0 to its passive state ρ^p which is nothing but populations arranged in decreasing order with increasing energy in energy eigenbasis as shown in Fig. 1.4(c).

1.3.2 Ergotropy gap

Up to now, we have only considered a single quantum system for work extraction. Now a genuine question to ask is what happens to ergotropy if there are two or more than two quantum systems.

Let's examine a bipartite system initialized as ρ_{AB} , $\rho_A = \text{tr}_B(\rho_{AB})$ and $\rho_B = \text{tr}_A(\rho_{AB})$ with their corresponding Hamiltonians as H_{AB} , H_A and H_B . Now ergotropy can be obtained in one of two ways: either locally, where only subsystems are allowed for work extraction using local unitaries $U_A \otimes U_B$, or globally, where the complete system is available for work extraction using a global unitary U_{AB} . Let's define a quantity called *Ergotropy gap* as the difference between global ergotropy and local ergotropies given by

$$\Delta = W_{max}^{AB} - (W_{max}^A + W_{max}^B) \quad (1.33)$$

Now $\Delta \geq 0$ always, as global operations are capable of extracting more work than local ones, since state can be locally passive but globally not. Such an enhancing may have two origins: (i) if our system is in active state, which is $\rho_A^p \otimes \rho_B^p \neq \rho_{AB}^p$ [47] or (ii) if our system is in a completely passive state [43, 46, 48] but there exist correlations among the subsystems [47, 49].

1.4 NMR experimental setup

In this thesis, we have employed the NMR setup to investigate quantum batteries and many-body entanglement as an application of ergotropy. Since the 1940s, when Rabi oscillations were discovered, NMR has experienced significant theoretical and experimental advancement. [50]. It has paved the way for a plethora of new studies in physics, chemistry, biology, and medicine, including investigations into the magnetic characteristics of materials, the structures of molecules and proteins, MRI tissue imaging, and more [51–53], a commonly used NMR spectrometer is shown in Fig. 1.5. NMR is also an excellent platform for implementation of quantum information processing tasks [54–56]. In this section, we provide a brief summary of the experimental setup and its potential applications in the investigation of quantum information and computing processes.

1.4.1 Nuclear spin as a qubit

Utilising nuclei's intrinsic spin degree of freedom is a feature of NMR. A spin angular momentum $\hat{\mathbf{I}}$, whose eigenvalue is provided by $\sqrt{I(I+1)}\hbar$ [52], is linked with each spin $\hat{\mathbf{I}}$, which might have



Figure 1.5: NMR spectrometer.

spin $I = 1/2, 1, 3/2, \dots$, depending on the nucleon configuration in the system.

A non-zero spin has a magnetic moment given by $\hat{\mu} = \gamma \hbar \hat{\mathbf{I}}$ where γ is the gyromagnetic ratio. A spin- I system when placed in an external magnetic field $\hat{\mathbf{B}} = B_0 \hat{z}$ interacts with it via Zeeman Hamiltonian which is given by

$$H_0 = -\hat{\mu} \cdot \hat{\mathbf{B}} = -\gamma \hbar B_0 I_z = \hbar \omega_0 I_z, \quad (1.34)$$

where $I_z = \sigma_z/2$ is the z -component of the spin angular momentum, and $\omega_0 = -\gamma B_0$ is the Larmor frequency. Since a non-zero spin is like a tiny magnet, when placed in an external field, it acts as a gyroscope and precesses about the field at $\omega_0/2\pi$ frequency. For fields of a few Tesla (typical of commercial NMR spectrometers), the Larmor frequency is of the order of hundreds of MHz. For a spin- I system, energy eigenvalues of the Hamiltonian are $E = -m_s \hbar \gamma B_0$, where $m_s = \{-I/2, -I/2 + 1, \dots, I/2\}$ are the magnetic quantum numbers, which forms a $2I + 1$ level system with equal energy gaps $\Delta E = \hbar \gamma B_0 = \hbar \omega_0$.

In NMR we have approximately about 10^{18} molecules per sample constituting an ensemble of nuclear spins. Now let's consider an ensemble of spin-1/2 systems having two energy levels corresponding to $m_s = \pm 1/2$. In the absence of an external field, the spin levels $|m_s = -1/2\rangle$ and $|m_s = 1/2\rangle$ are degenerate, and each spin is oriented randomly. Hence, the net magnetic moment is zero. When an external field $\hat{\mathbf{B}} = B_0 \hat{z}$ is introduced, the degeneracy between different

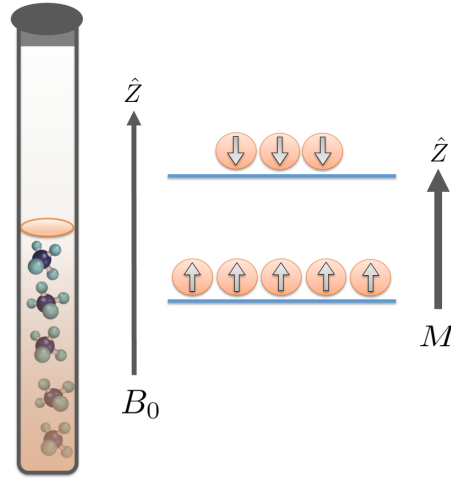


Figure 1.6: An NMR sample's schematic in an external magnetic field. The molecules in a typical sample are about 10^{18} , and at a temperature T , they settle to the Boltzmann distribution at thermal equilibrium. In the ground state, a net magnetization M parallel to the external field is created by the fractional surplus population.

spin levels is lifted, and they try to align along the z -direction. At ambient temperatures, the thermal energy of the system is much larger than the Zeeman energy splitting. Hence even the higher energy level is populated, and the system at thermal equilibrium at a temperature T is in a highly mixed state. The corresponding density matrix is diagonal, with populations in different energy levels distributed according to the Boltzmann function [52]. The diagonal elements of the density matrix are given by

$$\rho_{\text{eq}}^i = \frac{e^{-E_i/k_B T}}{\sum_i e^{-E_i/k_B T}}, \quad (1.35)$$

where E_i is the energy of the i -th spin level and k_B is the Boltzmann constant. For high temperature approximation, i.e. $\hbar\omega_0 \ll k_B T$, it can be easily shown that at thermal equilibrium,

$$\rho^{eq} = \begin{bmatrix} \frac{1+\epsilon}{2} & 0 \\ 0 & \frac{1-\epsilon}{2} \end{bmatrix} = \frac{1}{2}\mathbf{I} + \epsilon I_z \quad (1.36)$$

where $\epsilon = \hbar\gamma B_0/(2k_B T)$ is called the *purity factor* whose magnitude is of the order of 10^{-5} . The ground state ($|m_s = 1/2\rangle$) has a slightly higher population than the higher energy level ($|m_s = -1/2\rangle$), and hence there is a net magnetic moment or magnetization parallel to the external applied field, as shown in Fig. 1.6. If we assign $|m_s = 1/2\rangle \equiv |0\rangle$ and $|m_s = -1/2\rangle \equiv |1\rangle$, we will have our qubit, which establishes a link between NMR and quantum information process-

ing.

1.4.1.1 Qubit interactions

Most of the quantum information processing tasks require at least two interacting qubits. In NMR, interactions naturally present in the system help in this regard. These interactions are of two types [52] -

- (i) spin-spin scalar coupling or J -coupling which is indirectly mediated by electron
- (ii) dipolar interactions mediated direct spin-spin coupling through space

which are explained below. Spin with $I \geq 1$, called quadrupolar spins or qudit, have asymmetric electric charge distribution in the nuclei which gives rise to quadrupolar couplings [52].

For the case dealt in this thesis, namely, isotropic liquid, the direct dipole-dipole interactions average out to zero due to the fast tumbling motion of the spins [52]. However, indirect coupling also known as J - coupling survives and corresponds to the rotating-frame Hamiltonian given by (assuming $\hbar = 1$)

$$H_{int} = \sum_i \omega_i I_{zi} + \sum_{i,j>i} 2\pi J_{ij} I_i \cdot I_j. \quad (1.37)$$

with indirect spin-spin J -coupling J_{ij} . Here $I_i \cdot I_j = I_{xi}I_{xj} + I_{yi}I_{yj} + I_{zi}I_{zj}$. In the weak coupling limit at high fields, i.e., $|J_{ij}| \ll |\omega_i - \omega_j|$, under secular approximation [52], Eq. 1.37 becomes

$$H_{int} = \sum_i \omega_i I_{zi} + \sum_{i,j>i} 2\pi J_{ij} I_{zi} I_{zj}. \quad (1.38)$$

Note that, in case of heteronuclear spins this approximation is always satisfied since the Larmor frequency difference typically falls in MHz range and J -coupling constants are in Hz. For a two qubit system the above Hamiltonian has four eigenstates which form the basis $\{|00\rangle, |01\rangle, |10\rangle, |11\rangle\}$.

The eigenvalues corresponding to basis states are:

$$\begin{aligned} |00\rangle &\rightarrow (\omega_1 + \omega_2 + \pi J)/2 \\ |01\rangle &\rightarrow (\omega_1 - \omega_2 - \pi J)/2 \\ |10\rangle &\rightarrow (-\omega_1 + \omega_2 - \pi J)/2 \\ |11\rangle &\rightarrow (-\omega_1 - \omega_2 + \pi J)/2 \end{aligned} \tag{1.39}$$

1.4.1.2 Relaxation

No system is isolated in reality. System relaxation results from interactions between all systems and their environment. Thermal motion causes changes in the magnetic field surrounding spins, which results in relaxation in NMR [52]. These lead to systemic changes and a loss of coherence. The dipole moments of surrounding spins as the molecules tumble, which result in variations in the local fields around spins, are one of the main reasons of relaxation in liquid state NMR. Two categories can be used to classify the intrinsic relaxation processes:

(i) spin-lattice relaxation (T_1) - also known as longitudinal relaxation, The transverse frequency components around Larmor frequency are responsible for longitudinal relaxation [51, 52]. They introduce random transitions as well as relative phases between energy levels which leads to destruction of coherences and redistribution of populations towards thermal equilibrium on a timescale often termed as T_1 .

(ii) spin-spin relaxation (T_2) - also known as transverse relaxation, this phenomenon is the loss of coherence between spins. This type of relaxation occurs due to longitudinal low-frequency components compared to Larmor frequency. Though these components cannot induce transition, they introduce random relative phases between energy levels. Consequently, this is an energy-conserving process and only leads to decay of coherences while populations remain unaltered on a timescale often termed as T_2 , usually the transverse relaxation has a shorter life span than longitudinal relaxation, i.e. $T_2 < T_1$.

1.4.1.3 Chemical shift

In reality, most nuclear spin systems used in experiments are not unbound elements but rather molecules submerged in a solvent. In this case, the chemical environment surrounding the nucleus in the molecule causes the local field of a nucleus to be different from that of a free spin. The effective field surrounding the nucleus is altered by the dispersion of electronic clouds from the surrounding components, changing the Zeeman Hamiltonian.[51, 52]

$$\begin{aligned} H &= H_0 + H_{cs} \\ H_{cs} &= \hbar\gamma\delta_j \cdot \hat{\mathbf{B}}, \end{aligned} \tag{1.40}$$

where δ_j is the *chemical shift tensor* at the site of the j -th spin. At a strong external field $\hat{\mathbf{B}} = B_0\hat{z}$, due to rapid tumbling motion of the molecules in liquid samples, this tensor reduces to an averaged isotropic scalar value $\bar{\delta}$. Hence with $H_{cs} = \hbar\gamma\bar{\delta}B_0I_z$, the above equation becomes $H = -\hbar\gamma(1 - \bar{\delta})B_0I_z$, where we can identify the shifted Larmor frequency $\omega = -\gamma(1 - \bar{\delta})B_0$. The chemical shift is characteristic of the molecule and helps with addressability of qubits.

1.4.1.4 PFG (Pulsed Field Gradient)

Pulsed field gradients (PFGs) are magnetic fields that change spatially and are used to create space-dependent phases in the sample as needed. The NMR sample tube is aligned parallel to the static magnetic field $\hat{B} = B_0\hat{z}$, and the gradient is applied along the \hat{z} direction. This is given by:

$$\hat{B}(z) = zG_z\hat{z} \tag{1.41}$$

where G_z is the strength of the gradient. When such a gradient is applied, spins at various locations along the sample's length \hat{z} encounter various local magnetic fields. The transverse components of the magnetization vector precess at various Larmor frequencies along the sample's length because the spins' Larmor frequency is exactly proportional to the magnetic field. Thus, any phase coherence between the transverse components of the magnetization throughout the sample length is broken during the gradient's application, so removing the net transverse magne-

tization over the bulk sample volume. From an information processing point of view, PFGs are routinely used to destroy coherences, and for coherence order selection and filtering [57–59].

1.5 NMR based quantum information processing

Here, we describe how properties of NMR systems can be used to study quantum information processing tasks.

1.5.1 Qubit manipulation

The energy gaps between NMR qubit levels, as described in Sec. 1.4.1, are in the range of hundreds of MHz, which fall under the radio frequency (RF) range. Hence, NMR qubits can be manipulated by RF fields. A linearly polarized RF field $2B_1 \cos(\omega_{rf}t + \phi)$ applied transversely to the external field can be described by the following time-dependent Hamiltonian [51, 52]

$$H_{\text{RF}}(t) = -\gamma I_x \{2B_1 \cos(\omega_{rf}t + \phi)\} = 2\omega_1 I_x \cos(\omega_{rf}t + \phi), \quad (1.42)$$

where $\omega_1 = -\gamma B_1$ is effective RF amplitude. The resonance condition is achieved when $\omega_{rf} = \omega_0$. Otherwise, the difference between the two is called offset. The linear polarized RF field can be decomposed into right (B_r) and left (B_l) circularly polarized components

$$\begin{aligned} B_r(t) &= B_1 [\cos(\omega_{rf}t + \phi)\hat{x} + \sin(\omega_{rf}t + \phi)\hat{y}], \\ B_l(t) &= B_1 [\cos(\omega_{rf}t + \phi)\hat{x} - \sin(\omega_{rf}t + \phi)\hat{y}]. \end{aligned}$$

respectively, representing fields rotating in the same and opposite directions with respect to the precession of the nuclei. In the frame rotating with nuclear Larmor frequency, the field $B_r(t)$ is stationary, corresponds to the resonant component, while $B_l(t)$ rotates with twice the Larmor frequency ω_0 . Hence, in high-field rotating wave approximation, only $B_r(t)$ has effect on the dynamics of nuclei. Now in the rotating frame of ω_{rf} ,

$$B_r^0 = B_1 [\cos(\phi)\hat{x} + \sin(\phi)\hat{y}], \quad (1.43)$$

In an off resonant case with offset $\Omega = \omega_0 - \omega_{rf}$, an effective field can be defined

$$B_{\text{eff}} = \frac{\Omega}{\gamma} \hat{z} + \frac{\omega_1}{\gamma} [\cos(\phi) \hat{x} + \sin(\phi) \hat{y}], \quad (1.44)$$

and accordingly

$$H_{\text{eff}} = \Omega I_z + \omega_1 [\cos(\phi) I_x + \sin(\phi) I_y], \quad (1.45)$$

Therefore, using propagator $U = e^{(-iH_{\text{eff}}\tau)}$, desired evolution of the state of the nuclear spin ensemble can be achieved by careful tuning of RF amplitude and exposure time. Often RF fields are applied in short bursts with high power kHz, called RF pulse or RF rotation. An RF pulse achieving a flip angle $\beta = \omega_1 \tau_p$ can be applied using RF amplitude ω_1 for time τ_p to realize the required qubit evolution. For example, a $\pi/2$ rotation, which equilibrates the populations and creates coherences starting from the thermal equilibrium state, can be achieved using 25 kHz RF amplitude for a 10 μs duration.

1.5.2 NMR Quantum gates

Any quantum computing task can be broken down into single qubit and multi-qubit operations. In this thesis, these are accomplished in NMR by the following -

- (i) Single qubit manipulation \leftrightarrow RF pulses
 - (ii) Multi-qubit operations \leftrightarrow J coupling evolutions and RF pulses
- as explained below.

1.5.2.1 Single qubit gates

The effect of RF pulses, as explained in Sec. 1.5.1, is to bring about rotations of a qubit. This can be used to apply various gates such as NOT, Hadamard, etc.

X or NOT gate

Consider a single qubit system in thermal equilibrium described by the deviation density matrix $\rho = \sigma_z/2$. The net magnetization is parallel to the external field. An RF pulse of amplitude

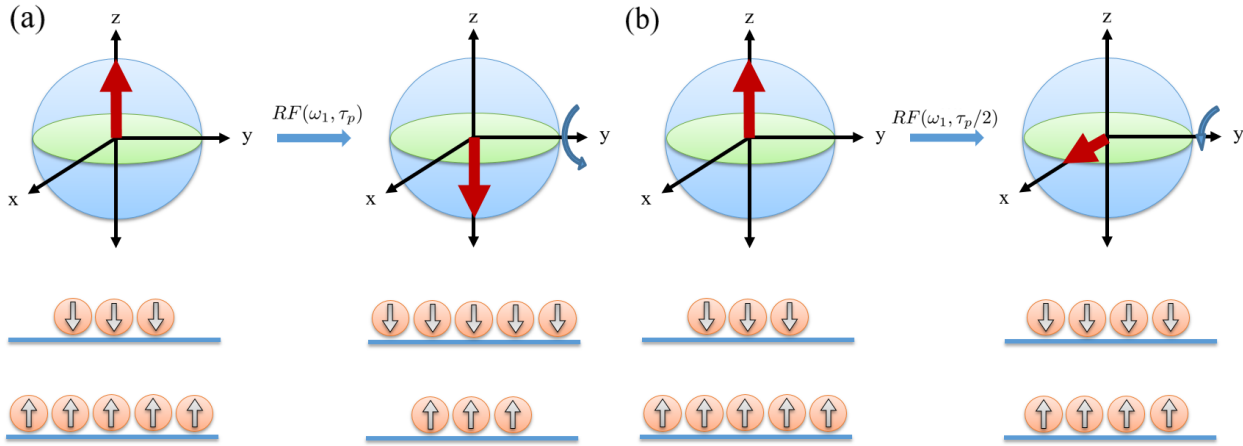


Figure 1.7: (a) For a duration of τ_p , a π pulse with amplitude ω_1 is applied about the x -axis, rotating the net magnetization 180° from z to $-z$. A NOT gate (b) $\pi/2$ pulse of amplitude ω_1 applied for length $\tau_p/2$ around the y -axis rotates the net magnetization by 90° from z to x , which equalizes population in the energy levels and causes a population inversion. This is how a *pseudo* Hadamard gate is implemented.

corresponding to $\omega_1 = -\gamma B_1$ for duration τ_p such that the flip angle $\beta = \omega_1 \tau_p = \pi$ and phase $\phi = 0$ which translates to the x -axis is given by the operator $R_x(\pi) = \exp(-i\pi I_x)$ where $I_x = \sigma_x/2$. This pulse acts on each spin to induce a rotation by angle π about the x -axis such that the net magnetization is rotated by 180° from $+z$ to $-z$ as shown in Fig. 1.7(a). In quantum computation terms, this transforms the state $|0\rangle \xrightarrow{R_x(\pi)} |1\rangle$. The matrix form of the NOT gate is

$$R_x(\pi) = \exp(-i\pi I_x) = -i \begin{bmatrix} 0 & 1 \\ 1 & 0 \end{bmatrix}.$$

The pre-factor i is a global phase and hence can be ignored.

Hadamard gate

The Hadamard gate $H = \frac{1}{\sqrt{2}} \begin{bmatrix} 1 & 1 \\ 1 & -1 \end{bmatrix}$ can be experimentally realized by a sequence of two pulses (i) $\pi/2$ rotation about y -axis ($R_y(\pi/2)$), followed by (ii) π rotation about x -axis ($R_x(\pi)$) whose matrix form is

$$R_x(\pi)R_y(\pi/2) = \exp(-i\pi I_x) \exp(-i\pi/2 I_y) = -i \begin{bmatrix} 0 & 1 \\ 1 & 0 \end{bmatrix} \frac{1}{\sqrt{2}} \begin{bmatrix} 1 & -1 \\ 1 & 1 \end{bmatrix} = \frac{-i}{\sqrt{2}} \begin{bmatrix} 1 & 1 \\ 1 & -1 \end{bmatrix}.$$

Again, the global phase $-i$ can be ignored. Often a pseudo Hadamard gate is used instead of Hadamard gate which is just a $R_y(\pi/2)$ pulse, as illustrated in Fig. 1.7(b).

1.5.2.2 Multi-qubit gates

Multi-qubit gates can be realized using a combination of RF pulses and evolution under the indirect coupling Hamiltonian given in Eq. 1.38. An NMR pulse sequence to realize a CNOT gate with the first qubit as control and second qubit as the target can be following (time ordered from right to left)

$$U_{CNOT} = R_y^2(\pi/2)U(\tau)R_{-y}^2(\pi/2)R_{-x}^2(\pi/2)R_{-z}^1(\pi/2), \quad (1.46)$$

where $U(\tau) = \exp(-iH\tau)$ with $\tau = 1/(2J_{12})$ is the evolution under the coupling Hamiltonian $H = 2\pi J_{12}I_{z1}I_{z2}$.

1.5.3 PPS (Pseudo-Pure States)

Initialising the system into a desired state, usually a pure state, is one of the fundamental prerequisites for many quantum information processing tasks [60]. NMR spins require highly strong magnetic fields or extremely low temperatures to create pure states because of their incredibly low purity factors. Instead, one can prepare *pseudo-pure states* (PPS) which are of the form

$$\rho_{\text{pps}} = \left(\frac{1-\epsilon}{4}\right) \mathbb{1} + \epsilon|00\rangle\langle 00|. \quad (1.47)$$

PPS has a little surplus population in the desired state ($|00\rangle$ in the example above) and a uniform background population in all states (caught by the identity term) as shown in Fig. 1.8. The dynamics of a PPS is isomorphic to that of the corresponding pure state [6]. This can be intuitively understood from the form of Eq. 1.47 where identity term remains invariant under evolution and any interesting dynamics is the result of evolution of the other term with ϵ purity. Moreover, the identity term does not contribute to the measured NMR signal.

A single qubit system is always in a pseudo-pure state. For two and more qubits, there are various techniques to prepare PPS including spatial averaging [6], temporal averaging [61], and

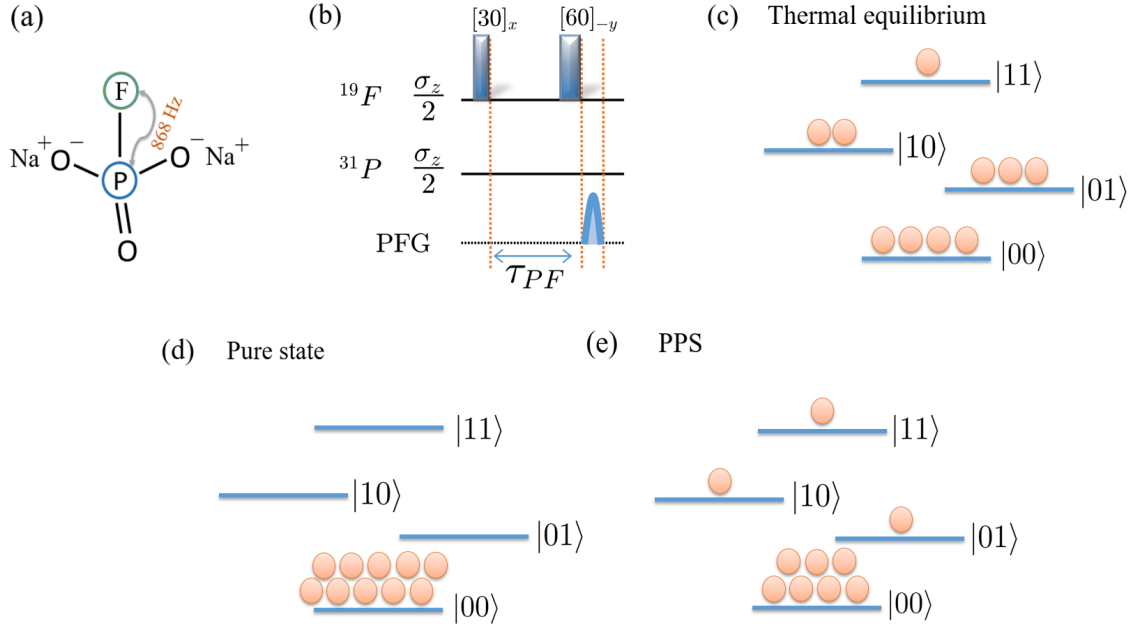


Figure 1.8: (a) Sodium fluorophosphate (NAFP) where spins ^{19}F and ^{31}P constitute a two qubit system (b) NMR pulse sequences for preparing PPS ($|00\rangle\langle 00|$) of NAFP molecule with $\tau_{PF} = 1/(2J_{PF})$ and (c) Population distribution of a two qubit thermal equilibrium state (d) two qubit pure state (e) two qubit PPS.

logical labelling [7]. We use the spatial averaging technique in this thesis, which uses single and multi-qubit gate to transfer populations between different spin states. These naturally generate coherences, which are destroyed using gradients (PFG). For the two-qubit system formed by ^{19}F and ^{31}P nuclei of sodium fluorophosphate molecule if we start with the thermal state as $\rho_{th} = \mathbf{I}/4 + \epsilon_P(\frac{\gamma_F}{\gamma_P}I_{1z} + I_{2z})$, where $\epsilon_P = \gamma_P B_0/4k_B T$ and $\frac{\gamma_F}{\gamma_P} \approx 4/\sqrt{3}$. The identity part is invariant under the unitary transformations, neither contributes to the NMR signal, and is ignored henceforth. The preparation of PPS obtained by pulse sequence shown in Fig. 1.8(b) can be understood by using product operator formalism [51] as follows:

$$\begin{aligned}
 \frac{1}{4}\mathbf{I} + \epsilon_P \left[\frac{4}{\sqrt{3}}I_{1z} + I_{2z} \right] &\xrightarrow{30^F_x} \frac{1}{4}\mathbf{I} + \epsilon_P \left[\frac{4}{\sqrt{3}}\frac{\sqrt{3}}{2}I_{1z} - \frac{4}{\sqrt{3}}\frac{1}{2}I_{1y} + I_{2z} \right] \\
 &\xrightarrow{1/2J_{PF}} \frac{1}{4}\mathbf{I} + \epsilon_P \left[2I_{1z} + \frac{4}{\sqrt{3}}I_{1x}I_{2z} + I_{2z} \right] \\
 &\xrightarrow{60^F_{-y}, \text{ PFG}} \frac{1}{4}\mathbf{I} + \epsilon_P [I_{1z} + 2I_{1z}I_{2z} + I_{2z}] \\
 &\equiv |00\rangle\langle 00|.
 \end{aligned} \tag{1.48}$$

1.5.4 Measurement in NMR

In NMR, as explained in Sec. 1.4.1, the sample has a net magnetization, which at thermal equilibrium is aligned parallel to the external field. When an RF pulse is applied to tilt it away from this direction, it begins to precess about the z -axis. In NMR architecture, RF receiver coils are in the transverse plane. Hence, as the magnetization precesses, it cuts through these coils generating a time-varying magnetic flux, which in turn induces an emf in the coils. However, due to inherent relaxation mechanisms, the measured signal decays with time, giving the *free induction decay* (FID) [51, 52]. This FID signal is proportional to

$$F(t) = \text{tr}[\rho(t)(\sigma_x + i\sigma_y)], \quad (1.49)$$

which gives the transverse magnetization components. The frequency spectrum is obtained by taking a Fourier transform of the time-domain FID signal. A schematic of the NMR spectrometer and components are shown in Fig. 1.9.

In general, for a non-equilibrium state, only single quantum coherence elements of the density matrix can be observed using the above FID signal [52]. To measure all the elements of a density matrix, one has to resort to a technique called quantum state tomography [62, 63].

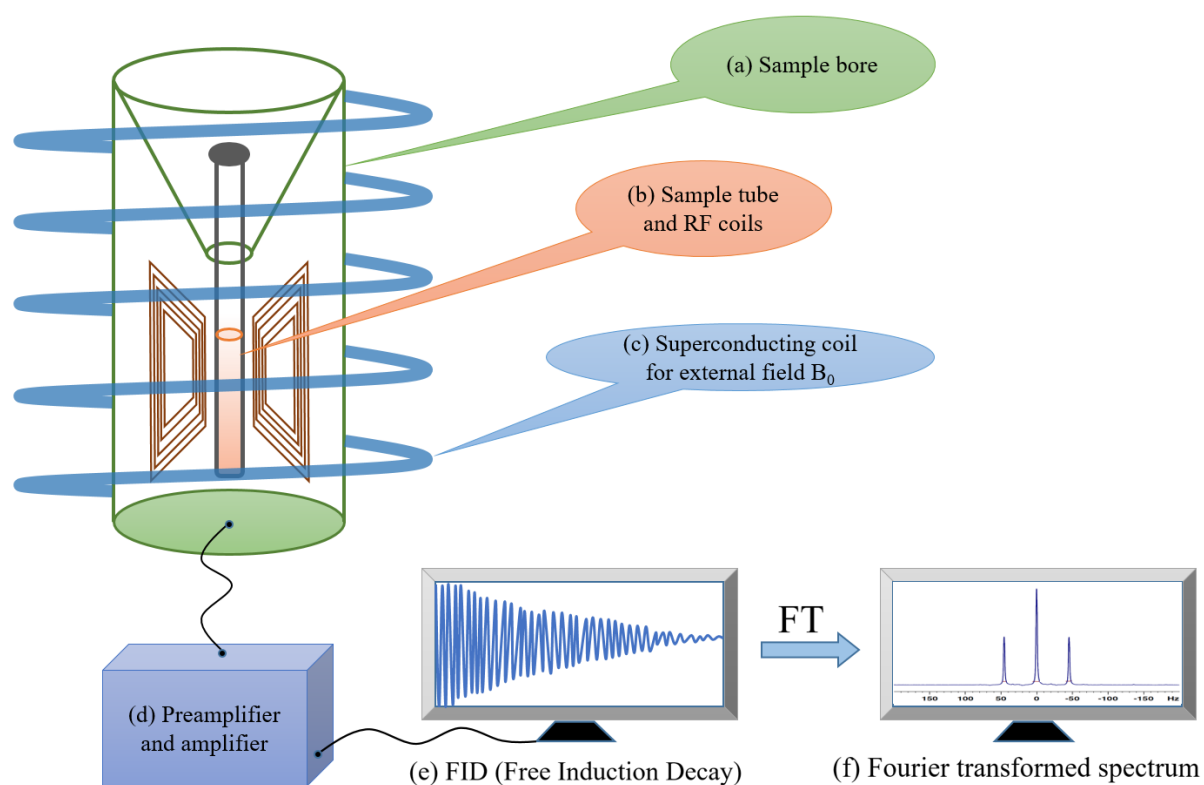
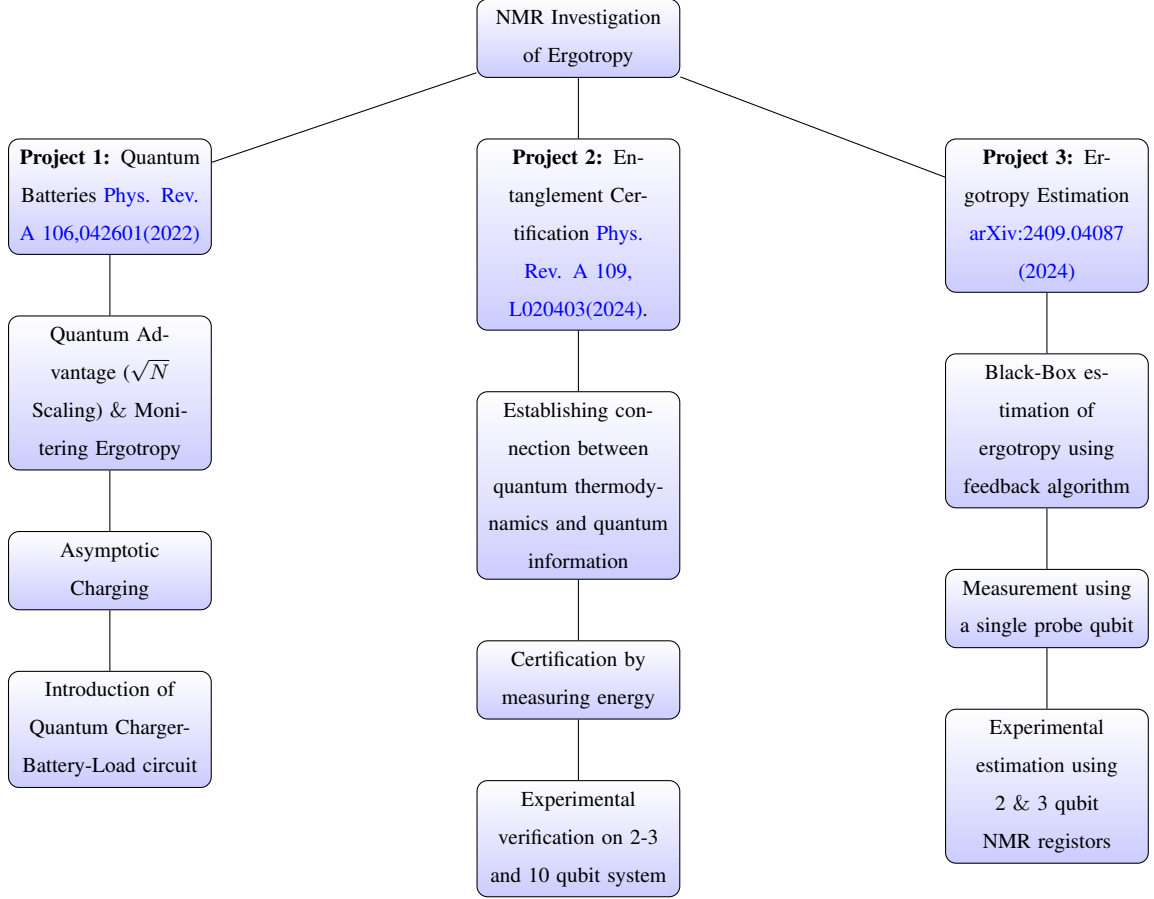


Figure 1.9: An NMR spectrometer schematic. Inserting the sample through bore (a) places it in an area of constant external magnetic field B_0 produced by a superconducting coil (b). Inside, nearer to the sample, are the RF coils (c), with their magnetic field direction perpendicular to B_0 . Preamplifier and amplifier (d) assist in applying pulses and gathering the sample signal. The frequency spectrum (f) is obtained by Fourier transforming the FID signal (e) that was obtained from the sample.

1.6 Thesis Summary



In this thesis, we have experimentally investigated and estimated ergotropy along with its applications in quantum batteries and entanglement certification, as shown in the flow chart. First we estimate the battery energy, ergotropy, and establish the quantum advantage in charging the quantum battery. Next, we have proposed a set of entanglement conditions for multi-qubit systems by measuring certain thermodynamic quantities. Lastly, in order to extract maximal work unitarily from an unknown state, we provide a feedback-based quantum method for ergotropy estimation that directs system dynamics to convert arbitrary initial states into their passive states. The completeness of this study is demonstrated by examining the charging dynamics of quantum batteries and ultimately developing a methodology for discharging.

CHAPTER 2

Nuclear spins as quantum battery

Abstract

Theoretical explorations have revealed that quantum batteries can exploit quantum correlations to achieve faster charging, thus promising exciting applications in future technologies. Using NMR architecture, here we experimentally investigate various aspects of quantum batteries with the help of nuclear spin systems in a star-topology configuration. We first carry out numerical analysis to study how charging a quantum battery depends on the relative purity factors of charger and battery spins. By experimentally characterizing the state of the battery spin undergoing charging, we estimate the battery energy as well as the ergotropy, the maximum amount of work that is unitarily available for extraction. The experimental results thus obtained establish the quantum advantage in charging the quantum battery. We propose using the quantum advantage, gained via quantum correlations among chargers and the battery, as a measure for estimating the size of the correlated cluster. We develop a simple iterative method to realize asymptotic charging that avoids the oscillatory behavior of charging and discharging. Finally, we introduce a load spin and realize a charger-battery-load circuit and experimentally demonstrate battery energy consumption after varying the duration of battery storage, for up to 2 min.

Reported in

Jitendra Joshi and T. S. Mahesh, *Experimental investigation of a quantum battery using star-topology NMR spin systems*, [Phys. Rev. A 106, 042601 \(2022\)](#).

2.1 Introduction

Recent advances in quantum technologies are revolutionizing the world with novel devices such as quantum computers, quantum communication, quantum sensors, and a host of other quantum-enhanced applications [64, 65]. The latest additions include quantum engines [66, 67], quantum diode [68, 69], quantum transistor [70], as well as quantum battery, an energy-storing device [71–73] that is capable of exploiting quantum superpositions [48, 74–78]. While quantum batteries open up novel applications, they are also exciting from the point of view of quantum thermodynamics [79–81], a rapidly emerging field that extends thermodynamical concepts to the quantum regime. It has been theoretically established that quantum batteries can exhibit faster charging in a collective charging scheme that exploits quantum correlations [74, 75, 82]. Recently quantum batteries with various models showing quantum advantages have been introduced [83, 84]. They include quantum cavity [72, 76, 85–91], spin chain [92–98], Sachdev-Ye-Kitaev model [99, 100], and quantum oscillators [71, 77, 101, 102]. There also have been a few experimental investigations of quantum battery, such as the cavity assisted charging of an organic quantum battery [103].

Here we describe an experimental exploration of quantum batteries formed by nuclear spin-systems of different sizes in star-topology configuration. Although, one can consider various other configurations, we find the star-topology systems to be particularly convenient for this purpose for the reasons mentioned in the review [104]. Using NMR methods, we study various aspects of quantum battery by experimentally characterizing its state via quantum state tomography. Thereby we monitor building up of battery energy during collective charging and establish the quantum speedup. We also estimate the quantity *ergotropy*, that quantifies the maximum extractable work. By numerically quantifying quantum correlation in terms of entanglement entropy as well as discord, we reconfirm the involvement of correlations in yielding the quantum speedup. We therefore propose using the quantum speed to estimate size of the correlated cluster. We find this method to be much simpler compared to spatial phase-encoding method [105] or the temporal phase-encoding method (eg. [106]). Unlike classical batteries, charging of a quantum battery is oscillatory, i.e., the quantum battery starts discharging after reaching the maximum charge. Recent theoretical proposals to realize a stable non-oscillatory charging were based on

either adiabatic protocol [107] or shortcut to adiabaticity [108]. Here we propose and demonstrate a simple iterative procedure to realize asymptotic charging based on the differential storage times of the charger and battery spins. Finally, we describe implementing the Quantum Charger-Battery-Load (QCBL) circuit. A similar circuit has recently been theoretically discussed in Ref. [109]. Using a 38-spin star-system we experimentally demonstrate QCBL circuit with battery storage up to two minutes before discharging energy on to the load spin

2.2 Objectives

In this project we study quantum battery in star-topology registers formed by central spin which is symmetrically coupled with non-interacting satellite spins where central spin works as a battery and the satellite spin works as chargers.

- (i) We first establish a quantum advantage of \sqrt{N} on fast charging with N being the number of chargers.
- (ii) We estimate the quantity ergotropy, that quantifies the maximum extractable work.
- (iii) By numerically quantifying quantum correlation in terms of entanglement entropy as well as discord, we reconfirm the involvement of correlations in yielding the quantum speedup.
- (iv) We therefore propose using the quantum speed-up to estimate size of the correlated cluster.
- (v) We propose and demonstrate a simple iterative procedure to realize asymptotic charging based on the differential storage times of the charger and battery spins.
- (vi) Using a 38-spin star-system we experimentally demonstrate QCBL circuit with battery storage up to two minutes before discharging energy on to the load spin.

2.3 Theory

2.3.1 Quantum Battery

The simplest quantum battery (B) consists of a two-level quantum system, like a spin-1/2 particle placed in a magnetic field (Fig. 2.1). Here, the ground state $|0\rangle$ is modeled as a discharged or empty battery, while the excited state $|1\rangle$ is modeled as the fully charged battery. The spin battery

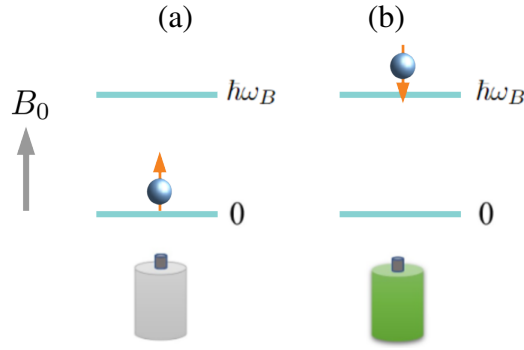


Figure 2.1: A single spin-1/2 particle in an external magnetic field B_0 as a quantum battery. The ground state (a) and excited state (b) correspond respectively to uncharged and charged states of the battery.

can be charged either directly using an external drive [74, 76] or indirectly via an ancillary spin, called charger spin (C) [92, 109]. Let us now consider the B-C spin system. Each of the two spins are governed by their local Hamiltonians H_B and H_C , respectively, which for the sake of simplicity, are chosen to have zero ground-state energy. Moreover, we assume that the quantum system at an initial time $t = 0$ is in a factorized state

$$\rho_{BC}(0) = |0\rangle\langle 0|_B \otimes |1\rangle\langle 1|_C, \quad (2.1)$$

with $|1\rangle\langle 1|_C$ being the excited state of the charger.

We now introduce a coupling Hamiltonian $H_{BC}(t)$ between B and C, in order to transfer as much energy as possible from the charger to the battery over a finite charging duration τ . Under the global Hamiltonian of the system BC

$$H(t) = H_B + H_C + H_{BC}(t), \quad (2.2)$$

the joint system evolves as

$$\begin{aligned} \rho_{BC}(\tau) &= U(\tau)\rho_{BC}(0)U^\dagger(\tau) \\ \text{with } U(\tau) &= T e^{-i \int_0^\tau dt H(t)}, \end{aligned} \quad (2.3)$$

where T is the time-ordering operator. The instantaneous state of battery $\rho_B(\tau) = \text{Tr}_C(\rho_{BC}(\tau))$

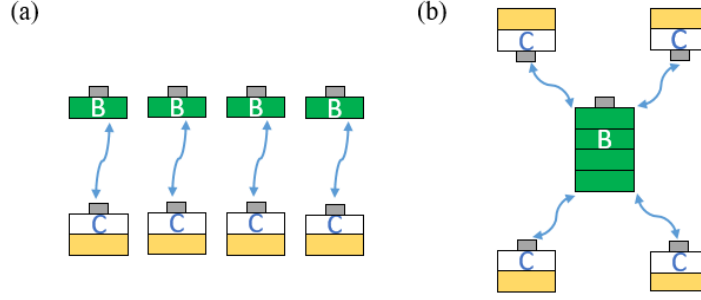


Figure 2.2: Two charging schemes: (a) parallel charging scheme where a single battery is charged by an individual charger and (b) the collective charging scheme where a single battery is charged by multiple chargers.

is obtained by tracing out the charger. The goal is to maximize the local energy of the battery

$$E_B^{\max} = E_B(\bar{\tau}) = \text{Tr}(\rho_B(\bar{\tau})H_B), \quad (2.4)$$

with the shortest possible charging time $\bar{\tau}$. For a given maximum energy charged E_B^{\max} , the charging power is defined as

$$P = E_B^{\max}/\bar{\tau}. \quad (2.5)$$

We now discuss two charging schemes, parallel and collective [74, 76, 92] as illustrated in Fig. 2.2. In parallel charging scheme (Fig. 2.2(a)), each of the N batteries is independently charged to a maximum energy E_B^{\max}/N by one of the N chargers over a duration $\bar{\tau}_1$. Conversely, in the collective charging scheme (Fig. 2.2(b)), all the batteries together form a battery-pack that is charged to a maximum energy E_B^{\max} simultaneously by N chargers over a duration $\bar{\tau}_N$. The latter scheme exploits quantum correlations and hence is more efficient [74, 76]. Let P_1 and P_N be the charging powers of the parallel and collective charging schemes respectively. The quantum advantage of collective charging is defined as [75]

$$\Gamma \equiv \frac{P_N}{P_1} = \frac{E_B^{\max}/\bar{\tau}_N}{N(E_B^{\max}/N)/\bar{\tau}_1} = \frac{\bar{\tau}_1}{\bar{\tau}_N}. \quad (2.6)$$

We may also characterize the state of the battery during charging in terms of ergotropy, or the maximum work that can be extracted [42]. Following Refs. [42, 43, 78], the ergotropy of a

battery at time τ is given by

$$\mathcal{E}(\rho_B(\tau)) = E_B(\rho_B(\tau)) - E_B(\rho_B^p(\tau)), \quad (2.7)$$

where $E_B(\rho) = \text{Tr}(\rho H_B)$ is the energy of the state ρ and $\rho_B^p(\tau)$ is the passive state corresponding to $\rho_B(\tau)$. A passive state, or a zero-ergotropy state, is the one from which no work can be extracted by using unitary methods [42, 43]. To construct the passive state, we first spectrally decompose the state $\rho_B(\tau)$ and Hamiltonian H_B as

$$\begin{aligned} \rho_B(\tau) &= \sum_j r_j |r_j\rangle\langle r_j|, \text{ where } r_1 \geq r_2 \geq \dots, \text{ and} \\ H_B &= \sum_k E_k |E_k\rangle\langle E_k| \text{ where } E_1 \leq E_2 \leq \dots. \end{aligned} \quad (2.8)$$

The passive state is diagonal in the energy basis formed by pairing descending order of populations r_j with ascending order of energy E_j levels, i.e.,

$$\rho_B^p(\tau) = \sum_j r_j |E_j\rangle\langle E_j|. \quad (2.9)$$

Note that the energy of the passive state is

$$E_B(\rho_B^p(\tau)) = \sum_j r_j E_j. \quad (2.10)$$

For a single spin battery described in Fig. 2.1, the eigenvalues of instantaneous state are of the form $(1 \pm \epsilon)/2$ where $|\epsilon| \leq 1$. Therefore,

$$\begin{aligned} \rho_B(\tau) &= \frac{1+\epsilon}{2} |0\rangle\langle 0| + \frac{1-\epsilon}{2} |1\rangle\langle 1| \text{ and} \\ E_B(\rho_B(\tau)) &= \hbar\omega_B \frac{1-\epsilon}{2}. \end{aligned} \quad (2.11)$$

As long as $\epsilon \geq 0$, the ground state is still more populated than the excited state, and the battery remains in the passive state and ergotropy $\mathcal{E}(\rho_B(\tau)) = 0$. After sufficient charging, ϵ becomes

negative, and the passive state changes to

$$\begin{aligned}\rho_B^p(\tau) &= \frac{1-\epsilon}{2}|0\rangle\langle 0| + \frac{1+\epsilon}{2}|1\rangle\langle 1|, \\ E_B(\rho_B^p(\tau)) &= \hbar\omega_B \frac{1+\epsilon}{2}, \\ \text{and ergotropy } \mathcal{E}(\rho_B(\tau)) &= -\epsilon\hbar\omega_B \quad (\epsilon \leq 0).\end{aligned}\tag{2.12}$$

For $|\epsilon| \ll 1$ we find that the dimensionless ratio

$$\frac{\mathcal{E}(\rho_B(\tau))}{-\epsilon E_B(\rho_B(\tau))} = \frac{2}{1-\epsilon} \approx 2.\tag{2.13}$$

In the following we describe the topology of the spin-systems used in our experiments.

2.3.2 star-topology network

We now consider the star-topology network in which a single central battery-spin uniformly interacts with a set of N indistinguishable charger spins [104] as illustrated in Fig. 2.3 (a). Quantum battery in this configuration has been studied theoretically very recently [110]. The spin-systems with $N = 3, 9, 12, 18,$ & 36 studied in this work are shown in Fig. 2.3 (b-f).

We consider the local Hamiltonians for the battery and charger to be

$$H_B = \hbar\omega_B(1/2 - S_z) \text{ and } H_C = \hbar\omega_C I_z.\tag{2.14}$$

Here $S_{x,y,z}$ represent the x, y, z -spin operators for the battery spin with Larmor frequency ω_B , $I_{x,y,z} = \sum_{i=1}^N I_{x,y,z}^i$ represent the collective x, y, z -spin operators for the chargers with Larmor frequency $\omega_C = \gamma\omega_B$, where γ is the relative gyromagnetic ratio. Following Ref. [77], we choose the interaction Hamiltonian,

$$H_{BC}(t) = \hbar 2\pi J (S_x I_x + S_y I_y),\tag{2.15}$$

where $J \ll |\omega_{C(B)}|$ is the coupling constant between the battery and the charger spins.

The spin-system is prepared in the thermal equilibrium state, which is in a generalized form

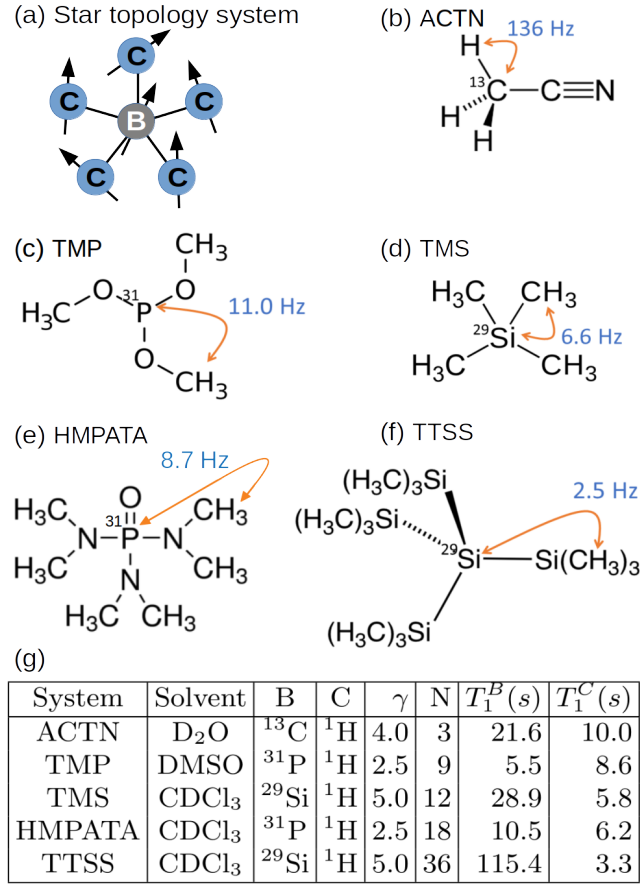


Figure 2.3: (a) Star-topology configuration showing the central battery spin symmetrically surrounded by charger spins. (b-f) The star-topology nuclear spin-systems studied in this work. The strength J of battery-charger interaction for each system is shown with the molecular structure, while other details are tabulated in (g). Note that all the nuclei considered here (B and C) are spin 1/2 nuclei.

of Eq. 2.1, i.e.,

$$\begin{aligned}
 \rho_{BC}(0) &= \rho_B(0) \otimes \rho_C(0), \text{ with} \\
 \rho_B(0) &= \frac{1+\epsilon}{2}|0\rangle\langle 0| + \frac{1-\epsilon}{2}|1\rangle\langle 1| \text{ and} \\
 \rho_C(0) &= \left(\frac{1-\gamma\epsilon}{2}|0\rangle\langle 0| + \frac{1+\gamma\epsilon}{2}|1\rangle\langle 1| \right)^{\otimes N},
 \end{aligned} \tag{2.16}$$

where ϵ and $\gamma\epsilon$ are the purity factors of the battery and charger spins respectively. Under the high-temperature approximation relevant for NMR conditions, $\epsilon \approx 10^{-5}$.

We evolve the whole system for a duration τ under the total Hamiltonian in the interaction

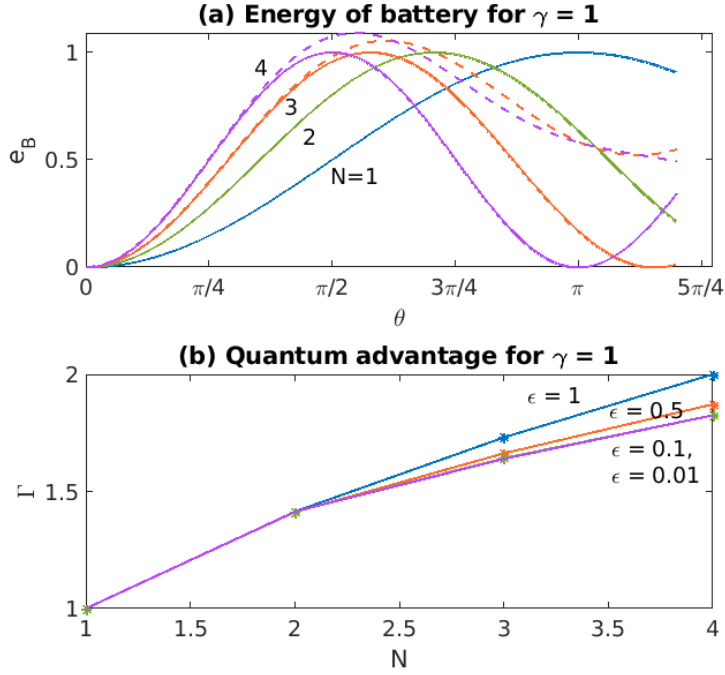


Figure 2.4: (a) Battery energy e_B versus charging phase $\theta = 2\pi J\tau$ for different number N of charger spins in pure (solid lines) as well as mixed (dashed lines; $\epsilon = 10^{-5}$) state cases. (b) Quantum advantage Γ versus N for different purity values ϵ .

frame defined by $U_{\text{IF}}(t) = e^{-i(H_B + H_C)t/\hbar}$. The dimensionless energy of the battery

$$e_B(\tau) = E_B(\tau)/\hbar\omega_B = \langle 1 | \rho_B(\tau) | 1 \rangle \quad (2.17)$$

is related to the normalized polarization of the battery

$$m_B(\tau) = \langle \sigma_z \rangle_{\rho_B(\tau)} / \epsilon \quad \text{via} \quad e_B(\tau) = \frac{1 - m_B(\tau)}{2}. \quad (2.18)$$

For the special case of pure state, i.e., $\epsilon = 1$ and also setting $\gamma = 1$, we obtain the state and dimensionless energy as

$$\rho_B(\tau) = \cos^2(\sqrt{N}\theta/2) |0\rangle\langle 0| + \sin^2(\sqrt{N}\theta/2) |1\rangle\langle 1| \quad (2.19)$$

$$e_B(\tau) = \sin^2(\sqrt{N}\theta/2) \text{ in terms of } \theta = 2\pi J\tau. \quad (2.20)$$

The energy is maximized for $\bar{\theta} = \pi/\sqrt{N}$ at optimal time

$$\bar{\tau}_N = \frac{\bar{\theta}}{2\pi J} = \frac{1}{2J\sqrt{N}}, \quad \therefore \quad \Gamma = \frac{\bar{\tau}_1}{\bar{\tau}_N} = \sqrt{N}, \quad (2.21)$$

clearly predicting the quantum speed-up. The battery energy evolution for various numbers of charger spins are shown in Fig. 2.4 (a). Note that mixed state curves deviate from the pure state curves for $N \geq 3$. Here, while e_B exceeds the pure state value of unity, the maximum charging takes longer duration. The quantum advantage Γ versus number of charger spins for $\gamma = 1$ and various values of ϵ are shown in Fig. 2.4 (b).

2.4 Experiments

2.4.1 Establishing quantum advantage

Our first aim is to establish the quantum advantage described in section 2.3.2 using various systems shown in Fig. 2.3. The table containing information about the solvent, the relative gyromagnetic ratio (γ), and the T_1 relaxation time constant for each of the spin systems is shown in Fig. 2.3 (g). All the experiments were carried out in a 500 MHz Bruker NMR spectrometer at an ambient temperature of 298 K. The NMR pulse-sequence for the experiments is shown in Fig. 2.5 (a). Starting from thermal equilibrium state, we energize the charger spins by inverting their populations with the help of a π pulse. This is followed by the charging propagator

$$\begin{aligned} U_{XY}(\tau/n_0) &= e^{-iH_{BC}\tau/n_0} \\ &\approx Y \cdot ZZ \cdot Y^\dagger \cdot X \cdot ZZ \cdot X^\dagger. \end{aligned} \quad (2.22)$$

Here, $X(Y) = e^{-i(S_{x(y)} + I_{x(y)})\pi/2}$ and $ZZ = e^{-iS_z I_z \theta/m}$. Note that for $N \geq 2$, $[S_x I_x, S_y I_y] \neq 0$, and therefore we implement the interaction propagator via integral iterations $n \in [0, n_0]$ of $U_{XY}(\tau/n_0)$ with sufficiently large n_0 such that $\tau/n_0 \ll 1/(2J)$. Finally, after dephasing spurious coherences with the help of a pulsed-field-gradient (PFG), we apply a $\pi/2$ detection pulse and measure the battery polarization $m_B(\tau)$. During the detection period, we decouple charger spins using WALTZ-16 composite pulse sequence [111].

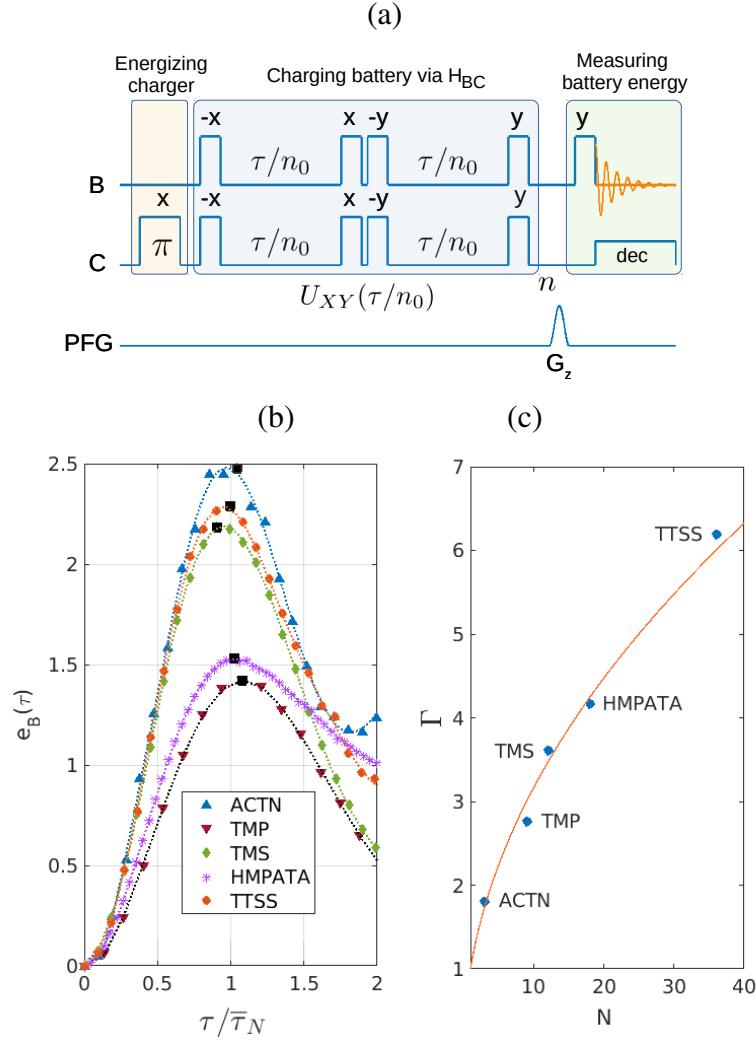


Figure 2.5: (a) The NMR pulse sequence for charging quantum battery and measuring its energy. The wide and narrow rectangular pulses correspond to π and $\pi/2$ pulses respectively. The shaped pulse in the lowest row corresponds to the pulsed-field-gradient (PFG) which dephases the coherences and retains populations. (b) The dots correspond to experimentally measured battery energy values e_B versus normalized charging duration τ/τ_N for the five spin-systems shown in Fig. 2.3. Here the solid lines are spline-fits to guide the eye. (c) Quantum advantage Γ versus the number N of charger spins showing \sqrt{N} dependence.

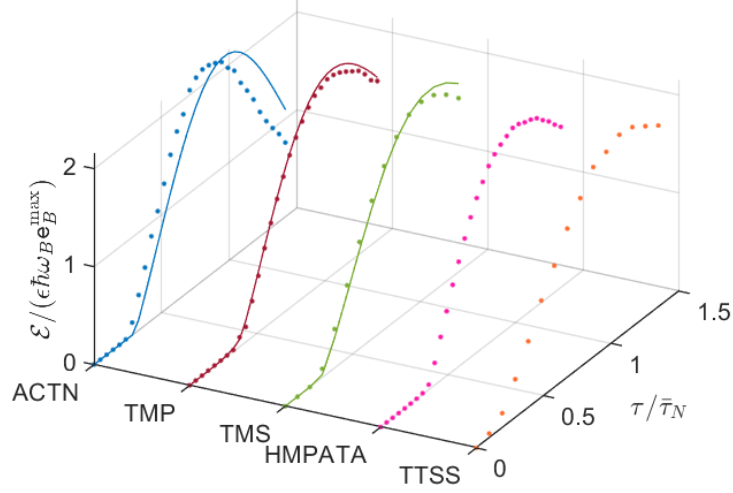


Figure 2.6: The dots represent the experimentally estimated ergotropy of the battery-spin versus normalized charging duration $\tau/\bar{\tau}_N$ for all five spin-systems. Here the ergotropy is scaled by $\epsilon\hbar\omega_B e_B^{\max}$ (see Eq. 2.13), where e_B^{\max} is taken from Fig. 2.5(b) indicated by filled squares. The solid lines in small spin-systems represent the theoretical fits accounting also for the experimental nonidealities.

The experimentally measured battery energy e_B estimated from m_B using Eq. 2.18 for all five spin-systems shown in Fig. 2.3 are plotted versus normalized charging duration $\tau/\bar{\tau}_N$ in Fig. 2.5 (b). For an ideal pure-state system, we expect the maximum energy storage at $\tau/\bar{\tau}_N = 1$. On the other hand, for mixed state systems with $N \geq 3$, $\tau/\bar{\tau}_N$ slightly overshoots the unit value. However, in practical systems, the charging dynamics is affected by the experimental imperfections such as RF inhomogeneity (RFI), off-set and calibration errors, etc. In spite of these issues, the results shown in Fig. 2.5 (b) for all the systems show a remarkable agreement with the expected maximum charging duration at $\bar{\tau}_N$. The corresponding quantum advantage Γ for all the systems are plotted versus the number N of charger spins in Fig. 2.5 (c), where the solid line corresponds to the theoretically expected \sqrt{N} function. Clearly, we observe a significant quantum advantage ranging from about 1.5 to over 6.

We now explain the experimental measurement of ergotropy for the subsystem consisting only the battery spin. To this end, we carry out the complete quantum state tomography [64] of the battery spin while tracing out the charger spins using heteronuclear composite pulse decoupling. After reconstructing the density matrix $\rho_B(\tau)$ we use Eqs. (4.1-2.9) to estimate the ergotropy value. The dots in Fig. 2.6 represent the experimentally estimated ratio of ergotropy to maximum energy (see Eq. 2.13) plotted versus the normalized charging time $\tau/\bar{\tau}_N$. Here the solid lines are

theoretical fits accounting for experimental nonidealities such as RFI, relaxation effects, etc. As explained after Eq. 2.11, the battery spin remains in a passive state and exhibits zero ergotropy until its populations are saturated. Ideally for $\gamma = 1$, the saturation occurs at time $1/(4J\sqrt{N})$ (follows from Eq. 2.19), while for $\gamma \geq 1$, it occurs earlier. Once the battery-spin populations begin to invert, the ergotropy ratio starts building up towards the value 2 (see Eq. 2.13) and reaches its maximum at normalized charging time $\tau/\bar{\tau}_N = 1$. Thus, once again we observe the quantum advantage in charging of quantum battery.

2.4.2 Determining size of the correlated cluster

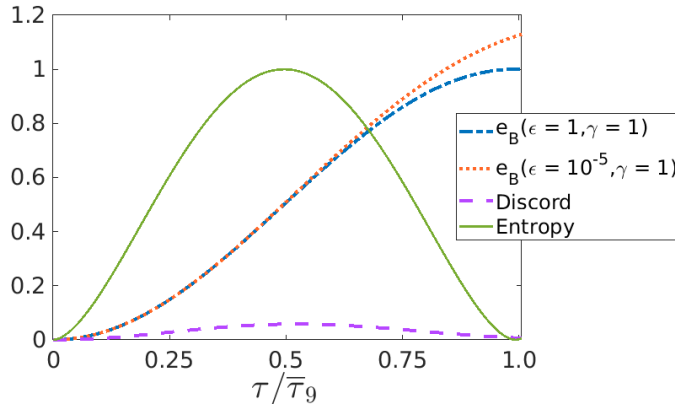


Figure 2.7: Numerically calculated battery energy (with pure and mixed states), entanglement entropy (for pure state; $\epsilon = 1$, $\gamma = 1$), and quantum discord (for mixed state; $\epsilon = 10^{-5}$, $\gamma = 1$) versus the normalized charging duration $\tau/\bar{\tau}_9$ for $N = 9$ star-system involving a single battery spin and nine charger spins.

It has been shown that quantum correlation plays a key role while charging quantum battery via collective mode [74]. The same holds true for charging in the star-topology system. In Fig. 2.7, we plot entanglement entropy as well as quantum discord against the normalized charging time $\tau/\bar{\tau}_9$ for a star-system with $N = 9$ charger spins. For reference we also show the charging energy e_B for both pure (with $\epsilon = 1$, $\gamma = 1$) and mixed state (with $\epsilon = 10^{-5}$, $\gamma = 1$). To evaluate entanglement entropy we traced out charger spins, and evaluated the von Neumann entropy of the battery state. For evaluating quantum discord, we used the two-spin reduced state obtained by tracing out all spins except the battery spin and one of charger spins. We find that the maximum correlation is reached at $\tau/\bar{\tau}_9 = 0.5$, i.e., at half the maximum charging period. Both entanglement entropy and discord vanish at maximum charging period, i.e., $\tau/\bar{\tau}_9 = 1$, and the spins get

uncorrelated [48, 74]. Since (i) the quantum advantage is linked to the generation of correlated state [74] and (ii) the maximum charging period depends on the size of the correlated cluster, here we propose to use $\Gamma^2 + 1$ as an estimate for size of the correlated cluster. This is justified by the good agreement between the theory and experiment for all the five systems investigated in Fig. 2.5 (b) and (c). For example, the experimentally obtained value $\Gamma \approx 6$ for TTSS matches with the correlated cluster of 37 spins.

2.4.3 Asymptotic charging

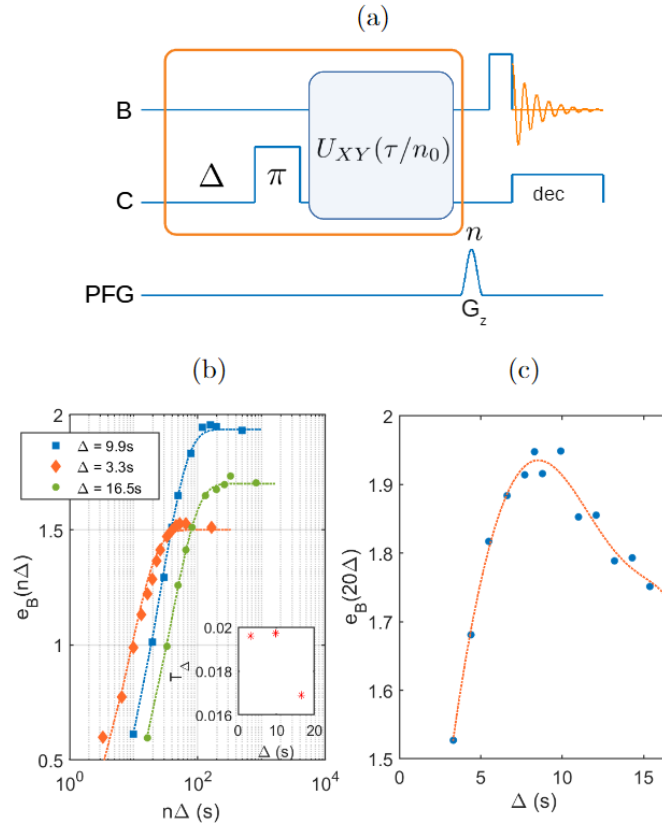


Figure 2.8: (a) The NMR pulse sequence for asymptotic charging of a quantum battery. (b) Battery energy e_B versus charging duration $n\Delta$ for three values of delay Δ . Here the dashed lines represent the fits to asymptotic charging functions as described in the text. The charging time-constants for these three cases are plotted in the inset. (c) Battery energy at saturation $e_B(20\Delta)$ (after $n = 20$ iterations) versus the delay Δ showing the optimal delay range from 7.5 s to 10 s. Here the dashed line is a spline curve fit to guide the eye.

We now propose a simple method to avoid oscillatory charging and realize an asymptotic charging that keeps the quantum battery from discharging. The method relies on the differen-

tial storage times of the charger and the battery spins, i.e., $T_1^B \gg T_1^C$. It involves iteratively re-energizing the chargers followed by transferring the charge to the quantum battery after a carefully chosen delay. The scheme for the asymptotic charging is described by the pulse-sequence shown in Fig. 2.8 (a). It involves a delay Δ before energizing the charger followed by charging the battery. However, unlike the unitary scheme described in section 2.4.1, here the entire process including waiting time, re-energizing of the battery, and charging is iterated. The experimentally measured battery energy e_B of the asymptotic charging with TTSS system are shown by dots in Fig. 2.8 (b), wherein the dashed lines represent the fits to asymptotic charging functions $e_B(n\Delta) = e_B^\Delta(1 - e^{-n\Delta/T_\Delta})$. Note that for TTSS, $T_1^B = 115.4$ s which is much longer than $T_1^C = 3.3$ s (see Fig. 2.3 (g)). The estimated values of the charging time-constants T_Δ is plotted versus Δ in the inset of Fig. 2.8 (b). It is clear that there is an optimal delay time Δ for which we observe maximum charging. Therefore, we monitored the saturation charging, i.e., $e_B(20\Delta)$ versus the delay time Δ as shown in Fig. 2.8 (c). For TTSS, we find the optimal delay ranges from 7.5 s to 10 s, to asymptotically achieve over 85 % charging compared to the simple unitary method described in section. 2.4.1.

2.4.4 Quantum Charger-Battery-Load (QCBL) Circuit

Now we describe the QCBL circuit consisting of charger (C), battery (B), as well as a load (L). Here we again use TTSS system, and consider all the proton spins together as charger, the central ^{29}Si spin as the battery, and the peripheral ^{29}Si spin as the load. Given the 5% natural abundance of ^{29}Si , the probability of both central and one of the four peripheral silicon nuclei to be ^{29}Si isotope is 0.2%. In this system, the strength of the ^{29}Si - ^{29}Si interaction, i.e., $J_{BL} = 52.4$ Hz. The QCBL circuit and the corresponding spin labeling are illustrated on the left of Fig. 2.9 (a). The NMR pulse-sequence for QCBL is shown on the right side of Fig. 2.9 (a). We first charge the battery (B) as described in Sec. 2.4.1 and switch-off the C-B interactions by decoupling the charger spins throughout. Subsequently, we can introduce a battery storage duration τ_s , after which we apply a Gaussian spin-selective $\pi/2$ pulse on L followed by a PFG (G_{1z}). This ensures that there is no residual polarization of the load (L) spin. We now introduce the discharging scheme $U_{XY}(\tau')$ between B and L. Note that, the U_{XY} propagator can be exactly implemented in the case of two-spin interaction. Finally, we measure the polarizations of both B and L spins after

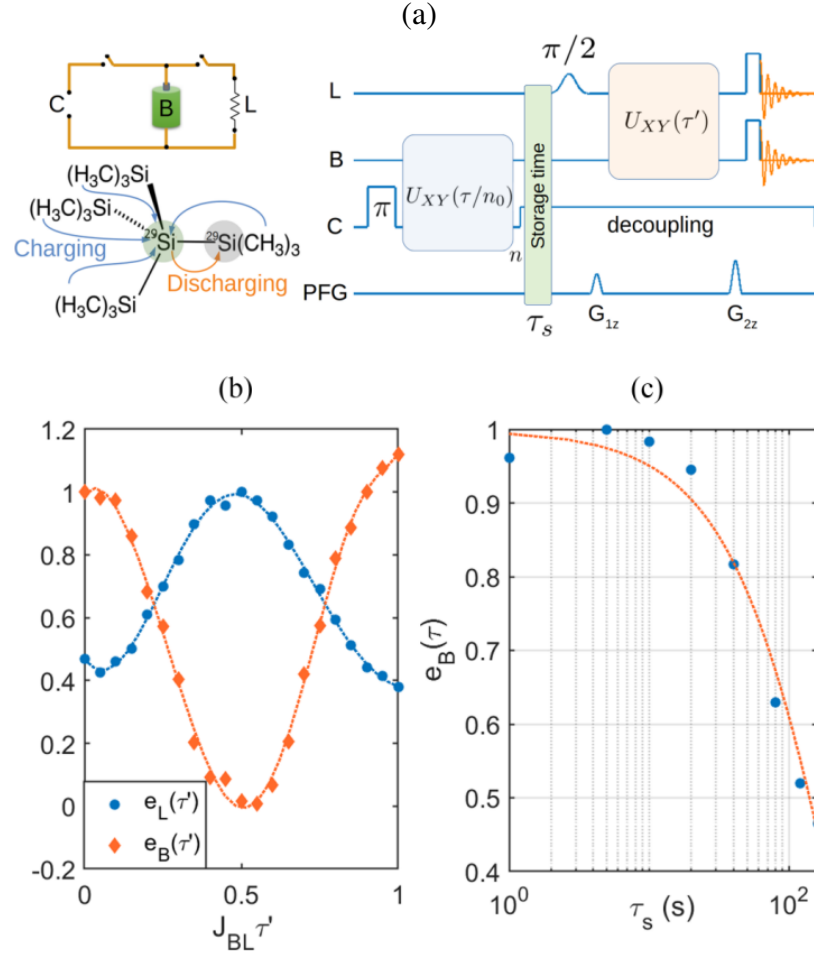


Figure 2.9: (a) The QCBL circuit and its implementation in the 38-spin star-topology system (left) and the NMR pulse sequence for the QCBL circuit (right). Here the dashed lines are spline curve fits to guide the eye. (b) The energy of battery (e_B) and load (e_L) versus discharging parameter $J_{BL}\tau'$. (c) The energy of the load (e_L) extracted from the battery after a storage time τ_s . The dashed line is an exponential fit as discussed in the text.

destroying the spurious coherences using a second PFG G_{z2} , and thereby estimate their energies e_B and e_L respectively. The experimental results of e_B and e_L are plotted versus $J_{BL}\tau'$ in Fig. 2.9 (b). In our experiment, the load spin is beginning from a maximally mixed state instead of the ground state. Therefore, e_L starts with a value around 0.5 before raising towards the maximum value of 1.0 for $J_{BL}\tau' = 0.5$. At this value of $J_{BL}\tau'$, we vary the battery storage time τ_s and monitor the load energy e_L . The results are shown in Fig. 2.9 (c). As expected, the data fits to an exponential decay function $e^{-\tau_s/T_s}$ (dashed line in Fig. 2.9 (c)) with an estimated battery storage time-constant $T_s \approx 200$ s. This completes the demonstration of QCBL circuit.

2.4.5 Effects of Dissipation on Quantum Battery Performance

Quantum batteries interact with their surrounding environment and are thus best modelled as open quantum systems. Such interactions introduce *dissipation*, which can manifest as amplitude damping, phase noise (dephasing), and thermal fluctuations [28, 112].

Impact on Energy Storage and Charging Dynamics

- **Energy leakage:** Dissipative processes cause energy loss into the environment, reducing the total stored energy and the extractable work (ergotropy) of the battery [113].
- **Damped charge oscillations:** Coherent charging oscillations decay over time, slowing the rate of energy accumulation [114].
- **Finite equilibrium energy:** In the long-time limit, dissipation drives the system toward thermal equilibrium, capping the maximum achievable stored energy regardless of charger drive strength [115].

Collective and Engineered Dissipative Effects

- **Collective robustness:** In many-body battery setups, collective effects can preserve advantages in charging power even in the presence of dissipation—and may improve with increasing system size [116].
- **Reservoir-engineered enhancement:** Carefully engineered dissipation can stabilize coherences and even accelerate charging, converting noise into a beneficial resource [117].

Mathematical Framework Open-system dynamics are modeled using the Lindblad master equation:

$$\dot{\rho} = -\frac{i}{\hbar}[H, \rho] + \sum_i \gamma_i \left(L_i \rho L_i^\dagger - \frac{1}{2} \{L_i^\dagger L_i, \rho\} \right).$$

Here, $\{L_i\}$ are jump operators representing dissipative interactions, and γ_i are decay rates [112].

2.5 Summary and outlook

Considering the potential applications of quantum technologies, it is of great interest to study energy storage and usage at the quantum level. In this context, there is a significant contemporary interest in studying quantum battery. We investigated various aspects of quantum battery using nuclear spin systems in star-topology molecules in the context of NMR architecture. We first theoretically compared the efficiency of the collective charging scheme (involving quantum correlation) with parallel (classical) scheme.

Using NMR methods, we experimentally studied collective charging scheme in a variety of spin-systems, each having a single battery spin and a set of charger spins whose number N ranged between 3 and 36. By measuring the polarization of the battery spin, we estimated the battery energy and thereby established the quantum advantage $\Gamma = \sqrt{N}$ of the collective charging scheme.

An important parameter to characterize a quantum battery is ergotropy, which quantifies the maximum amount of work that can be extracted from a quantum system via unitary methods. For each spin-system, we performed the experimental quantum state tomography and estimated the ergotropy of the battery spin and its evolution during charging. We observed the \sqrt{N} quantum advantage in ergotropy as well.

By numerically evaluating entanglement entropy and quantum discord for star-systems, we reconfirmed the established fact that the quantum advantage is realized via quantum correlation. Therefore, we proposed using $\Gamma^2 + 1$ as an estimate for the size of the correlated cluster. In particular, for a 37 spin-system, we obtained an experimental value of $\Gamma \approx 6$, which in this case matched well with the expected number.

We then addressed the issue of oscillatory charging wherein the battery starts discharging after overshooting the optimal charging duration. To this end, we proposed a simple asymptotic charging method that involves iteratively re-energizing the charger with a suitable delay. We experimentally demonstrated asymptotic charging and determined the optimal delay range.

Finally, we introduced a load spin to which the battery can deposit its energy after a suitable storage time, thus completing the complete charger-battery-load circuit. Using a 38-spin system, we showed that the battery spin can store energy for up to two minutes and yet was able to transfer the stored energy to the load spin.

We believe this work paves the way for further methodology developments towards the practical aspects of quantum batteries. Such developments may also contribute towards better understanding of quantum thermodynamics and its applications. One may also envisage an advanced circuit involving multiple elements such as quantum diodes, quantum transistors, and quantum heat engines, in addition to quantum batteries.

CHAPTER 3

Verification of many-body entanglement in NMR

Abstract

The phenomenon of quantum entanglement underlies several important protocols that enable emerging quantum technologies. Entangled states, however, are extremely delicate and often get perturbed by tiny fluctuations in their external environment. Certification of entanglement is therefore immensely crucial for the successful implementation of protocols involving this resource. In this work, we propose a set of entanglement criteria for multi-qubit systems that can be easily verified by measuring certain thermodynamic quantities. In particular, the criteria depend on the difference in optimal global and local works extractable from an isolated quantum system under global and local interactions, respectively. As a proof of principle, we demonstrate the proposed scheme on nuclear spin registers of up to 10 qubits using the Nuclear Magnetic Resonance architecture. We prepare noisy Bell-diagonal state and noisy Greenberger–Horne–Zeilinger class of states in star-topology systems and certify their entanglement through our thermodynamic criteria. Along the same line, we also propose an entanglement certification scheme in many-body systems when only partial or even no knowledge about the state is available.

Reported in

Jitendra Joshi, Mir Alimuddin, T S Mahesh and Manik banik, *Experimental verification of many-body entanglement using thermodynamic quantities*, [Phys. Rev. A 109, L020403](#).

3.1 Introduction

Quantum entanglement, identified as a puzzling feature of multipartite quantum systems [118–121], plays the pivotal role in a number of important quantum information protocols [122–128]

(see also [129]). In quantum systems involving more than two parts entanglement appears in different inequivalent and exotic forms [130, 131], that have been proved to be useful in several distributed protocols [132–141]. However, entangled states are fragile and easily lost by external perturbations. Successful implementation of the protocols involving entanglement, therefore, demands faithful certification of entanglement. Although the generic *separability problem* is known to be extremely hard even for bipartite systems [142], negative-partial-transposition (NPT) criterion [40, 143] and sometimes measurement of entanglement witness operator [144] become useful for certifying entanglement. On the other hand, there exist entropic quantities that also serve the purpose of entanglement certification [145, 146]. However, these entropic quantities are not directly measurable in experiments, and calculating the value of witness operator & evaluating NPT-ness of a state demands complete tomographic knowledge which is practically impossible when large number of subsystems are involved.

During the recent past, in a completely different approach, researchers are trying to identify operationally motivated thermodynamic quantities that can capture the signature of entanglement in multipartite quantum systems [47, 147–152]. In this work we show that suitably defined functions of such a thermodynamic quantity, namely the ergotropic work, can serve as bona-fide entanglement certifiers for generic N -qubit systems. The optimal amount of work extractable from an isolated quantum system by keeping its entropy unchanged is known as ergotropic work [153]. Depending upon whether a many-body quantum system is addressed globally or its parts are addressed separately, different kinds of ergotropic works can be extracted. Interestingly, entanglement of the initially prepared multipartite state keeps its footprints in the difference of these global and local ergotropic works. Furthermore, while extracting work one might infer the spectral of the state in question. Depending on the available information about the spectral of the global state and its marginals we propose several entanglement certifiers. As proof of principle, we implement the proposed thermodynamic entanglement criterion on nuclear spin registers of up to 10 qubits via Nuclear Magnetic Resonance (NMR) architecture. In particular, the star-topology systems allow preparation of Greenberger–Horne–Zeilinger (GHZ) class of states in large registers [154–156]. We prepare two-qubit Bell diagonal state and noisy states comprising of singlet/GHZ state and white noise, and certify their entanglement through our proposed criteria.

3.2 Objectives

In this project we establish an entanglement certification protocol for multi-qubit system and testify its validity using nuclear spin qubits.

- (i) Using thermodynamic quantities we first establish an entanglement certification protocol for multi-qubit system analytically.
- (ii) We implement the proposed thermodynamic entanglement criterion on nuclear spin registers of up to 10 qubits via NMR architecture.
- (iii) We prepare two-qubit Bell diagonal state and noisy states comprising of singlet/GHZ state and white noise, and certify their entanglement through our proposed criteria.

3.3 Theory

3.3.1 Majorization based entanglement criteria

In this section we briefly review the majorization based entanglement criteria as relevant to the present work. The concept of majorization has been extensively studied in mathematics [157], and its applications span across various domains, including quantum information theory. For instance, majorization plays a crucial role in detecting bipartite entanglement (through Nielsen-Kempe criteria [158]), quantum state transformation [159–161], quantum thermodynamics [162], and more. Here, we shortly recall the concept of majorization. We will denote a probability distribution $\{p_i\}_{i=0}^{n-1}$ as a vector $\vec{p} \equiv \{p_i\}_{i=0}^{n-1} \in \mathbb{R}^n$ with the elements arranged in decreasing order, *i.e.*, $p_{i+1} \geq p_i, \forall i \in \{0, \dots, n-1\}$.

Definition 1 A probability distribution \vec{p} majorizes another probability distribution \vec{q} , denoted as $\vec{p} \succ \vec{q}$, if and only if

$$\sum_{i=0}^k p_i \geq \sum_{i=0}^k q_i, \forall k \in \{0, \dots, n-2\}; \text{ \& } \sum_{i=0}^{n-1} p_i = \sum_{i=0}^{n-1} q_i. \quad (3.1)$$

If dimensions of the two vectors are not same extra zeros need to be appended to check their majorization relation.

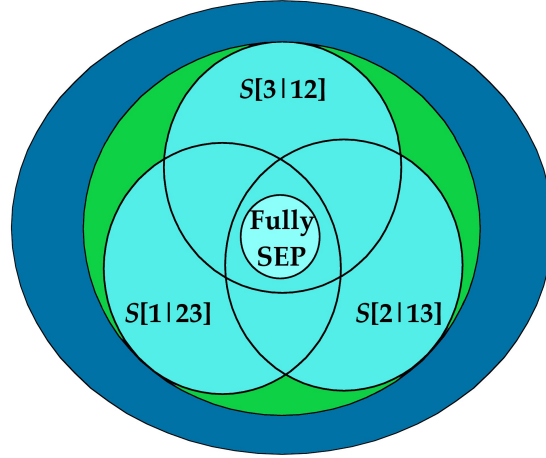


Figure 3.1: Entanglement in three qubit noisy GHZ states: The diagram illustrates various types of entanglement within three qubit systems. The large blue disc represents the complete state space of the three qubit system. The subset $\mathcal{S}[X|X^c]$, where $X \in 1, 2, 3$, denotes a convex set that encompasses states separable across the partition of X versus X^c . A state is considered bi-separable if it resides within $\text{CovHul}\{\mathcal{S}[1|1^c], \mathcal{S}[2|2^c], \mathcal{S}[3|3^c]\}$. On the other hand, if a state can be expressed as a convex combination of tripartite product states it is called fully separable. It is worth noting that the intersecting region $\cap_{X=1}^3 \mathcal{S}[X|X^c]$ is separable across all partitions. Interestingly, it is known that the set of fully separable states is a strict subset of $\cap_{X=1}^3 \mathcal{S}[X|X^c]$ [32]. In this analysis, we examine the entanglement region of three qubit noisy GHZ states. These states are fully separable if and only if $0 \leq p \leq \frac{1}{5}$. For $\frac{1}{5} < p \leq \frac{3}{7}$, the states are bi-separable but only reside in the green region, which re-establishes the fact that the set $\text{CovHul}\{\mathcal{S}[1|1^c], \mathcal{S}[2|2^c], \mathcal{S}[3|3^c]\}$ strictly contains $\cup_{X=1}^3 \mathcal{S}[X|X^c]$. Conversely, states are genuinely entangled if and only if $p > \frac{3}{7}$.

Definition 2 A quantum state $\rho \in \mathcal{D}(\mathbb{X})$ majorizes another quantum state $\sigma \in \mathcal{D}(\mathbb{Y})$, denoted as $\rho \succ \sigma$, if and only if spectral vector \vec{p}_ρ of the state ρ majorizes the spectral vector \vec{p}_σ of the state σ , i.e., $\vec{p}_\rho \succ \vec{p}_\sigma$.

Interestingly, Nielsen and Kempe provided a useful separability criteria based on majorization [158].

Nielsen-Kempe criteria: Any bipartite separable state $\rho_{AB} \in \mathcal{D}(\mathbb{X}_A \otimes \mathbb{Y}_B)$ satisfies

$$\vec{p}_{\rho_A} \succ \vec{p}_{\rho_{AB}}, \quad \& \quad \vec{p}_{\rho_B} \succ \vec{p}_{\rho_{AB}}. \quad (3.2)$$

Here $\rho_A := \text{Tr}_B[\rho_{AB}]$ and $\rho_B := \text{Tr}_A[\rho_{AB}]$. Violation of any one of these criteria implies the state ρ_{AB} is entangled. This condition can also be applied to certify entanglement across any bipartition of a multipartite state $\rho_{A_1 \dots A_N} \in \mathcal{D}(\otimes_i \mathbb{C}^{d_i})$. Recall that, $\mathcal{S}[X|X^c]$ denotes the set to states that are separable across X -vs- X^c cut, with X containing κ parties and X^c containing

the remaining parties; and Nielsen-Kempe criteria can be applied by considering the global state $\rho_{A_1 \dots A_N}$ and the parts ρ_X & ρ_{X^c} . A state is genuinely entangled if it lies outside the convex hull (CovHul) of all biseparable states. For instance, consider the N -qubit noisy GHZ states

$$\rho_{(\lambda, N)} = \lambda |\psi\rangle\langle\psi|_{GHZ} + (1 - \lambda) \frac{I}{2^N}, \quad (3.3)$$

where $|\psi\rangle_{GHZ} = \frac{1}{\sqrt{2}}|0\rangle^{\otimes N} + \frac{1}{\sqrt{2}}|1\rangle^{\otimes N}$ and $\lambda \in [0, 1]$. The states in this class are fully separable *if and only if* $0 \leq p \leq \frac{1}{1+2^{N-1}}$ [163], and genuinely entangled *if and only if* $\frac{1-2^{1-N}}{2-2^{1-N}} < p \leq 1$ [164]. Using Nielsen-Kempe criteria it can be concluded that the state exhibits entanglement across the $(N - 1)$ -vs-1 partition when the value of $p > \frac{1}{1+2^{N-1}}$. In the intermediate region, specifically when $\frac{1}{1+2^{N-1}} < p \leq \frac{1-2^{1-N}}{2-2^{1-N}}$, the state is observed to be bi-separable across the $(N - 1)$ -vs-1 partition. Nevertheless, due to the symmetrical nature of this class, all the $(N - 1)$ -vs-1 partitions exhibit entanglement but not genuine entanglement (refer to Fig. 3.1).

3.3.2 A: State dependent thermodynamic criteria of entanglement

State of an N -qubit system is described by a density operator $\rho_{A_1 \dots A_N} \in \mathcal{D}((\mathbb{C}^2)^{\otimes N})$; where $\mathcal{D}(\mathbb{H})$ denote the set of positive trace-one operators acting on the Hilbert space \mathbb{H} . A state is called fully separable if it is a probabilistic mixture of fully product state, *i.e.*, $\rho_{A_1 \dots A_N} = \sum_i p_i \left(\bigotimes_{j=1}^N |\psi_{A_j}^i\rangle\langle\psi_{A_j}^i| \right)$, with $|\psi_{A_j}^i\rangle \in \mathbb{C}_{A_j}^2 \equiv \mathbb{C}^2$. States lying outside the set of fully separable states are entangled. However, different kinds of entanglement are possible in multi-qubit systems. Let $\mathcal{S}[X|X^c]$ denotes the set of states separable across X -vs- X^c bipartite cut, where X contain κ parties together and X^c contains the remaining parties; $\kappa \in \{1, \dots, N - 1\}$. States lying outside $\mathcal{S}[X|X^c]$ contains entanglement across X -vs- X^c bipartition.

When an isolated such system evolves from an initial state ρ to a lower energy state σ , the difference in energies can be extracted as work. Study of this topic dates back to late seventies [46, 165] and it gains renewed interest in the recent past [166–169]. Consider an N -qubit system governed by non-interacting Hamiltonian $H = \sum_{l=1}^N \tilde{H}_l$, where $\tilde{H}_l := \mathbf{I}_1 \otimes \dots \otimes \mathbf{I}_{l-1} \otimes H_l \otimes \mathbf{I}_{l+1} \otimes \dots \otimes \mathbf{I}_N$, with $H_l = \sum_{i=0}^1 (E_l + i\alpha_l) |i\rangle\langle i|$ and $|0\rangle$ & $|1\rangle$ being the energy eigenkets with respective eigenvalues E_l and $E_l + \alpha_l$; \mathbf{I}_j be the identity operator on j^{th} qubit. Evolution from the initial state to final state is governed through a cyclic unitary $U(\tau)$ generated by switching

on a time dependent interaction. The optimally extractable work, called ergotropy, amounts to $W(\rho) = \text{Tr}[\rho H] - \min_{U(\tau)} \text{Tr}[U(\tau)\rho U^\dagger(\tau)H]$, where optimization is considered over all unitaries. As it turns out during optimal work extraction the system evolves to the passive state ρ^P , and accordingly we have, $W(\rho) := E(\rho) - E(\rho^P) = \text{Tr}[\rho H] - \text{Tr}[\rho^P H]$ [46, 165]. Passive state is the lowest energetic state with spectral identical to the initial state. Moreover, it is diagonal in energy basis where higher energy states are lessly populated. In multipartite scenario different parts of the system can be probed separately leading to several inequivalent configuration for work extraction. For instance, in the X -vs- X^c configuration, with X containing κ parties together, the optimal extractable work from X subsystem is given by, $W_{[\kappa]}(\rho_X) := \text{Tr}[\rho_X H_X] - \text{Tr}[\rho_X^P H_X]$, where $\rho_X := \text{Tr}_{X^c}(\rho) \in \mathcal{D}((\mathbb{C}^2)^{\otimes \kappa})$, $\rho \in \mathcal{D}((\mathbb{C}^2)^{\otimes N})$, H_X is the Hamiltonian of the subsystem X , ρ_X^P is the passive state corresponding to ρ_X , with $W_{[N]}(\rho)$ simply denoted as $W(\rho)$.

We will denote the spectral for a generic N -qubit state ρ as $\vec{t}_\rho \equiv \{t_j\}_{j=0}^{2^N-1}$, arranged in decreasing order. System's Hamiltonian H can be re-expressed as $H = \sum_{j=0}^{2^N-1} (E_g + n_j)|e_j\rangle\langle e_j|$, where $|e_0\rangle = |0\rangle^{\otimes N}$ is the ground state with energy value $E_g = \sum_{l=1}^N E_l$, and the energy eigenvalues are arranged in increasing order, i.e. $n_{j+1} \geq n_j$, $\forall j$, with $n_0 = 0$. The highest excited state $|e_{2^N-1}\rangle = |1\rangle^{\otimes N}$ has energy value $E_g + \sum_{l=1}^N \alpha_l$. Spectral of the subsystem X will be denoted as $\vec{x}_{\rho_X} \equiv \{x_j\}_{j=0}^{2^\kappa-1}$, with its Hamiltonian re-expressed as $H_X = \sum_{j=0}^{2^\kappa-1} (E_g^X + m_j)|f_j\rangle\langle f_j|$. While extracting work in X -vs- X^c configuration, we can evaluate the thermodynamic quantity

$$\Delta_{X|X^c} := W(\rho) - W_{[\kappa]}(\rho_X) - E(\rho_{X^c}) + E_g^{X^c}. \quad (3.4)$$

Here the first three terms are state dependent and their values can be evaluated through experiment; the last term designates the ground state energy of the Hamiltonian of the X^c part. We are now in a position to provide our thermodynamic entanglement criteria.

Theorem 1 *An N -qubit state separable across X -vs- X^c bipartition satisfies*

$$\Delta_{X|X^c} \leq \sum_{i=1}^{2^\kappa-1} (m_i - m_1)x_i + \sum_{i=1}^{2^N-1} (m_1 - n_i)t_i := \delta_{X|X^c}^{GL}, \quad (3.5a)$$

$$\Delta_{X|X^c} \leq \sum_{i=1}^{2^\kappa-2} (m_i - n_i)t_i + \sum_{i=2^\kappa-1}^{2^N-1} (m_{2^\kappa-1} - n_i)t_i := \delta_{X|X^c}^G, \quad (3.5b)$$

where, $m_{i+1} \geq m_i$ for $i \in \{0, 2^\kappa - 1\}$, $n_{i+1} \geq n_i$ for $i \in \{0, 2^N - 1\}$, and $m_{2^\kappa-1} = \sum_{i=1}^\kappa \alpha_i$.

proof : The quantity $\Delta_{X|X^c}$ in Eq.(3.4) reads as

$$\begin{aligned}
 \Delta_{X|X^c} &= \{\text{Tr}[\rho H] - \text{Tr}[\rho^p H]\} - \{\text{Tr}[\rho_X H_X] - \text{Tr}[\rho_X^p H_X]\} \\
 &\quad - E(\rho_{X^c}) + E_g^{X^c} \\
 &= \sum_{i=0}^{2^\kappa-1} m_j x_j - \sum_{i=0}^{2^N-1} n_j t_j + E_g^{X^c} + E_g^X - E_g \\
 \Delta_{X|X^c} &= \sum_{i=1}^{2^\kappa-1} m_j x_j - \sum_{i=1}^{2^N-1} n_j t_j.
 \end{aligned} \tag{3.6}$$

According to Nielsen-Kempe separability criteria a state separable across X -vs- X^c cut satisfies $\rho_X \succ \rho$, i.e.,

$$x_0 \geq t_0, \Rightarrow \sum_{i=1}^{2^\kappa-1} x_i \leq \sum_{i=1}^{2^N-1} t_i. \tag{3.7}$$

Substituting Eq.(3.7) in Eq.(3.6) we obtain

$$\Delta_{X|X^c} \leq \sum_{i=1}^{2^\kappa-1} (m_i - m_1) x_i + \sum_{i=1}^{2^N-1} (m_1 - n_i) t_i := \delta_{X|X^c}^{GL}.$$

This is the entanglement criterion (2a) of Theorem 1. Evaluation of this criterion requires information about the spectral of the global state as well as spectral of the X -marginal. One can, however, achieve a entanglement criterion depending on the global spectral only. For that, rewrite Eq.(3.6) as

$$\Delta_{X|X^c} = \sum_{i=1}^{2^\kappa-1} m_j x_j + \sum_{j=1}^{2^\kappa-1} (m_j - m_{j-1}) \sum_{i=j}^{2^\kappa-1} x_i - \sum_{j=1}^{2^\kappa-1} (m_j - m_{j-1}) \sum_{i=j}^{2^\kappa-1} x_i - \sum_{i=1}^{2^N-1} n_j t_j.$$

Substituting the separability condition $\sum_{i=j}^{2^\kappa-1} x_i \leq \sum_{i=j}^{2^N-1} t_i$ we obtain,

$$\begin{aligned}
\Delta_{X|X^c} &\leq \sum_{i=1}^{2^\kappa-1} m_j x_j + \sum_{j=1}^{2^\kappa-1} (m_j - m_{j-1}) \sum_{i=j}^{2^N-1} t_i - \sum_{j=1}^{2^\kappa-1} (m_j - m_{j-1}) \sum_{i=j}^{2^\kappa-1} x_i - \sum_{i=1}^{2^N-1} n_j t_j \\
&= \sum_{j=1}^{2^\kappa-1} (m_j - m_{j-1}) \sum_{i=j}^{2^N-1} t_i - \sum_{i=1}^{2^N-1} n_j t_j \\
&= \sum_{i=1}^{2^\kappa-2} (m_i - n_i) t_i + \sum_{i=2^\kappa-1}^{2^N-1} (m_{2^\kappa-1} - n_i) t_i \\
&:= \delta_{X|X^c}^G.
\end{aligned}$$

This is the condition (2b) of Theorem 1; and this completes the proof. Violation of any of the conditions in Theorem 1 certifies entanglement across X -vs- X^c bipartition.

Note that, the criterion (2a) and the criterion (2b) help us to detect entanglement at X -vs- X^c cut in the following way. For a given state ρ , if the values of thermodynamic quantity $\Delta_{X|X^c}$ of Eq.(3.4) exceeds the separability bound $\delta_{X|X^c}^{GL}$ then the state is entangled, and the thermodynamic criteria turns out to be equivalent to some conditions of Nielsen-Kempe criteria:

$$\begin{aligned}
\sum_{i=1}^{2^\kappa-1} m_j x_j - \sum_{i=1}^{2^N-1} n_j t_j &> \sum_{i=1}^{2^\kappa-1} (m_i - m_1) x_i + \sum_{i=1}^{2^N-1} (m_1 - n_i) t_i \\
&\Rightarrow \sum_{i=1}^{2^\kappa-1} x_i > \sum_{i=1}^{2^N-1} t_i \Rightarrow x_0 < t_0.
\end{aligned} \tag{3.8}$$

Please note that, examining condition (3.5a) requires knowledge of the global and local spectrals \vec{t}_ρ and \vec{x}_{ρ_X} . Quite interestingly this thermodynamic criterion turns out to be a special case of Nielsen-Kempe entanglement criterion [158] (see Remark 1. The separability bound $\delta_{X|X^c}^G$ in (3.5b) depends only on the global spectral of the given state (and hence the superscript ‘G’) and generally turns out to be a weaker than (3.5a).

Remark 1 For the N -qubit noisy GHZ state of Eq. (3.3) entanglement across X -vs- X^c bipartition can be certified by comparing the values of $\Delta_{X|X^c}$ and $\delta_{X|X^c}^{GL}$. As it turns out according to this test the state is entangled for $\lambda > \lambda_\kappa^{GL} := \frac{2^{N-\kappa}-1}{2^{N-1}+2^{N-\kappa}-1}$, where the X subsystem contains

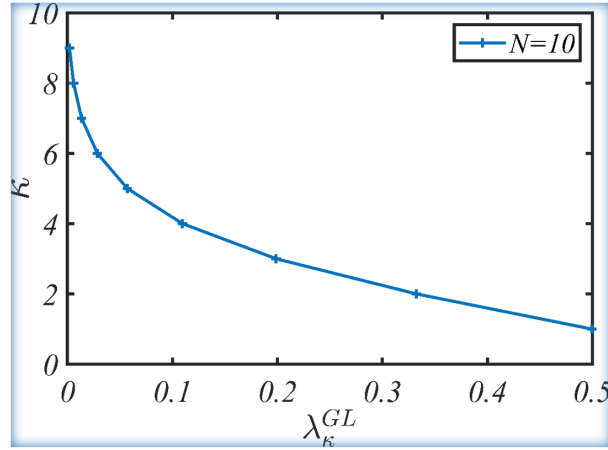


Figure 3.2: A plot of global and local spectral dependent entanglement threshold (λ_{κ}^{GL}) across X -vs- X^c bi-partition versus the number of subsystems (κ) in the X part.

κ qubits. Important to note that the bound λ_{κ}^{GL} depends on the value of κ . As more subsystems are considered in the X part, the criteria will encompass a broader range of entanglement, as illustrated in Fig. 3.2. In the present example, our criteria will encompass the entire range of entanglement, just like the Nielsen-Kempe criteria, when we choose $\kappa = N - 1$.

Important to note that likewise Nielsen-Kempe criteria criterion, (2a) of Theorem 1 is independent of the Hamiltonian of the given system. However, as evident from Eq.(3.7) and the separability bound (2b), entanglement detection condition explicitly depends on the Hamiltonian (except for $\delta_{1|1^c}^G$, since it becomes equal to $\delta_{1|1^c}^{GL}$) as shown below,

$$\begin{aligned}
 \sum_{i=1}^{2^{\kappa}-1} m_i x_i - \sum_{i=1}^{2^N-1} n_i t_i &> \sum_{i=1}^{2^{\kappa}-2} (m_i - n_i) t_i + \sum_{i=2^{\kappa}-1}^{2^N-1} (m_{2^{\kappa}-1} - n_i) t_i \\
 \Rightarrow \sum_{i=1}^{2^{\kappa}-1} m_i x_i &> \sum_{i=1}^{2^{\kappa}-2} m_i t_i + m_{2^{\kappa}-1} \sum_{i=2^{\kappa}-1}^{2^N-1} t_i.
 \end{aligned} \tag{3.9}$$

3.3.3 B: State independent thermodynamic criteria of entanglement

Thermodynamic criteria provided in the Theorem 1 are spectral dependent and therefore entanglement certification through this criteria demands knowledge about the state in question. Next we will show that one can in-fact obtain spectral independent entanglement criterion, albeit weaker than spectral dependent criterion. But, the advantage is that one can invoke this state independent criterion to test entanglement of an unknown state. Such criteria generally depends on the Hamil-

tonian as well as the number of parties involved in the X -vs- X^c partition. Since it is difficult to analyze the most generic case in one go, in the following we analyze different systems one after another.

3.3.3.1 Two-qubit system

Consider a two-qubit system governed by the Hamiltonian

$$H = H_1 \otimes \mathbf{I} + \mathbf{I} \otimes H_2, \quad (3.10)$$

Proposition 1 *Any separable state of a two-qubit system governed by the Hamiltonian $H = H_1 \otimes \mathbf{I} + \mathbf{I} \otimes H_2$ satisfies the condition*

$$\Delta_{1|2} \leq \max\{(\alpha_1 - \alpha_2)/2, 0\} := \delta_{1|2}^I.$$

Here, $H_l := \sum_{i=0}^1 (E_l + i\alpha_l)|i\rangle\langle i|$, for $l = 1, 2$.

proof : In this case criterion (2b) of Theorem 1 boils down to

$$\Delta_{1|2} \leq \sum_{i=1}^3 (m_1 - n_i)t_i. \quad (3.11)$$

Depending upon the values of α_1 and α_2 several cases are possible which we analyze below.

(C-I) $\alpha_1 > \alpha_2 > 0$: In this case we have, $m_1 = \alpha_1$, $n_1 = \alpha_2$, $n_2 = \alpha_1$, $n_3 = \alpha_1 + \alpha_2$, and accordingly condition (3.11) becomes

$$\Delta_{1|2} \leq (\alpha_1 - \alpha_2)t_1 - \alpha_2 t_3. \quad (3.12)$$

As the global spectral $\vec{t} \equiv \{t_i\}_{i=0}^3$ are arranged in decreasing order, in the above inequality maximization occurs at $\vec{t} \equiv \{\frac{1}{2}, \frac{1}{2}, 0, 0\}$; and therefore we have the spectral independent criterion

$$\Delta_{1|2} \leq \frac{\alpha_1 - \alpha_2}{2} = \delta_{1|2}^I. \quad (3.13)$$

(C-II) $\alpha_1 = \alpha_2 = \alpha > 0$: Here we have $m_1 = \alpha$, $n_1 = \alpha$, $n_2 = \alpha$, $n_3 = 2\alpha$, and accordingly

condition (3.11) becomes

$$\Delta_{1|2} \leq -\alpha t_3. \quad (3.14)$$

In this case maximization occurs at $\vec{t} \equiv \{t_0, t_1, t_2, 0\}$ and thus we have

$$\Delta_{1|2} \leq 0 = \delta_{1|2}^I. \quad (3.15)$$

(C-III) $0 < \alpha_1 < \alpha_2$: $m_1 = \alpha_1, n_1 = \alpha_1, n_2 = \alpha_2, n_3 = \alpha_1 + \alpha_2$; and condition (3.11) reads as

$$\Delta_{1|2} \leq -(\alpha_2 - \alpha_1)t_2 - \alpha_2 t_3. \quad (3.16)$$

As maximization occurs at $\vec{t} \equiv \{t_0, t_1, 0, 0\}$, we have

$$\Delta_{1|2} \leq 0 = \delta_{1|2}^I. \quad (3.17)$$

Combining (3.13), (3.15), and (3.17), we therefore have

$$\Delta_{1|2} \leq \delta_{1|2}^I = \max \left\{ \frac{\alpha_1 - \alpha_2}{2}, 0 \right\}. \quad (3.18)$$

This completes the proof.

3.3.3.2 Three-qubit system

Consider a 3-qubit system with Hamiltonian

$$H = H_1 \otimes \mathbf{I} \otimes \mathbf{I} + \mathbf{I} \otimes H_2 \otimes \mathbf{I} + \mathbf{I} \otimes \mathbf{I} \otimes H_3, \quad (3.19)$$

with $H_i = \sum_{j=0}^1 (E_i + j\alpha_i)|j\rangle\langle j|$ for $i \in \{1, 2, 3\}$, and $\alpha_i > 0 \forall i$. Depending upon the values of $\{\alpha_i\}_{i=1}^3$ and depending on the bipartitions considered several cases are possible. In the following, we will analyze the cases relevant to our experiment.

Proposition 2 *Consider a 3-qubit system governed by the Hamiltonian (3.19). Any state of this*

system separable across 1-vs-23 bipartition satisfies the condition

$$\Delta_{1|23} \leq 0 := \delta_{1|23}^I, \quad \text{when } \alpha_1 < \alpha_2 = \alpha_3 := \alpha \quad (3.20a)$$

$$\Delta_{1|23} \leq \frac{\alpha - \alpha_3}{2} := \delta_{1|23}^I, \quad \text{when } \alpha_1 = \alpha_2 = \alpha > \alpha_3. \quad (3.20b)$$

proof : In this case, across 1-vs-23 cut the criterion (2b) of Theorem 1 reads as

$$\Delta_{1|23} \leq \sum_{i=1}^7 (m_1 - n_i) t_i. \quad (3.21)$$

(C-I) When $\alpha_1 < \alpha_2 = \alpha_3 = \alpha$, we have $m_1 = \alpha_1, n_1 = \alpha_1, n_2 = n_3 = \alpha, n_4 = n_5 = \alpha + \alpha_1, n_6 = 2\alpha, n_7 = 2\alpha + \alpha_1$, and accordingly above becomes

$$\Delta_{1|23} \leq -[(\alpha - \alpha_1)(t_2 + t_3) + \alpha(t_4 + t_5) + (2\alpha - \alpha_1)t_6 + 2\alpha t_7]. \quad (3.22)$$

Since the function $f := (\alpha - \alpha_1)(t_2 + t_3) + \alpha(t_4 + t_5) + (2\alpha - \alpha_1)t_6 + 2\alpha t_7$ is a linear in $\vec{t} \equiv \{t_i\}_{i=0}^7$, and since spectral are arranged in decreasing order, it is evident that f will take minimum value 0 at $\vec{t} \equiv (1, 0, 0, 0, 0, 0, 0)$. This proves the claim

$$\Delta_{1|23} \leq 0 = \delta_{1|23}^I. \quad (3.23)$$

(C-II) Similarly, for $\alpha_1 = \alpha_2 = \alpha > \alpha_3$ we have $m_1 = \alpha, n_1 = \alpha_3, n_2 = n_3 = \alpha, n_4 = n_5 = \alpha + \alpha_3, n_6 = 2\alpha, n_7 = 2\alpha + \alpha_3$, and accordingly condition (3.21) becomes

$$\Delta_{1|23} \leq (\alpha - \alpha_3)t_1 - \alpha_3(t_4 + t_5) - \alpha t_6 - (\alpha + \alpha_3)t_7. \quad (3.24)$$

In this case the function $g = (\alpha - \alpha_3)t_1 - \alpha_3(t_4 + t_5) - \alpha t_6 - (\alpha + \alpha_3)t_7$ takes maximum value at $\vec{t} \equiv (1/2, 1/2, 0, 0, 0, 0, 0)$, which further imply

$$\Delta_{1|23} \leq \frac{\alpha - \alpha_3}{2} = \delta_{1|23}^I.$$

This completes the proof.

Proposition 3 Consider a 3-qubit system governed by the Hamiltonian (3.19). Any state of this system separable across 12-vs-3 bipartition satisfies the condition

$$\Delta_{12|3} \leq \frac{\alpha_1}{4} := \delta_{12|3}^I, \quad \text{when } 0 < \alpha_1 < \alpha_2 = \alpha_3 := \alpha; \quad (3.25a)$$

$$\Delta_{12|3} \leq \frac{\alpha - \alpha_3}{4} + \frac{\alpha}{4} := \delta_{12|3}^I, \quad \text{when } \alpha_1 = \alpha_2 = \alpha > \alpha_3 > 0 \text{ and } \alpha_3 \geq \frac{2}{3}\alpha; \quad (3.25b)$$

$$\Delta_{12|3} \leq \frac{\alpha - \alpha_3}{2} + \frac{\alpha}{6} := \delta_{12|3}^I, \quad \text{when } \alpha_1 = \alpha_2 = \alpha > \alpha_3 > 0 \text{ and } \alpha_3 \leq \frac{2}{3}\alpha. \quad (3.25c)$$

proof : Criterion (2b) of Theorem 1 boils down to

$$\Delta_{12|3} \leq \sum_{i=1}^3 (m_i - n_i) t_i + \sum_{i=4}^7 (m_3 - n_i) t_i. \quad (3.26)$$

(C-I) For $0 < \alpha_1 < \alpha_2 = \alpha_3 = \alpha$, we have $m_1 = \alpha_1, m_2 = \alpha, m_3 = \alpha + \alpha_1, n_1 = \alpha_1, n_2 = n_3 = \alpha, n_4 = n_5 = \alpha + \alpha_1, n_6 = 2\alpha, n_7 = 2\alpha + \alpha_1$, and accordingly condition (3.26) becomes,

$$\Delta_{12|3} \leq \alpha_1 t_3. \quad (3.27)$$

As maximization occurs at $\vec{t} \equiv \{1/4, 1/4, 1/4, 1/4, 0, 0, 0, 0\}$, we have

$$\Delta_{12|3} \leq \frac{\alpha_1}{4} = \delta_{12|3}^I. \quad (3.28)$$

(C-II) For $0 < \alpha_1 < \alpha_2 = \alpha_3 = \alpha$, we have $m_1 = \alpha, m_2 = \alpha, m_3 = 2\alpha, n_1 = \alpha_3, n_2 = n_3 = \alpha, n_4 = n_5 = \alpha + \alpha_3, n_6 = 2\alpha, n_7 = 2\alpha + \alpha_3$, and accordingly condition (3.26) becomes,

$$\Delta_{12|3} \leq (\alpha - \alpha_3)(t_1 + t_4 + t_5) + \alpha t_3. \quad (3.29)$$

If $\alpha_3 \geq \frac{2}{3}\alpha$, maximization occurs at $\vec{t} \equiv \{1/4, 1/4, 1/4, 1/4, 0, 0, 0, 0\}$ and we have

$$\Delta_{12|3} \leq \frac{\alpha - \alpha_3}{4} + \frac{\alpha}{4} = \delta_{12|3}^I. \quad (3.30)$$

If $\alpha_3 \leq \frac{2}{3}\alpha$, maximization occurs at $\vec{t} \equiv \{1/6, 1/6, 1/6, 1/6, 1/6, 1/6, 0, 0\}$ and we have

$$\Delta_{12|3} \leq \frac{\alpha - \alpha_3}{2} + \frac{\alpha}{6} = \delta_{12|3}^I. \quad (3.31)$$

This completes proof of the claim.

Remark 2 *It is instructive to see an explicit example how the entanglement certification criteria get weakened with lesser amount of information about the state in question. For that, consider a three-qubit noisy GHZ state described in Eq. (3.3), where $N = 3$, and the Hamiltonian has the following specifications: $\alpha_1 = \alpha_2 = \alpha > \alpha_3 = 2\alpha/3$. Let's set $\kappa = 2$ and focus on the thermodynamic quantity $\Delta_{12|3}$ (Eq. 3.4). By comparing the values of $\Delta_{12|3}$ with $\delta_{12|3}^{GL}$ (2a), $\delta_{12|3}^G$ (2b) and $\delta_{12|3}^I$ (3.25b & 3.25c), we obtain the entanglement threshold values: $\lambda_{12|3}^{GL} = 1/5 < \lambda_{12|3}^G = 1/2 < \lambda_{12|3}^I = 4/5$, respectively. Beyond these threshold values, the state is entangled, and it is evident that the range of entanglement expands as our separability bound $\delta_{12|3}$ incorporates more information about the state.*

3.3.3.3 Ten-qubit system

Consider a 10-qubit system with Hamiltonian

$$H = \sum_{l=1}^{10} \tilde{H}_l; \text{ where } \tilde{H}_l := \mathbf{I}_1 \otimes \cdots \otimes \mathbf{I}_{l-1} \otimes H_l \otimes \mathbf{I}_{l+1} \otimes \cdots \otimes \mathbf{I}_{10}, \quad (3.32)$$

with $H_l = \sum_{i=0}^1 (E_l + i\alpha_l)|i\rangle\langle i|$. Our experiment considers a central qubit whose energy gap between excited and ground state is denoted by α_c and the rest qubits are identical where energy gap takes the value $\alpha > \alpha_c$.

Proposition 4 *Any state of this system separable across 1-vs-1^c bipartition satisfies the condition*

$$\Delta_{1|1^c} \leq 0 := \delta_{1|1^c}^I, \quad \text{when } \alpha_1 = \alpha_c < \alpha_j = \alpha \quad \forall j \neq 1 \quad (3.33a)$$

$$\Delta_{1|1^c} \leq \frac{\alpha - \alpha_c}{2} := \delta_{1|1^c}^I, \quad \text{when } \alpha_1 = \alpha. \quad (3.33b)$$

proof : In this case criterion (2b) of Theorem 1 boils down to

$$\Delta_{1|1^c} \leq \sum_{i=1}^{2^{10}-1} (m_1 - n_i) t_i. \quad (3.34)$$

Depending on the central qubit's arrangement in bi-partition two cases are possible.

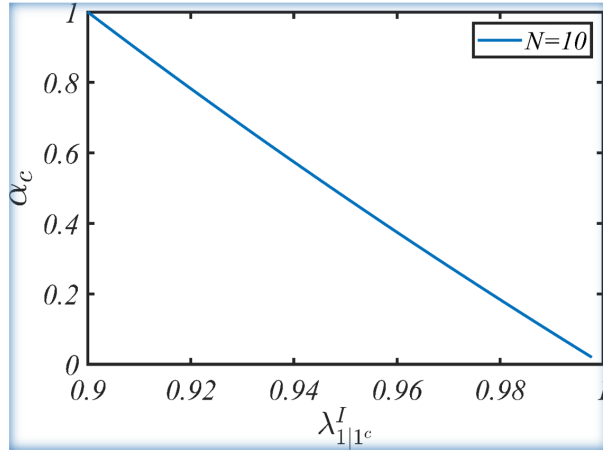


Figure 3.3: A plot of state independent entanglement threshold (λ_{κ}^{GL}) across 1-vs- 1^c bi-partition versus the energy difference in central qubit (α_c) for a ten-qubit system.

(C-I) $\alpha > \alpha_1 = \alpha_c > 0 : m_1 = \alpha_c, n_1 = \alpha_c, n_j \geq \alpha \ \forall j \neq 1$, and accordingly condition (3.34) becomes,

$$\Delta_{1|1^c} \leq - \sum_{i=2}^{2^{10}-1} (n_i - \alpha_c) t_i. \quad (3.35)$$

Note that maximization occurs at $\vec{t} \equiv \{t_0, t_1, t_3, t_k = 0\} \ \forall k \in \{4, \dots, 2^{10} - 1\}$ and we have

$$\Delta_{1|1^c} \leq 0 := \delta_{1|1^c}^I. \quad (3.36)$$

(C-II) $0 < \alpha_1 = \alpha : m_1 = \alpha, n_1 = \alpha_c, n_j \geq \alpha \ \forall j \neq 1$ and accordingly condition (3.34) becomes,

$$\Delta_{1|1^c} \leq (\alpha - \alpha_c) t_1 - \sum_{j=2}^{2^{10}-1} (n_j - \alpha_c) t_j. \quad (3.37)$$

In this case maximization occurs at $\vec{t} \equiv \{1/2, 1/2, t_k\} \ \forall k \in \{3, \dots, 2^{10} - 1\}$ and we have

$$\Delta_{1|1^c} \leq \frac{\alpha - \alpha_c}{2} := \delta_{1|1^c}^I. \quad (3.38)$$

This completes the proof.

Remark 3 It turns out that the state-independent value of purity ensuring entanglement varies with the energy difference between the ground and excited states of the central qubit (α_c). Let's consider an N -qubit noisy GHZ system (3.3) where $N - 1$ qubits are identical with energy pa-

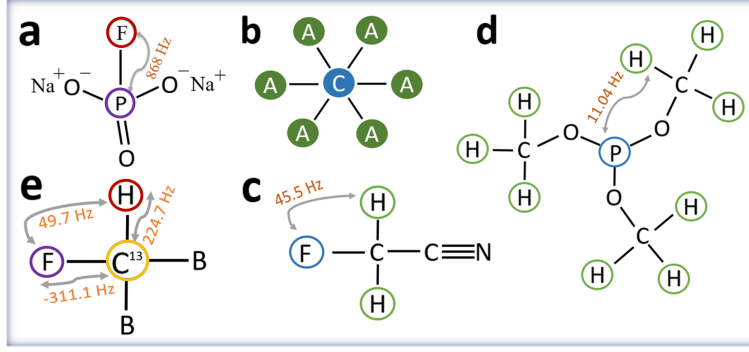


Figure 3.4: (Color Online) (a) 2-qubit system sodium fluoro-phosphate (NAFP, with ^{19}F and ^{31}P being first and second qubits) used in Experiment I. (b) The star topology configuration, wherein each ancillary spin A interacts with the central spin ^{13}C . (c,d) 3-qubit star-system fluoroacetonitril (FAN) and 10-qubit star-system trimethyl-phosphate (TMP) used in Experiment II. (e) Di-bromo fluoromethane (DBFM, with ^1H , ^{13}C , and ^{19}F being first, second, and third qubits) used in Experiment III.

parameter α , while the central qubit has $\alpha_c < \alpha$. By comparing the values of $\Delta_{1|1^c}$ with the separability bound $\delta_{1|1^c}^I$, we can determine that the entanglement threshold value is given by $\lambda_{1|1^c}^I = \frac{(N-1)\alpha}{\alpha_c + (N-1)\alpha}$. If the purity parameter λ exceeds this bound, we classify the state as entangled. Note that as α_c approaches to α , state independent thresh-hold value of purity $\lambda_{1|1^c}^I$ decreases and consequently more region of entanglement can be detected (see Fig.3.3).

3.4 Experiments

3.4.1 Experiment I: Two-qubit Bell diagonal states

In our first experiment we deal with two-qubit Bell diagonal states prepared using the system NAFP (Fig. 3.4 (a)) dissolved in D_2O . All the experiments were carried out on a 500 MHz Bruker NMR spectrometer at an ambient temperature of 300 K. Hamiltonian of the system consisting of the internal part and the RF drive reads as $H_{12} = H_{12}^{\text{int}} + H_{12}^{\text{RF}}$, where $H_{12}^{\text{int}} = -\omega_F I_{1z} - \omega_P I_{2z} + 2\pi J I_{1z} I_{2z}$ and $H_{12}^{\text{RF}} = \Omega_F(t) I_{1x} + \Omega_P(t) I_{2x}$, with $I_{ix} = \sigma_{ix}/2$, $I_{iy} = \sigma_{iy}/2$, $I_{iz} = \sigma_{iz}/2$. Here (ω_F, ω_P) and (Ω_F, Ω_P) respectively denote the Larmor frequencies and RF amplitudes of $(^{19}\text{F}, ^{31}\text{P})$, $\hbar = 1$, and J is the scalar coupling constant. We prepare Bell diagonal states with two independent controllable parameters β and γ . We start with the thermal state, which under high-field, high-temperature approximation reads as $\rho_{th} = \mathbf{I}/4 + \epsilon_P(\frac{\gamma_F}{\gamma_P} I_{1z} + I_{2z})$, where $\epsilon_P = \gamma_P B_0 / 4k_B T$. The method of spatial averaging yields us psuedo-pure state (PPS) $|11\rangle\langle 11|^{pps} = (1 - \epsilon)\mathbf{I}/4 + \epsilon|11\rangle\langle 11|$, with $\epsilon \ll 1$ (Fig.3.5 (a)). Within the paradigm of PPS we set $\epsilon = 1$

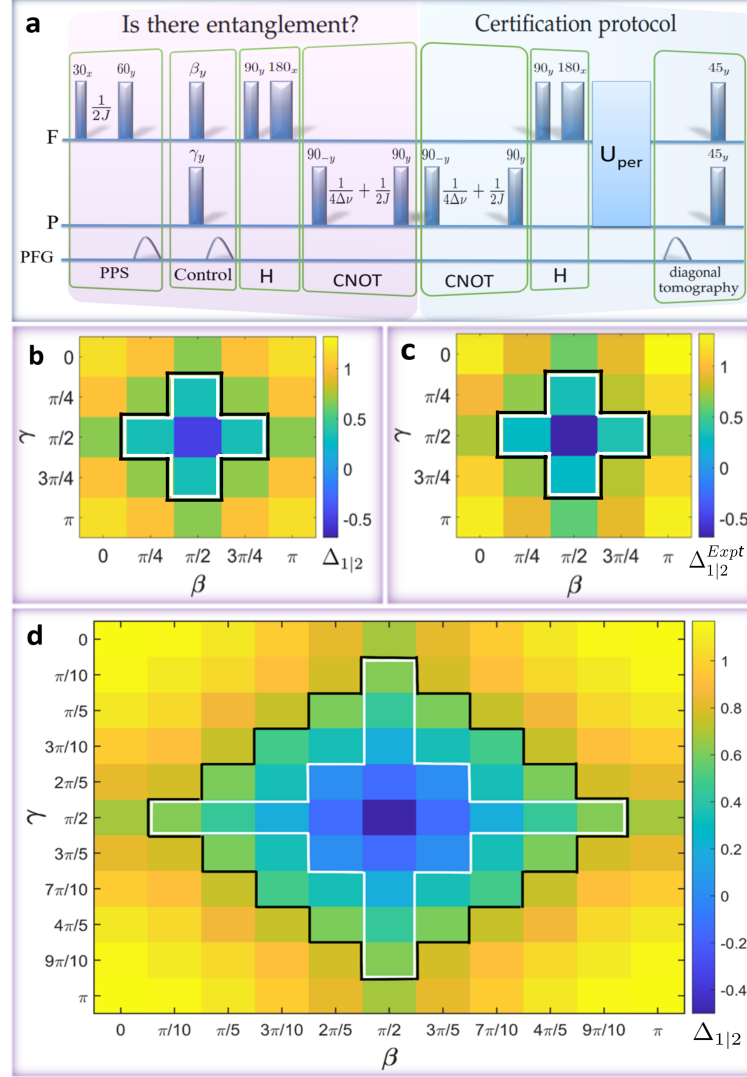


Figure 3.5: (Color Online) (a) The NMR pulse sequence to prepare Bell diagonal state with control parameter β and γ . Here PFG is the Pulsed-Field Gradient and $\Delta\nu$ is the resonance offset of both ^{19}F and ^{31}P . One of the operations $[U_{\text{per}} \circ H \circ \text{CNOT}]$ takes the Bell diagonal state to its passive. Detailed explanation of this sequence is given in the supplemental. (b) Gradient-color-plot for theoretical values of $\Delta_{1|2}$ (in units of ω_P) vs the control parameters β and γ . States outside the white line (inner-perimeter) are entangled as $\Delta_{1|2} > \delta_{1|2}^G$. For the states outside the black line (outer-perimeter) $\Delta_{1|2} > \delta_{1|2}^I$ and hence they are also entangled. (c) Gradient-color-plot for the experimental values of $\Delta_{1|2}^{Exp}$ with estimated errors of $\pm 0.1\omega_P$. Here error originates both from the spin system as well as the NMR hardware, accordingly we have estimated the random error from the experimental NMR spectrum corresponding to the least signal-to-noise ratio providing a useful upper bound for errors. (d) 11×11 pixel theoretical gradient-color-plot of $\Delta_{1|2}$: evidently state independent certification scheme is weaker than the state dependent scheme.

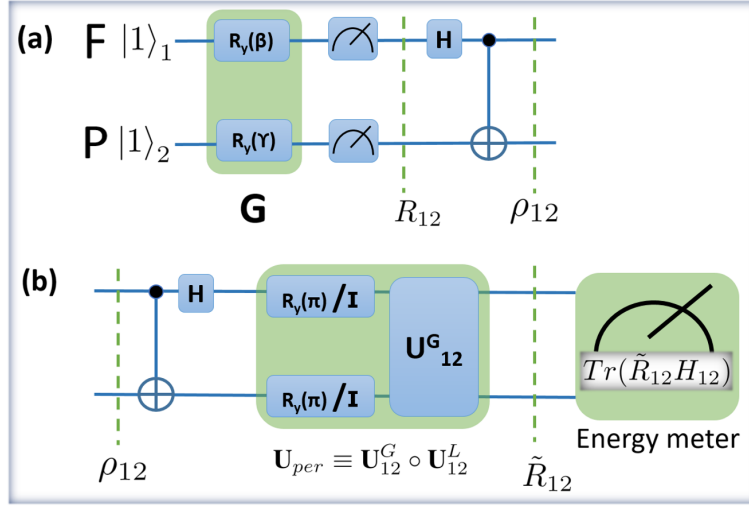


Figure 3.6: (a) Quantum circuit to prepare Bell-diagonal state ρ_{12} . Here $R_y(\alpha)$ is the rotation along y-axis with angle α and the unread measurement after G is equivalent to a crusher gradient that destroys all the coherence in x-y plane. (b) Simplified circuit with two independent parameters along with passive state ρ_{12}^p conversion.

and realize the effective state $|11\rangle\langle 11|$ [170]. Subsequently we prepare the two-parameter Bell diagonal state

$$\rho_{12} = \sum_{i,j=0}^1 p_{ij} |\mathcal{B}_{ij}\rangle\langle \mathcal{B}_{ij}|, \quad (3.39)$$

$$|\mathcal{B}_{0j}\rangle := (|00\rangle + (-1)^j |11\rangle) / \sqrt{2}, \quad p_{00} := [S(\beta/2)S(\gamma/2)]^2,$$

$$|\mathcal{B}_{1j}\rangle := (|01\rangle + (-1)^j |10\rangle) / \sqrt{2}, \quad p_{01} := [S(\beta/2)C(\gamma/2)]^2,$$

$$p_{10} := [C(\beta/2)S(\gamma/2)]^2, \quad p_{11} := [C(\beta/2)C(\gamma/2)]^2,$$

where $S(\star) := \sin(\star)$ and $C(\star) := \cos(\star)$.

Our aim is to certify entanglement of the prepared state through the thermodynamics entanglement criteria obtained in Theorem 1. For that we need to evaluate the following thermodynamic quantity from experiment:

$$\Delta_{1|2} := W(\rho_{12}) - W_{[\kappa]}(\rho_1) - E(\rho_2) + E_g^2. \quad (3.40)$$

To evaluate $W(\rho_{12})$, we need to apply a proper unitary so that the state ρ_{12} evolves to the lowest

energy state (*i.e.* the passive state). In case of an unknown state ρ_{12} finding the optimal unitary is quite tedious. However, for the Bell-diagonal state in the following we provide a systematic method to do the same. First we apply CNOT and Hadamard [see Fig.3.6(b)] to evolve ρ_{12} to

$$R_{12} = \sum_{i,j=0}^1 p_{ij} |ij\rangle\langle ij|, \quad (3.41)$$

which is diagonal in computational basis $\{|ij\rangle\}_{i,j=0}^1$. In the next step, we have to apply unitary operation that permutes the computational basis that accordingly leads us to the lowest energy state. As it turns out, in this case 24 different permutations \mathbf{U}_{per} are possible that can be represented as $\mathbf{U}_{per} \equiv \mathbf{U}_{12}^G \circ \mathbf{U}_{12}^L$, where

$$\mathbf{U}_{12}^G \in \{\mathbf{I}_{12}, \mathbf{CNOT}_1, \mathbf{CNOT}_2, \mathbf{CNOT}_1 \circ \mathbf{CNOT}_2, \mathbf{CNOT}_2 \circ \mathbf{CNOT}_1, \mathbf{CNOT}_1 \circ \mathbf{CNOT}_2 \circ \mathbf{CNOT}_1\}, \quad (3.42a)$$

$$\mathbf{U}_{12}^L \in \{\mathbf{I}_1 \otimes \mathbf{I}_2, \mathbf{I}_1 \otimes \mathbf{Y}_2, \mathbf{Y}_1 \otimes \mathbf{I}_2, \mathbf{Y}_1 \otimes \mathbf{Y}_2\}, \text{ with} \quad (3.42b)$$

$$\mathbf{Y}_s : \left\{ \begin{array}{l} |0\rangle_s \mapsto |1\rangle_s \\ |1\rangle_s \mapsto |0\rangle_s \end{array} \right\}; \quad \mathbf{CNOT}_1 : \left\{ \begin{array}{l} |00\rangle_{12} \mapsto |00\rangle_{12} \\ |01\rangle_{12} \mapsto |01\rangle_{12} \\ |10\rangle_{12} \mapsto |11\rangle_{12} \\ |11\rangle_{12} \mapsto |10\rangle_{12} \end{array} \right\}; \quad \mathbf{CNOT}_2 : \left\{ \begin{array}{l} |00\rangle_{12} \mapsto |00\rangle_{12} \\ |01\rangle_{12} \mapsto |11\rangle_{12} \\ |10\rangle_{12} \mapsto |10\rangle_{12} \\ |11\rangle_{12} \mapsto |01\rangle_{12} \end{array} \right\}; \quad (3.43)$$

and \mathbf{I} be the identity operation. The task now boils down to evaluating the energy of the state $\tilde{R}_{12} = \mathbf{U}_{per} R_{12} \mathbf{U}_{per}^\dagger$ for obtaining the lowest energy state by varying these 24 permutations. This completes the process of evaluating $W(\rho_{12})$. On the other hand, $W_{[\kappa]}(\rho_1)$ in this case becomes zero as ρ_{12} being the Bell-diagonal state we have $\rho_1 = \mathbf{I}/2$. Since the system's Hamiltonian is known the other two terms in left hand side of Eq.(3.40) can be evaluated immediately. Please note that, during the process we do not need to know the spectral of the given state since the expected energy value suffice the purpose. This experimentally obtained thermodynamic quantity $\Delta_{1|2}^{Expt}$ is plotted in Fig.2(c) of the main manuscript. Now to certify entanglement, we need to evaluate the separability bounds $\delta_{1|2}^G$ and $\delta_{1|2}^I$ for the given state ρ_{12} . We can also calculate $\Delta_{1|2}$

analytically to tally with our experiment. For the system in consideration with $H_{12}^{\text{int}} \approx -\omega_F I_{1z} - \omega_P I_{2z}$ where $J \ll (\omega_F, \omega_P)$ we have

$$\left\{ \begin{array}{l} x_0 = 1/2, \quad x_1 = 1/2, \quad m_0 = 0, \quad m_1 = \omega_F = \alpha_1, \quad n_0 = 0, \\ n_1 = \omega_P = \alpha_2, \quad n_2 = \omega_F, \quad n_3 = (\omega_F + \omega_P) \end{array} \right\}; \quad (3.44)$$

and accordingly we get

$$\Delta_{1|2} = m_1 x_1 - \left(\sum_{i=1}^3 n_i t_i \right) = [\omega_F/2 - (\omega_P t_1 + \omega_F t_2 + (\omega_P + \omega_F) t_3)], \quad (3.45a)$$

$$\delta_{1|2}^G = \sum_{i=1}^3 (m_1 - n_i) t_i = (\omega_F t_1 - \omega_P (t_1 + t_3)), \quad (3.45b)$$

$$\delta_{1|2}^I = \frac{\alpha_1 - \alpha_2}{2} = (\omega_F - \omega_P)/2, \quad (3.45c)$$

where vector $\vec{t} \equiv \{t_k\}_{k=0}^3$ is obtained by arranging $\{p_{ij}\}$ in descending order. Now, in 500MHz spectrometer we have, $\omega_F = 470.385\text{MHz}$ and $\omega_P = 202.404\text{MHz}$, which thus yield

$$\Delta_{1|2} = (1.162 - 2.324t_2 - 3.324t_3 - t_1)\omega_P, \quad (3.46a)$$

$$\delta_{1|2}^G = (1.324t_1 - t_3)\omega_P, \quad (3.46b)$$

$$\delta_{1|2}^I = 0.662\omega_P. \quad (3.46c)$$

This way we obtain the value of the quantity $\Delta_{1|2}^{\text{Expt}}$ experimentally. Notably as the number of qubits increases, the optimization over the set of possible unitary operations expands significantly, and hence the scalability issues persists.

Note that, evaluation of the quantity $\delta_{1|2}^G$ in Eq. 3.46(b) demands knowledge of the global spectral, whereas $\delta_{1|2}^I$ is state independent. Entanglement is certified whenever $\Delta_{1|2}$ is strictly greater than any one of these quantities. Varying the parameter β and γ we show the entanglement certification in Fig.3.5. through ‘gradient-color-plot’. As expected and also evident from the plot, the state independent certification scheme turns out to be weaker than the state dependent scheme. For instance, the specific values of $\beta = 2\pi/5$ and $\gamma = 3\pi/10$ yield $\Delta_{1|2} = 0.338\omega_P$, which is strictly less than $\delta_{1|2}^I = 0.662\omega_P$, but greater than $\delta_{1|2}^G = 0.292\omega_P$. This is not visible in Fig.3.5 (b)-(c) due to limited pixel resolution, but can be seen in Fig.3.5 (d). Important to note that, our

entanglement certification scheme does not require tomographic knowledge of the state, rather it is obtained by evaluating expected energies of the given state and the unitarily evolved state. More specifically, our thermodynamic entanglement criteria can certify entanglement in the given state without requiring the information of the population frequencies for different energy eigenstates. Following are some methodologies used in the experiments.

Preparation of PPS

We start with the thermal state, which under high-field, high-temperature approximation reads as $\rho_{th} = \mathbf{I}/4 + \epsilon_P(\frac{\gamma_F}{\gamma_P}I_{1z} + I_{2z})$, where $\epsilon_P = \gamma_P B_0/4k_B T$ and $\frac{\gamma_F}{\gamma_P} \approx 4/\sqrt{3}$. The identity part is invariant under the unitary transformations, neither contributes to the NMR signal, and is ignored henceforth. The PPS preparation (upto the scaling factor ϵ_P can be described as follows:

$$\begin{aligned}
\frac{1}{4}\mathbf{I} + \epsilon_P \left[\frac{4}{\sqrt{3}}I_{1z} + I_{2z} \right] &\xrightarrow{30_x^F} \frac{1}{4}\mathbf{I} + \epsilon_P \left[\frac{4}{\sqrt{3}}\frac{\sqrt{3}}{2}I_{1z} - \frac{4}{\sqrt{3}}\frac{1}{2}I_{1y} + I_{2z} \right] \\
&\xrightarrow{1/2J} \frac{1}{4}\mathbf{I} + \epsilon_P \left[2I_{1z} + \frac{4}{\sqrt{3}}I_{1x}I_{2z} + I_{2z} \right] \\
&\xrightarrow{60_y^F, \text{ PFG}} \frac{1}{4}\mathbf{I} + \epsilon_P [I_{1z} - 2I_{1z}I_{2z} + I_{2z}] \\
&\equiv (1 - \epsilon)\frac{1}{4}\mathbf{I} + \epsilon|11\rangle\langle 11|. \tag{3.47}
\end{aligned}$$

Control of p_{ij}

Using notations $C_\theta = \cos \theta$ & $S_\theta = \sin \theta$,

$$\begin{aligned}
 & \frac{1}{4}\mathbf{I} + \epsilon_P [I_{1z} - 2I_{1z}I_{2z} + I_{2z}] \xrightarrow{\beta_y^F, \gamma_y^P, \text{PFG}} \frac{1}{4}\mathbf{I} + \epsilon_P [C_\beta I_{1z} - C_\beta C_\gamma 2I_{1z}I_{2z} + C_\gamma I_{2z}] \\
 &= \frac{1}{4}\mathbf{I} + \epsilon_P \frac{1}{2} \begin{bmatrix} C_\beta + C_\gamma - C_\beta C_\gamma & & & \\ & C_\beta - C_\gamma + C_\beta C_\gamma & & \\ & & -C_\beta + C_\gamma + C_\beta C_\gamma & \\ & & & -C_\beta - C_\gamma - C_\beta C_\gamma \end{bmatrix}, \\
 &= \frac{1}{4}\mathbf{I} + \epsilon_P \frac{1}{2} \begin{bmatrix} 1 - 4p_{00} & & & \\ & 1 - 4p_{01} & & \\ & & 1 - 4p_{10} & \\ & & & 1 - 4p_{11} \end{bmatrix} \equiv \sum_{i,j \in \{0,1\}} p_{ij} |ij\rangle \langle ij| \quad (3.48)
 \end{aligned}$$

up to the uniform background population within the PPS paradigm.

Hadamard operation

The Hadamard operation on F is realized by

$$U_{180_x} U_{90_y} = \exp(-i\pi I_x) \exp(-i\pi I_y/2) = H, \text{ up to a global phase.} \quad (3.49)$$

Implementing CNOT

$$\begin{aligned}
 U_{\text{CNOT}} &= U_y U_{zz} U_{z12}^\dagger U_y^\dagger \\
 &= \exp(-i\pi I_{2y}/2) \exp(-i\pi I_{1z} I_{2z}) \exp(i\pi (I_{1z} + I_{2z})/2) \exp(i\pi I_{2y}/2). \quad (3.50)
 \end{aligned}$$

In our experiment, local z-rotations U_{z12}^\dagger was realized by introducing a temporary resonance offset of $\Delta\nu = 10000$ Hz for a duration $1/(4\Delta\nu) = 25\mu\text{s}$. Similarly, the bilinear rotation U_{zz} was realized by using the J -Hamiltonian $H_J = 2\pi J I_{1z} I_{2z}$ evolving for time $1/(2J)$ as indicated in the pulse sequence.

Implementing U_{per}

The U_{per} operator has a sequence of nonlocal CNOT gates and local 90_y rotations as described in Eq. 3.46. These are implemented in the same way as described in the previous steps.

Detection:

The final 45 degree y-pulse allows the measurement of not only linear I_{iz} terms, but also bilinear $I_{1z}I_{2z}$ term:

$$\begin{aligned} I_{iz} &\xrightarrow{45_y} I_{ix}, \\ I_{iz}I_{iz} &\xrightarrow{45_y} \frac{1}{\sqrt{2}} (I_{ix}I_{iz} + I_{iz}I_{ix}), \end{aligned} \quad (3.51)$$

both the cases leading to single-quantum observable NMR signals. For 90_y pulse, the bilinear term becomes $I_{1x}I_{2x}$ which is a combination of zero- and two-quantum coherence and hence not directly observable.

3.4.2 Experiment I-b: Two-qubit Werner state

As of special interest, in this experiment we addresses entanglement certification in two-qubit Werner class of states. For that, we use a two-qubit homo-nuclear spin system of 5-Bromothiophene-2-Carbaldehyde (BRTP) dissolved in Dimethyl Sulphoxide (DMSO) [see Fig. 3.7(a)]. All the experiments are carried out on a 500 MHz Bruker NMR spectrometer at an ambient temperature of 300 K. The Hamiltonian of the system can be written in terms of the internal part and the RF drive as

$$H_{12} = H_{12}^{\text{int}} + H_{12}^{\text{RF}}, \quad \text{where} \quad (3.52a)$$

$$\begin{aligned} H_{12}^{\text{int}} &= -(\omega_H + \pi\Delta\nu) I_{1z} - (\omega_H - \pi\Delta\nu) I_{2z} + 2\pi J I_{1z} I_{2z} \\ &\approx -\omega_H (I_{1z} + I_{2z}), \quad \text{for } (J, \Delta\nu) \ll \omega_H, \quad \text{and} \end{aligned} \quad (3.52b)$$

$$H_{12}^{\text{RF}} = \Omega_H(t) (I_{1x} + I_{2x}). \quad (3.52c)$$

Here ω_H denotes the Larmor frequency of proton, $\Delta\nu$ is the chemical shift difference between the two spins, J denotes the scalar coupling constant, and Ω_H denotes the RF amplitude. In

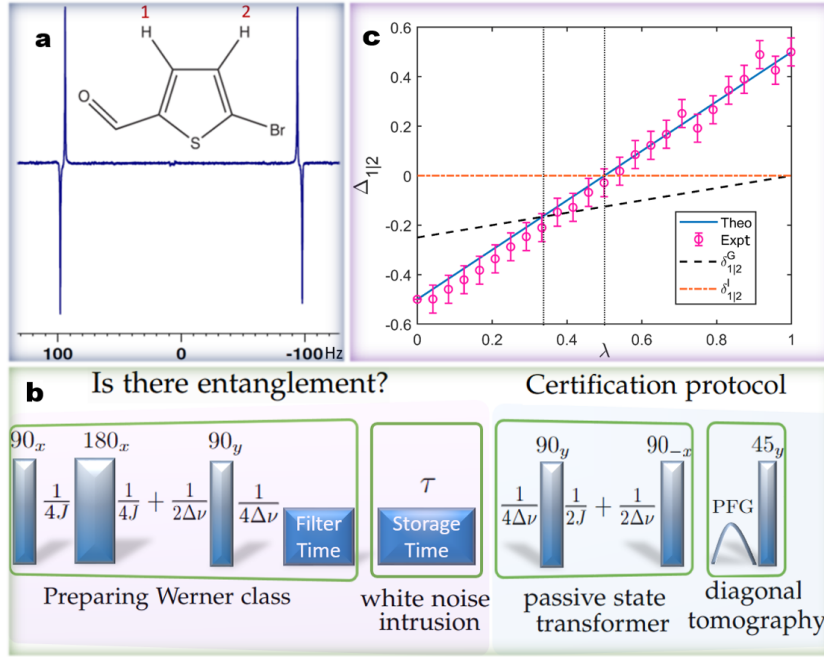


Figure 3.7: (a) The ^1H spectrum corresponding to the singlet or Werner state of pair of hydrogen spins BRTP. (b) The NMR pulse sequence to produce Werner class states with controlled purity and then to certify the presence or absence of entanglement. Here rectangles with $\Theta_\beta = e^{-i\Theta(I_{1\beta} + I_{2\beta})}$ represent RF rotations, delays represent free-evolutions, and PFG is the Pulsed-Field Gradient. Here a short filter time of a few seconds is used to allow the decay of triplet state thereby retaining high-fidelity singlet state [171]. The final 45 degree y-pulse allows the measurement of not only linear I_{iz} terms, but also bilinear $I_{1z}I_{2z}$ term. (c) Plot of $\Delta_{1/2}$ in units of ω_H versus purity of the Werner class. The vertical dotted lines indicate the purity threshold for entanglement: the left one marks purity $\lambda = 1/3$, above which $\Delta_{1/2}$ surpasses $\delta_{1/2}^G$ and the state becomes entangled; the right one marks $\lambda = 1/2$, corresponding to the state-independent bound $\delta_{1/2}^I$. The errorbar represents the estimated random error due to noise.

BRTP, $\omega_H = 500.2$ MHz, $\Delta\nu = 192$ Hz and $J = 4.01$ Hz. Using appropriate RF pulses, we can realize various local rotations and an entangling gate can be implemented through scalar coupling [see Fig. 3.7(b)]. When applied on a pure superposition state, the entangling gate can produce a singlet pair. Intrusion of white noise via decoherence lead to a noisy singlet state belonging in Werner class

$$\rho_\lambda := \lambda|\psi^-\rangle\langle\psi^-| + (1 - \lambda)\mathbf{I}/4, \quad \lambda \in [0, 1], \quad \text{where } |\psi^-\rangle = \frac{1}{\sqrt{2}}(|01\rangle - |10\rangle). \quad (3.53)$$

Now criterion 3.5b can certify entanglement for the parameter values $\lambda > 1/3$, whereas a state independent thermodynamic criterion can detect entanglement for the parameter ranges $\lambda > \frac{\omega_H}{2\omega_H} = 1/2$.

To prepare the Werner class of state in BRTP system, we start with thermal state, which under high-field, high-temperature approximation ($\hbar\omega_H \ll k_B T$) reads as $\rho_{th} = \mathbf{I}/4 + \epsilon_H(I_{1z} + I_{2z})$, where $\epsilon_H = \omega_H/4k_B T$. We then prepare the long-lived singlet state (LLS) by applying suitable pulse sequence as shown in the preparation part of Fig. 3.7(b),

$$\begin{aligned}\rho_{LLS} &= \frac{\mathbf{I}}{4} - \epsilon_H(I_{1x}I_{2x} + I_{1y}I_{2y} + I_{1z}I_{2z}) \\ &= (1 - \epsilon_H)\frac{\mathbf{I}}{4} + \epsilon_H|\psi^-\rangle\langle\psi^-|. \end{aligned} \quad (3.54)$$

As the name suggests, LLS outlives any other nonequilibrium state [172]. In BRTP, LLS decay constant T_{LLS} is 12.9 s, which is considerably longer than the individual T_1 values (longitudinal relaxation time constants) of 6.1 s and 8.2 s. Thus, after the filter time shown in Fig. 3.7(b), we obtain a clean state in the above form of Eq. (3.54) [171]. Since LLS is isomorphic to a pure singlet, we invoke the paradigm of pseudo-pure states [170] and set $\epsilon_H = 1$. Thus our reference state at time $t = 0$ is $\rho_{\lambda(0)} \equiv |\psi^-\rangle\langle\psi^-|$. During the storage time, white noise intrusion takes place and the singlet state gradually becomes more and more mixed Werner state, i.e., $\rho_{\lambda(\tau)} = (1 - \lambda(\tau))\mathbf{I}/4 + \lambda(\tau)|\psi^-\rangle\langle\psi^-|$, where $\lambda(\tau) = e^{-\tau/T_{LLS}}$ is the purity factor of Werner class.

To evaluate global ergotropic work $W[\rho_{\lambda(\tau)}]$ we unitarily drive the system to its passive state by applying appropriate pulse sequence as shown in the 2nd part of Fig. 3.7(b)

$$\begin{aligned}\rho_{\lambda(\tau)} &= \eta(\tau)\mathbf{I} + \lambda(\tau)[\mathbf{I}/4 - (I_{1x}I_{2x} + I_{1y}I_{2y} + I_{1z}I_{2z})] \\ &\xrightarrow{\frac{1}{4\Delta\nu}} \eta(\tau)\mathbf{I} + \lambda(\tau)[\mathbf{I}/4 - (-I_{1x}I_{2y} + I_{1y}I_{2x} + I_{1z}I_{2z})] \\ &\xrightarrow{90_y^{(1,2)}} \eta(\tau)\mathbf{I} + \lambda(\tau)[\mathbf{I}/4 - (I_{1z}I_{2y} - I_{1y}I_{2z} + I_{1x}I_{2x})] \\ &\xrightarrow{\frac{1}{2J}} \eta(\tau)\mathbf{I} + \lambda(\tau)[\mathbf{I}/4 - (-I_{1x} + I_{2x} + 2I_{1x}I_{2x})/2] \\ &\xrightarrow{\frac{1}{2\Delta\nu}} \eta(\tau)\mathbf{I} + \lambda(\tau)[\mathbf{I}/4 - (I_{1y} + I_{2y} - 2I_{1y}I_{2y})/2] \\ &\xrightarrow{90_x^{(1,2)}} \eta(\tau)\mathbf{I} + \lambda(\tau)[\mathbf{I}/4 - (-I_{1z} - I_{2z} - 2I_{1z}I_{2z})/2] \\ &= \text{diag}(1 - 3\eta(\tau), \eta(\tau), \eta(\tau), \eta(\tau)) = \rho_{\lambda}^p(\tau), \end{aligned} \quad (3.55)$$

where $\eta(\tau) := (1 - \lambda(\tau))/4$, $90_{x/y}$ represents a $\pi/2$ rotation with rotation axis along x/y , $(1/2J)$ and $(1/4J)$ delays represent the free evolution under the scalar coupling, $(1/2\Delta\nu) \equiv 90_z^1 90_z^2$ and $(1/4\Delta\nu) \equiv 45_z^1 45_z^2$ represent the evolution under the chemical shift and PFG is the crusher gradient used in dephasing the coherence. For a finite storage time the system remains in the passive state having energy $E(\rho_\lambda^p(\tau)) = \text{Tr}(H_{AB}^{\text{int}} \rho_\lambda^p(\tau)) \simeq -\omega_H \lambda(\tau)$, where $H_{AB}^{\text{int}} \approx -\omega_H(I_{1z} + I_{2z})$, for $(J, \Delta\nu) \ll \omega_H$ and it can be estimated simply by measuring the diagonal elements of $\rho_\lambda^p(\tau)$ following the procedure shown in the last part of Fig. 3.7(b).

For singlet state, the marginal states are maximally mixed and no work can be extracted under a cyclic unitary operation. Therefore, using Eq. (3.6), we have $\Delta_{1|2} = \omega_H \lambda(\tau) - \omega_H/2$. Furthermore, since $m_1 = \omega_H$, $t_1 = t_2 = t_3 = (1 - \lambda(\tau))/4$, we therefore have $\delta_{1|2}^G = (\lambda(\tau) - 1)\omega_H/4$. In this case, the spectral independent bound turns out to be $\delta_{1|2}^I = 0$. In Fig. 3.7 (c) theoretically estimated (solid line) as well as experimentally estimated (circles) values of $\Delta_{1|2}$ are plotted against the purity factor $\lambda(\tau) = e^{-\tau/T_{LLS}}$. The vertical dashed and dotted-dashed lines correspond to $\delta_{1|2}^G$ and $\delta_{1|2}^I$, respectively. For the region where $\Delta_{1|2}$ exceeds those bounds the state is entangled.

3.4.3 Experiment II: Multi-qubit systems

Multi-qubit entangled states within NMR architecture can be prepared in star topology register (STR) [155]. STR involves a central qubit C (1st qubit) uniformly interacting with a set of $N - 1$ identical satellite qubits A (see Fig. 3.4(b)). Central qubit can be selectively addressed as it is realized by a different nuclear isotope. The ancillary qubits being indistinguishable can be addressed globally only. STR allows efficient preparation of entangled GHZ state [154]. The STR Hamiltonian along with the pulse sequence dynamics is described in Supplemental part.

We carry out experiments on the following two systems: (i) 3-qubit STR using FAN, wherein ^{19}F spin is the central qubit and two ^1H spins are the satellite qubits, with $J_{CA} = 45.5$ Hz; (ii) 10-qubit STR using TMP, wherein ^{31}P spin is the central qubit and nine ^1H spins are the satellite qubits, with $J_{CA} = 11.04$ Hz (see Fig. 3.4). After preparing the noisy state $\rho_\lambda[N] = (1 - \lambda)\mathbf{I}/2^N + \lambda|\psi_N\rangle\langle\psi_N|$, with $|\psi_N\rangle := (|0\rangle^{\otimes N} + |1\rangle^{\otimes N})/\sqrt{2}$, we test entanglement across C-vs-A bipartition considering $N = 3$ and 10 respectively for FAN and TMP. In doing that, we experimentally determine the thermodynamic quantity $\Delta_{1|1^c}$ along with global spectral dependent

separability bound $\delta_{1|1^c}^G$ and state independent bound $\delta_{1|1^c}^I$. Subsequently, we find out the ranges of λ for which $\Delta_{1|1^c}$ exceeds these bounds, and accordingly entanglement across C-vs-A gets certified.

The STR Hamiltonian is given by

$$H_{STR} = H_{STR}^{\text{int}} + H_{STR}^{RF}, \text{ where,} \quad (3.56a)$$

$$H_{STR}^{\text{int}} = -\omega_C I_{1z} - \omega_A \sum_{i=2}^N I_{iz} + 2\pi J I_{1z} \sum_{i=2}^N I_{iz}$$

$$H_{STR}^{RF} = \Omega_C(t) I_{1x} + \Omega_A(t) \sum_{i=2}^N I_{ix}. \quad (3.56b)$$

Here ω_C and ω_A are the Larmor frequencies of C and A spins respectively, J is the scalar coupling constant between C and A spins (see Fig. 3.4), and $\Omega_C(t)$, $\Omega_A(t)$ are the time-dependent RF drives on C and A respectively.

Preparation step

The initial thermal state of an STR is of the form

$$\rho_{th} = \frac{\mathbf{I}}{2^N} + \epsilon_A \left(\frac{\gamma_C}{\gamma_A} I_{1z} + \sum_{i=2}^N I_{iz} \right),$$

where $\epsilon_A = \gamma_A B_0 / (2^N k_B T)$. Starting from the thermal state a θ_y pulse on all the qubits followed by PFG results in the control over purity, i.e.,

$$\begin{aligned} \rho_{th} &\xrightarrow{\theta_y^{C,A}} \xrightarrow{\text{PFG}} \frac{\mathbf{I}}{2^N} + \epsilon_A \cos \theta \left(\frac{\gamma_C}{\gamma_A} I_{1z} + \sum_{i=2}^N I_{iz} \right) \\ &\rightarrow \frac{\mathbf{I}}{2^N} + \epsilon_A \cos \theta \sum_{i=2}^N I_{iz}, \end{aligned}$$

where we have ignored the first-qubit component, since it does not lead to the GHZ state (and gets filtered away by the subsequent PFG pulses). On further applying INEPT followed by CNOT, we

obtain

$$\rho_{Nq_h} = \sum_{q_h} r_{q_h} \left[(1 - \epsilon_A \cos \theta) \frac{\mathbf{I}}{2^N} + \epsilon_A \cos \theta \rho_{q_h} \right],$$

where $\sum_{q_h} r_{q_h} = 1$, with ρ_{q_h} describing a set of entangled states of coherence order $q_h = N - 2h$. Note that $q_h \in \{N, N - 2, \dots, -N + 2\}$ for $h \in \{0, 1, \dots, N - 1\}$. Using a pair of PFGs, we can filter out GHZ class ($q_h = N, h = 0$) by choosing lopsidedness

$$l_0 = 1 + (N - 1) \frac{\gamma_A}{\gamma_C} \quad (3.57)$$

[155, 156]. Invoking the paradigm of pseudopure states by setting $r_N = 1$ and $\epsilon_A = 1$, we obtain

$$\rho_N(\lambda(\theta)) = (1 - \lambda(\theta)) \frac{\mathbf{I}}{2^N} + \lambda(\theta) |\psi_N\rangle \langle \psi_N|, \quad \text{where } |\psi_N\rangle := \frac{1}{\sqrt{2}} (|0\rangle_C |0\rangle_A^{\otimes(N-1)} + |1\rangle_C |1\rangle_A^{\otimes(N-1)}) \quad (3.58)$$

is the N -qubit GHZ state with purity control $\lambda(\theta) = \cos \theta$. This completes the preparation protocol of GHZ class of states.

Entanglement certification step

The entanglement certification step involves transforming GHZ class of states to their corresponding passive states. This is accomplished by another CNOT gate followed by a 90_y pulse (which cancels with a subsequent readout pulse) as depicted in Fig. 3.8. A pair of PFG pulses of relative ratio $-l_0$ is used to filter the GHZ state for which the passive state reads as

$$\rho_N^p(\lambda(\theta)) = [1 - \lambda(\theta)] \frac{\mathbf{I}}{2^N} + \lambda(\theta) |0\rangle \langle 0|_C \otimes |0\rangle \langle 0|_A^{\otimes(N-1)}.$$

We have carried out the experiments on two systems as shown in Fig. 3.4. This final spectrum corresponding to the GHZ class contains a single transition at frequency $-J(N - 1)/2$ [155]. Comparing the final intensity with that corresponding to $\theta = 0$ we have a direct estimation of the purity factor $\lambda(\theta)$.

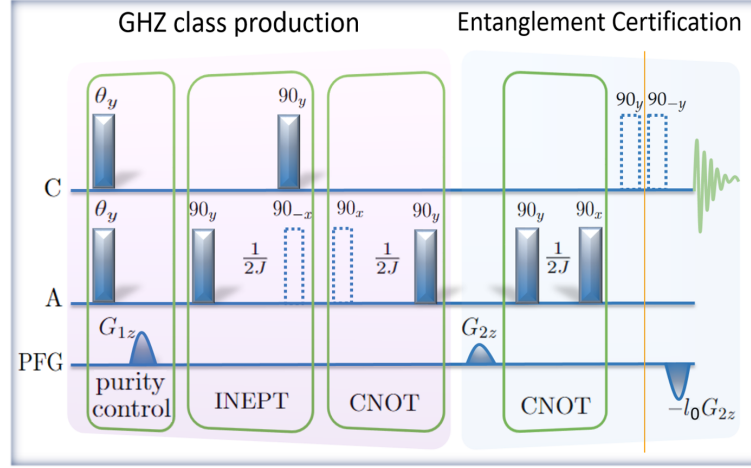


Figure 3.8: The NMR pulse sequence to prepare GHZ class states with controlled purity on an STR and then certify the presence or absence of entanglement. The vertical line shows the instant when the passive state is created. The dashed pulses cancel each other.

3.4.3.1 Three-qubit system

We have used FAN (fluoroacetonitril; Fig. 3.4 (d)), wherein ^{19}F spin is the central qubit and two ^1H spins are the satellite qubits. Here $J_{FH} = 11.04$ Hz. Now following Eq. (3.56a) and Eq.(3.58) we have our Hamiltonian and initial global state as $H_{STR}^{\text{int}} \approx -\omega_F I_{1z} - \omega_H \sum_{i=2}^3 I_{iz}$ as $J \ll (\omega_H, \omega_F)$ and $\rho_{N=3}(\lambda(\theta))$. Furthermore, using Eq.(3.4) we have

$$\begin{aligned}
 \Delta_{1|23} &= W(\rho_{N=3}(\lambda(\theta))) - W(\rho_1) - E(\rho_{23}) + E_g^{23} \\
 &= [E(\rho_{N=3}(\lambda(\theta))) - E(\rho_{N=3}^p(\lambda(\theta)))] - [E(\rho_1) - E(\rho_1^p)] - E(\rho_{23}) + E_g^{23} \\
 &= -E(\rho_{N=3}^p(\lambda(\theta))) + E_g^{23} \\
 &= \lambda(\theta)(\omega_F + 2\omega_H)/2 - \omega_H,
 \end{aligned} \tag{3.59}$$

where $E(\rho_{N=3}^p(\lambda(\theta))) = \text{tr}(H_{STR}^{\text{int}} \rho_{N=3}^p(\lambda(\theta))) = -\lambda(\theta)(\omega_F + 2\omega_H)/2$, $E_g^{23} = -\omega_H$ is the ground state energy of the second and third qubit and $E(\rho_1^p) = 0$. Now following Eq.(3.22) and using values $\alpha_1 = \omega_P$, $\alpha = \omega_H$ and $t_1 = \dots = t_7 = (1 - \lambda(\theta))/8$ we have

$$\delta_{1|23}^G = (\lambda(\theta) - 1)(\omega_H - 3\omega_F/8) \tag{3.60}$$

and following Eq.(3.23) we have spectral independent bound as $\delta_{1|23}^I = 0$. Fig. 3.9(b) in the manuscript shows both $\delta_{1|23}^G$ and $\delta_{1|23}^I$ marking $\Delta_{1|23}$ at $\lambda = 3/7$ and $\lambda = 0.68$ and for any value

of λ above them the state $\rho_{N=3}(\lambda(\theta))$ is said to be entangled.

3.4.3.2 Ten-qubit system

We have used TMP (trimethyl-phosphate; Fig. 3.4 (c)), wherein ^{31}P spin is the central qubit and nine ^1H spins are the satellite qubits. Here $J_{PH} = 11.04$ Hz. Following Eq. (3.56a) and Eq.(3.58) we have our Hamiltonian and initial global state as $H_{STR}^{\text{int}} \approx -\omega_P I_{1z} - \omega_H \sum_{i=2}^{10} I_{iz}$ as $J \ll (\omega_H, \omega_P)$ and $\rho_{N=10}(\lambda(\theta))$ for GHZ class we have

$$\begin{aligned} \Delta_{1|1^c} &= W(\rho_{N=10}(\lambda(\theta))) - W(\rho_1) - E(\rho_{1^c}) + E_g^{1^c} \\ &= [E(\rho_{N=10}(\lambda(\theta))) - E(\rho_{N=10}^p(\lambda(\theta)))] - [E(\rho_1) - E(\rho_1^p)] - E(\rho_{1^c}) + E_g^{1^c} \\ &= -E(\rho_{N=10}^p(\lambda(\theta))) + E_g^{1^c} \\ &= \lambda(\theta)(\omega_P + 9\omega_H)/2 - 9\omega_H/2, \end{aligned} \quad (3.61)$$

where $E(\rho_{N=10}^p(\lambda(\theta))) = \text{tr}(H_{STR}^{\text{int}} \rho_{N=10}^p(\lambda(\theta))) = -\lambda(\theta)(\omega_P + 9\omega_H)/2$, $E_g^{1^c} = -9\omega_H/2$ is the ground state energy of rest of the 9 qubits and $E(\rho_1^p) = 0$. Now following Eq.(3.35) and using values $\alpha_1 = \omega_P$, $\alpha = \omega_H$ and $t_1 = t_2 = \dots = t_{2^{10}-1} = (1 - \lambda(\theta))/2^{10}$ we have

$$\delta_{1|1^c}^G = (\lambda(\theta) - 1)(9\omega_H/2 - (2^9 - 1)\omega_P/2^{10}) \quad (3.62)$$

and following Eq.(3.36) we have spectral independent bound as $\delta_{1|1^c}^I = 0$. Fig. 3.9(d) shows both $\delta_{1|1^c}^G$ and $\delta_{1|1^c}^I$ marking $\Delta_{1|1^c}$ at $\lambda = 0.499$ and $\lambda = 0.957$ and if any value of λ is above the marked values then $\rho_{N=10}(\lambda(\theta))$ is entangled.

3.4.4 Experiment III: Global vs Global-Local Separability bounds

In this experiment we aim to compare the efficacy of entanglement certification of three-qubit noisy GHZ state through Global-Local and Global separability bounds as stated in Theorem 1. In our earlier experiments when we were evaluation $\Delta_{X|X^c}$, we considered the X part consisting only one subsystem. Accordingly the Global-Local separability bound and Global separability bound become identical. In this case we consider a three-qubit system with X consisting of two qubits. In experiment we use Di-Bromo Fuloromethane (DBFM) [see Fig. 3.5(e)] as the three-

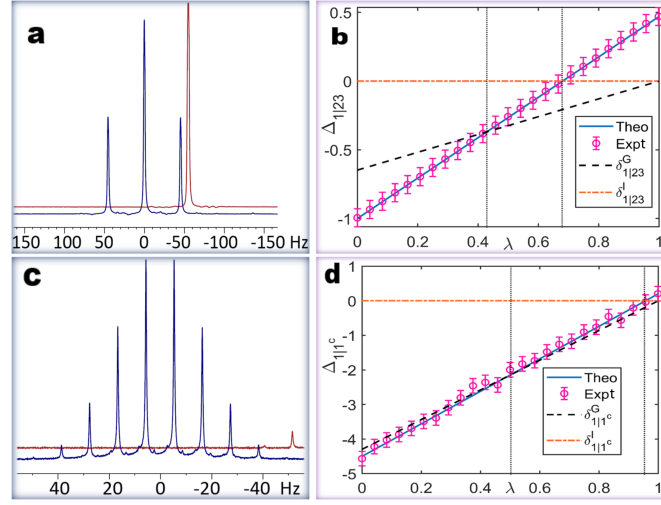


Figure 3.9: (Color Online) (a) ^{19}F spectra of FAN corresponding to one-pulse experiment on thermal state (front) and to the three-qubit GHZ state (back). (b) Plot $\Delta_{1|23}$ (in the unit of ω_H) vs purity λ for 3-qubit noisy GHZ states. Comparing the values of $\Delta_{1|23}$ and $\delta_{1|23}^G$, $\delta_{1|23}^I$, we identify the threshold values marked by the dotted lines: $\lambda = 3/7$ and $\lambda = 0.68$, respectively. Above these thresholds, the state exhibits entanglement. (c) ^{31}P spectra of TMP corresponding to one pulse experiment (front), and to GHZ (back). (d) $\Delta_{1|1^c}$ vs purity λ for the 10-qubit GHZ class. Here $\lambda = 0.499$ and $\lambda = 0.957$ for $\delta_{1|1^c}^G$ and $\delta_{1|1^c}^I$ marks the entanglement threshold boundary. The errorbar represents the estimated random error due to noise.

qubit system. The Hamiltonian of the system can be written in terms of the internal part and the RF drive as

$$H_{123} = H_{123}^{\text{int}} + H_{123}^{\text{RF}}, \quad \text{where} \quad (3.63a)$$

$$H_{123}^{\text{int}} = -\omega_H I_{1z} - \omega_C I_{2z} - \omega_F I_{3z} + 2\pi J_{HC} I_{1z} I_{2z} + 2\pi J_{CF} I_{2z} I_{3z} + 2\pi J_{HF} I_{1z} I_{3z} \\ H_{123}^{\text{RF}} = \Omega_H(t) I_{1x} + \Omega_C(t) I_{2x} + \Omega_F(t) I_{3x}, \quad (3.63b)$$

$$H_{12}^{\text{int}} = -\omega_H I_{1z} - \omega_C I_{2z} + 2\pi J_{HC} I_{1z} I_{2z}, \quad \text{where } X \equiv 12. \quad (3.63c)$$

Here, H , C , & F correspond to first, second, and third system respectively.

Preparation step

We start with the initial thermal state

$$\sigma_{123}^{th} = \frac{1}{8} \mathbf{I} + \epsilon_H \left(I_{2z} + \frac{\gamma_C}{\gamma_H} I_{2z} + \frac{\gamma_F}{\gamma_H} I_{3z} \right), \quad \text{where } \epsilon_H = \gamma_H B_0 / 4k_B T. \quad (3.64)$$

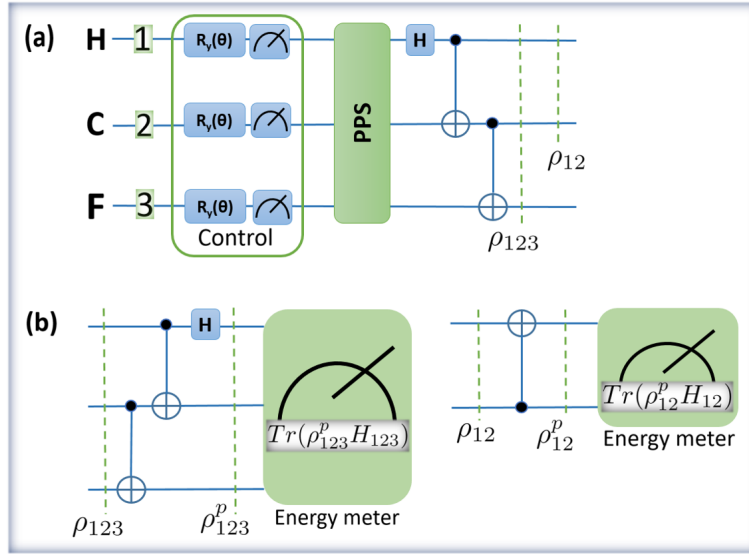


Figure 3.10: (a) Quantum circuit to prepare 3-qubit GHZ state ρ_{123} with control θ , here PPS stands for pulse sequence to prepare pseudo-pure state from thermal equilibrium. (b) Quantum circuit for global and local passive state conversion and to measure their corresponding energies.

After application of the control sequence as shown in Fig. 3.10(a) and the PPS pulse sequence [173], we obtain the state

$$\sigma_{123}^\epsilon(\lambda) = \frac{1 - \epsilon\lambda}{8} \mathbf{I} + \epsilon\lambda |000\rangle\langle 000|, \quad (3.65)$$

where $\lambda = \cos \theta$. Within the PPS paradigm taking $\epsilon = 1$ we have

$$\sigma_{123}(\lambda) = \frac{1 - \lambda}{8} \mathbf{I} + \lambda |000\rangle\langle 000|. \quad (3.66)$$

Now, consecutively applying Hadamard on H , CNOT with H being the control and C being the target, and CNOT (C control and F target) [Fig. 3.10(a)], we prepare the noisy GHZ state

$$\rho_{123}(\lambda) = \frac{1 - \lambda}{8} \mathbf{I} + \lambda |\psi\rangle_{GHZ} \langle \psi|, \quad (3.67)$$

where $|\psi\rangle_{GHZ} := (|000\rangle + |111\rangle)/\sqrt{2}$.

Entanglement certification step

To evaluate the quantity $\Delta_{12|3}$ we will first evaluate $W(\rho_{123}(\lambda))$. For that we unitarily evolve $\rho_{123}(\lambda)$ to the corresponding lowest energy state. While for a generic state the optimization over

the unitary is a tedious task, however for this class of state it can be achieved by applying a single unitary operation [see Fig. 3.10(b)]. The resulting state reads as

$$\rho_{123}^p(\lambda) = \frac{1-\lambda}{8}\mathbf{I} + \lambda|000\rangle\langle 000|, \quad (3.68)$$

which in turn will yield $W(\rho_{123}(\lambda)) = E(\rho_{123}(\lambda)) - E(\rho_{123}^p(\lambda))$. To evaluate $W_{[12]}(\rho_{12})$ we evolve the subsystem 12 to the corresponding lowest energy state ρ_{12}^p [see Fig. 3.10(c)]. We have

$$\rho_{12} = \frac{1+\lambda}{4}|00\rangle\langle 00| + \frac{1-\lambda}{4}|01\rangle\langle 10| + \frac{1-\lambda}{4}|10\rangle\langle 01| + \frac{1+\lambda}{4}|11\rangle\langle 11|, \quad (3.69a)$$

$$\rho_{12}^p = \frac{1+\lambda}{4}|00\rangle\langle 00| + \frac{1+\lambda}{4}|01\rangle\langle 01| + \frac{1-\lambda}{4}|10\rangle\langle 10| + \frac{1-\lambda}{4}|11\rangle\langle 11|, \quad (3.69b)$$

where $\rho_{12} = \text{Tr}_3[\rho_{123}]$. Since the system Hamiltonian is known we can eventually calculate energy of the third subsystem $E(\rho_3)$, its ground state energy E_g^3 , and obtain $\Delta_{12|3}^{Exp}$ experimentally. We can also calculate this quantity theoretically. For the system in consideration with $(J_{HC}, J_{CF}, J_{HF}) \ll (\omega_H, \omega_C, \omega_F)$ we have

$$\left\{ \begin{array}{l} x_0 = \frac{1+\lambda}{4}, \quad x_1 = \frac{1+\lambda}{4}, \quad x_2 = \frac{1-\lambda}{4}, \quad x_3 = \frac{1-\lambda}{4}, \quad t_0 = \frac{1+7\lambda}{8}, \\ \{t_1, \dots, t_7\} = \frac{1-\lambda}{8}, \quad m_0 = 0, \quad m_1 = \omega_C, \quad m_2 = \omega_H, \quad m_3 = (\omega_H + \omega_C), \\ n_0 = 0, \quad n_1 = \omega_C, \quad n_2 = \omega_F, \quad n_3 = \omega_H, \quad n_4 = (\omega_C + \omega_F), \\ n_5 = (\omega_C + \omega_H), \quad n_6 = (\omega_F + \omega_H), \quad n_7 = (\omega_C + \omega_F + \omega_H), \\ \omega_H = 500\text{MHz}, \quad \omega_C = 125.721\text{MHz}, \quad \omega_F = 470.385\text{MHz} \end{array} \right\}. \quad (3.70)$$

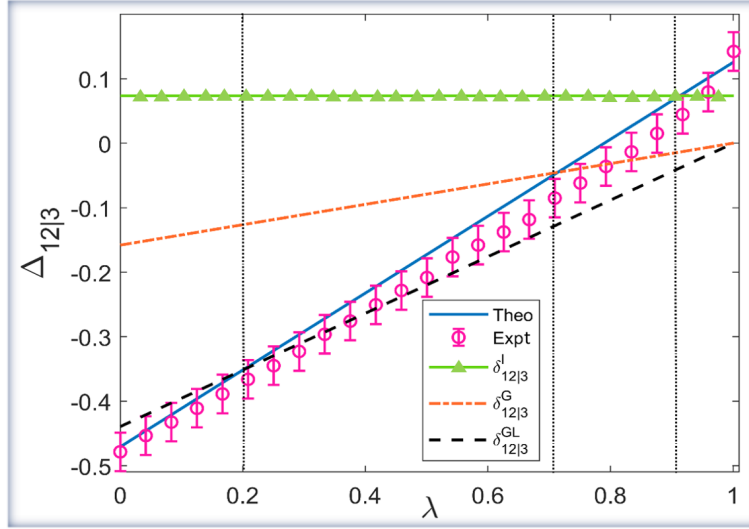


Figure 3.11: (Color Online) Plot of $\Delta_{12|3}$ (experimental as well as theoretical), $\delta_{12|3}^{GL}$, $\delta_{12|3}^G$, and $\delta_{12|3}^I$ against the noise parameter λ . The state independent, the global, and the global-local separability conditions certify entanglement for the parameter ranges $\lambda > 0.91$, $\lambda > 0.71$, and $\lambda > 1/5$ respectively, establishing hierarchy among these conditions.

These yield us

$$\Delta_{12|3} = \sum_{j=1}^3 m_j x_j - \sum_{j=1}^7 n_j t_j = (\omega_C + \omega_F)\lambda/2 - \omega_F/2, \quad (3.71a)$$

$$\delta_{12|3}^{GL} = \sum_{j=1}^3 (m_j - m_1) x_j + \sum_{j=1}^7 (m_1 - n_j) t_j = (4\omega_F - \omega_C)\lambda/8 + (\omega_C - 4\omega_F)/8, \quad (3.71b)$$

$$\delta_{12|3}^G = \sum_{j=1}^2 (m_j - n_j) t_j + \sum_{j=3}^7 (m_3 - n_j) t_j = (\omega_H + \omega_C - 2\omega_F)(1 - \lambda)/4, \quad (3.71c)$$

$$\delta_{12|3}^I = (2\omega_H - 2\omega_F + \omega_C)/5 = 0.0743\omega_H. \quad (3.71d)$$

In Fig. 3.11 we plot $\Delta_{12|3}$ (experimental as well as theoretical), $\delta_{12|3}^{GL}$, $\delta_{12|3}^G$, and $\delta_{12|3}^I$ against the noise parameter λ .

3.5 Conclusions and outlook

Manipulating entanglement efficiently in multipartite system is essential for emerging quantum technologies that involve distributed quantum information protocols. Continuous research effort is going on to this aim with different quantum architectures [21, 174–177]. Certifying entangle-

ment is a crucial step for successful implementation of many quantum protocols. Along with device independent certification scheme through Bell tests [178–183], there exists device dependent witness based method of entanglement certification [184, 185]. However, implementing those methods are quite challenging in practice when the quantum systems are composed of many subsystems.

In that respect our proposed thermodynamic criteria are less demanding. It provides a way to certify entanglement by measuring global and local ergotropic works. We experimentally validate the proposed thermodynamic entanglement criterion in NMR architecture by considering particular classes of 2-qubit, 3-qubit, and 10-qubit noisy entangled states. In comparison with [186] that relies on full density state tomography of pure states and [187] that is limited to bipartite system, our method achieves certification for multi-qubit mixed states with three different bounds based on the thermodynamic quantifiers of the system. Our thermodynamic approach opens up an easy avenue to certify entanglement even when the knowledge about the state in question is not available. While we have invoked the pseudopure paradigm for our ensemble architecture, similar protocols can be easily setup for other architectures with access to different degrees of state purity. For instance, entanglement enhanced quantum sensing by optical probes [128] or NV centers [188] may be benefited from prior certification of entanglement. At this point, we would like to point out that study of ergotropy is constantly advancing with different quantum architectures, such as optical mode [189] and bosonic Gaussian models [190, 191]. It will be therefore interesting to test entanglement in those physical systems using our proposed criteria. The recent work of [192] wherein coarse-grained measurement scheme is proposed is worth-mentioning at this point. Our study welcomes a number of other questions for future research. For instance, generalizing our criteria for systems with arbitrary local dimensions and generalizing to capture more exotic kinds of entanglement, such as genuine multi-partite entanglement, would be quite important. While the local passivity in our case is studied under local unitary operations, more general notion of strong local passivity is introduced by considering more general local quantum operation [49, 193, 194]. Obtaining entanglement certification criteria under this generic consideration could also be quite interesting.

CHAPTER 4

Maximal work extraction from nuclear spins using FQErgo

Abstract

Considering the emerging applications of quantum technologies, studying energy storage and usage at the quantum level is of great interest. In this context, there is a significant contemporary interest in studying *ergotropy*, the maximum amount of work that can be extracted unitarily from an energy-storing quantum device. Here, we propose and experimentally demonstrate a feedback-based algorithm (FQErgo) for estimating ergotropy. This method also transforms an arbitrary initial state to its passive state, which allows no further unitary work extraction. FQErgo applies drive fields whose strengths are iteratively adjusted via certain expectation values, conveniently read using a single probe qubit. Thus, FQErgo provides a practical way for unitary energy extraction and for preparing passive states. By numerically analyzing FQErgo on random initial states, we confirm the successful preparation of passive states and estimation of ergotropy, even in the presence of drive errors. Finally, we implement FQErgo on two- and three-qubit NMR registers, prepare their passive states, and accurately estimate their ergotropy. **Reported in**

Jitendra Joshi and T. S. Mahesh, *Maximal work extraction unitarily from an unknown quantum state: Ergotropy estimation via feedback experiments*, [arXiv:2409.04087](https://arxiv.org/abs/2409.04087) (2024).

4.1 Introduction

In second chapter we studied how to charge a nuclear spin quantum battery, in this chapter, we will aim to extract work from a set of charged nuclear spins initially existing in their unknown quantum state. Quantum technologies are appealing as they can surpass their classical counterparts by using exclusive concepts like coherence and entanglement. Understanding their capa-

bilities has progressed in recent years, thanks to the numerous experimental breakthroughs that have improved control over quantum states. Specifically, the investigation of the principles of quantum thermodynamics is made possible by quantum thermal machines, which include refrigerators and heat engines to regulate heat flow and work production [195, 196]. Further options for storing energy for later extraction include quantum batteries [48, 72, 74, 78, 95, 197–202]. The quantum batteries have the potential to outperform their classical counterparts in relevant metrics like charging speed [77, 93, 169, 203–206], stored energy [71, 101, 169], and energy extraction [76, 83, 92, 207–210]. The maximum amount of energy that can be extracted from quantum systems through unitary processes is known as *the ergotropy* [42]. A practical way to determine ergotropy is by finding the optimal unitary operation that transforms the system to its lowest attainable energy state, known as its *passive state* [43]. This can be a challenging undertaking as ergotropy might be sensitive to correlations that can also impact device performance [211–218]. Recent works have tried to establish a link between entanglement and thermodynamic quantities like the ergotropy gap, the difference between the maximal extractable works via global and local unitaries. These thermodynamic quantities can be used to verify entanglement present in bipartite [219], multipartite [220, 221], and multiqubit mixed states [222]. Using these quantities, experimental certification of entanglement has been demonstrated in up to 10 qubits [222].

The main focus of this work is FQErgo, an algorithm we propose for preparing the passive state and thereby estimating ergotropy. FQErgo is inspired by (hence the name) the feedback-based algorithm for quantum optimization (FALQON) [223], which has been recently developed for combinatorial quantum optimization. This method is related to quantum Lyapunov control (QLC) and uses feedback conditioned on qubit measurements at each quantum circuit layer and parametrized quantum circuits to determine the values of the circuit parameters at subsequent layers [224, 225].

We note several salient features of the FQErgo algorithm. Firstly, the all-quantum nature of the algorithm: unlike the previous methods [226, 227] for estimating ergotropy, FQErgo requires no classical optimizer, and can be fully automated for convenient practical realizations. Secondly, FQErgo is robust against circuit errors since each feedback iteration readjusts the drives based on previous errors. This way, cumulative error growth is prevented. Thirdly, the circuit parameters can be read efficiently via an ancillary probe qubit using the interferometric method [228–230],

which alleviates the need for resource-intensive quantum state tomography. In this work, after numerically analyzing the FQErgo algorithm, we experimentally demonstrate it using two and three-qubit NMR registers.

4.1.1 Objectives

In this work, we carry out NMR investigation of Work extraction from a nuclear spin system whose initial state is unknown.

- (i) We propose a feedback based method FQErgo for work extraction.
- (ii) We numerically simulate FQErgo on one and two qubit system.
- (iii) We experimentally verify FQErgo using two and three qubit NMR registers.

4.2 Theory

4.2.1 Unitary extraction of work, passive state, and ergotropy

Given a quantum system in a state ρ_0 , the *ergotropy* quantifies the maximum amount of work that is unitarily extracted while leaving the system into a passive state ρ^p from which no further work can be unitarily extracted [42]. If H_0 is the system Hamiltonian, the ergotropy is given by

$$\begin{aligned}\mathcal{E}(\rho_0) &= E(\rho_0) - E(\rho^p), \text{ where,} \\ E(\rho^p) &= \min_U \text{Tr} (U \rho_0 U^\dagger H_0) .\end{aligned}\tag{4.1}$$

Let \mathcal{U}_p corresponds to the unitary that minimizes the system energy such that $\rho^p = \mathcal{U}_p \rho_0 \mathcal{U}_p^\dagger$ is the passive state [42, 43]. If H_0 and ρ_0 , in their respective eigenbases, are in the form

$$\begin{aligned}H_0 &= \sum_k E_k |E_k\rangle\langle E_k|, \text{ with } E_1 \leq E_2 \leq \dots \text{ and} \\ \rho_0 &= \sum_j r_j |r_j\rangle\langle r_j|, \text{ with } r_1 \geq r_2 \geq \dots ,\end{aligned}\tag{4.2}$$

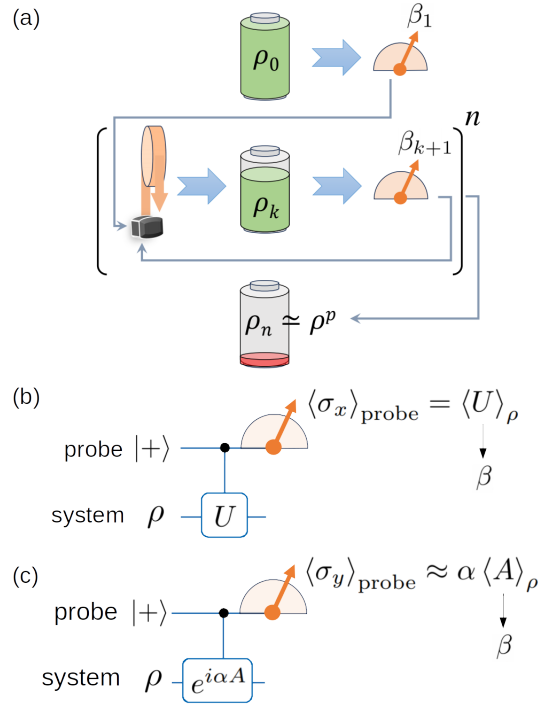


Figure 4.1: (a) Illustrating n iterations of FQErgo applied on an initial state ρ_0 to reach $\rho_n \approx \rho^p$, its passive state. (b,c) Determining FQErgo drive amplitude β with a probe qubit, for (b) unitary Hermitian drive σ_γ , and (c) nonunitary Hermitian drive A . For energy measurement, we set $A = H_0$.

then the passive state is uniquely defined in the energy eigenbasis as

$$\rho^p = \sum_j r_j |E_j\rangle \langle E_j|. \quad (4.3)$$

While the above definitions of the passive state and ergotropy are simple and clear, the experimental realization of the passive state from an unknown initial state and thereby estimating its ergotropy has not been reported. In the following, we describe a robust method for the same.

4.2.2 FQErgo: A feedback algorithm for ergotropy estimation

FQErgo is based on the FALQON algorithm proposed recently [223]. We assume multiple copies of individually accessible systems each prepared in the state ρ_0 , which is not necessarily known. Alternatively, we can assume an oracle that transforms a uniquely initialized quantum system into

a definite unknown state ρ_0 . On introducing a drive Hamiltonian $\beta(t)H_d$, the system evolves as

$$i\frac{d}{dt}\rho(t) = [H_0 + \beta(t)H_d, \rho(t)], \quad (4.4)$$

where $\beta(t)$ is the time-dependent drive parameter. Here and in the rest of the paper we have set $\hbar = 1$. We seek to minimize the system energy $E(\rho(t)) = \langle H_0 \rangle \rho(t) = \text{Tr}(H_0 \rho(t))$, which can be accomplished by designing control $\beta(t)$ satisfying the Lyapunov condition

$$\frac{d}{dt}\langle H_0 \rangle \rho(t) = \beta(t) \langle C_d \rangle \rho(t) \leq 0, \quad \forall t \geq 0 \quad (4.5)$$

where $C_d = i[H_d, H_0]$. One way to satisfy the above is by choosing the control in the form [223]

$$\beta(t) = -w \langle C_d \rangle \rho(t), \quad (4.6)$$

where w is a positive scalar coefficient.

The overall algorithm is illustrated in Fig. 4.1 (a). We apply discrete drives each of duration τ and realize a n -step feedback loop,

$$U_n = u_n \cdots u_2 u_1, \quad \text{with } u_k = e^{-i\beta_k \tau H_d}. \quad (4.7)$$

We find the first drive parameter by measuring the expectation value $\beta_1 = -w \langle C_d \rangle \rho_0$, and prepare the state $\rho_1 = U_1 \rho_0 U_1^\dagger$. The subsequent steps involve finding

$$\beta_k = -w \langle C_d \rangle \rho_{k-1} \text{ and preparing } \rho_k = U_k \rho_0 U_k^\dagger. \quad (4.8)$$

Thus, starting from an unknown quantum state ρ_0 , using the sequence of feedback-designed operators $U_n \approx \mathcal{U}_p$, we attain the minimum saturated energy state $\rho_n \approx \rho^p$. The energy measurements of the system for the initial state ρ_0 and the final state $\rho_n \sim \rho_p$ yield an estimation of ergotropy via Eq. 4.1.

4.2.3 FQErgo using a probe qubit

FQErgo described above needs an efficient method to repeatedly extract expectation values of the commutator in Eq. 4.6, and to monitor the system-energy. Since quantum state tomography is prohibitively expensive and unnecessary for such a task, we shall use the interferometric circuit with an ancillary probe qubit [226–228]. The interferometric circuit for measuring the energy $E(\rho_k)$ as well as extracting the drive parameter β_k in Eq. 4.8 are shown in Fig. 4.1 (b,c). The circuit involves preparing the probe qubit in the $|+\rangle$ state, the system in any state ρ , applying a certain controlled operation on the system, and finally measuring the probe qubit. First, consider extracting the expectation value $\langle U \rangle_\rho$ of a unitary Hermitian observable U . In this case, we implement a controlled U gate as shown in Fig. 4.1 (b). The probe signal is then given by [229],

$$\langle \sigma_x \rangle_{\text{probe}} = \langle U \rangle_\rho. \quad (4.9)$$

Thus, we directly obtain the desired expectation value of the system as the signal $\langle \sigma_x \rangle_{\text{probe}}$ in the probe qubit. For example, if the system Hamiltonian is the Pauli operator σ_z as described later in the experimental section, the probe signal directly yields the expectation value $\langle \sigma_z \rangle_\rho$. For the more general case of extracting the expectation value $\langle U \rangle_\rho$ of a nonunitary Hermitian observable A , we construct a unitary $e^{-i\alpha A}$, where α is a real parameter such that $||\alpha A|| \ll 1$. Now implementing the controlled gate as shown in Fig. 4.1 (c), we obtain the probe signal [229]

$$\langle \sigma_y \rangle_{\text{probe}} = -\langle \sin(A\alpha) \rangle_\rho \approx -\alpha \langle A \rangle_\rho. \quad (4.10)$$

Here, by setting $A = C_d$, we can extract $\langle C_d \rangle_\rho$ directly as the probe signal $\langle \sigma_y \rangle_{\text{probe}}$.

4.3 Numerical simulations

4.3.1 Single qubit system

We consider a single qubit system with Hamiltonian $H_0 = \omega_0(\mathbf{I} - \sigma_z)/2$ with energy eigenvalues $(0, \omega_0)$ prepared in an arbitrary mixed state $\rho(0) = (1 - \epsilon)/2\mathbf{I} + \epsilon|\psi\rangle\langle\psi|$, where $|\psi\rangle = \cos(\theta/2)|0\rangle + e^{i\phi}\sin(\theta/2)|1\rangle$ and the purity parameter $\epsilon \in [0, 1]$. We now use FQErgo to reach

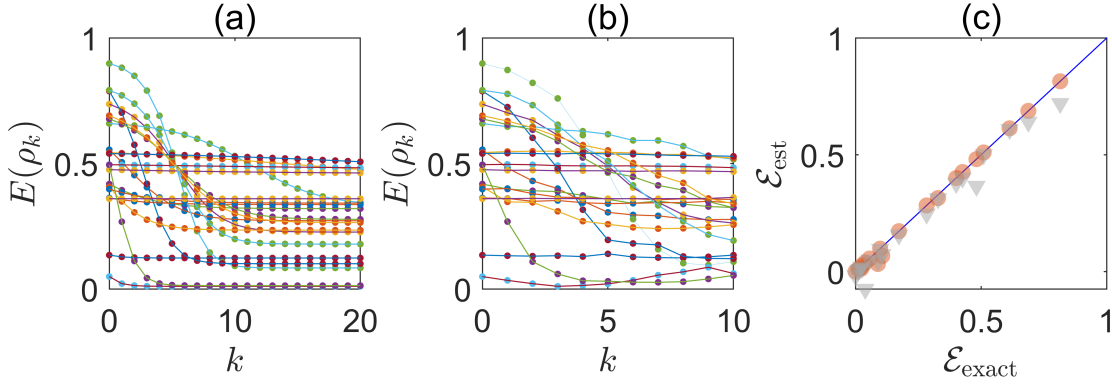


Figure 4.2: (a,b) Simulated system-energy $E(\rho_k)$ vs iteration number k for a single qubit ($\omega_0 = 1$) starting from 20 random initial states applied with (a) ideal FQErgo and (b) FQErgo having random errors. Insets show the first three iterations. (c) Numerically estimated vs exact ergotropy values with ideal FQErgo (filled circles) and FQErgo with random errors (filled triangles).

its passive state $\rho^p = (1 - \epsilon)\mathbb{I}/2 + \epsilon|0\rangle\langle 0|$. For the one qubit case, FQErgo needs only two drives: σ_x and σ_y . Fig. 4.2 (a) shows the energy $E(\rho_k)$ versus iteration number k for a set of 20 random initial states. In all cases, we see monotonically decreasing energy, ultimately approaching their respective passive states for sufficiently large iterations n , i.e., $\rho_n \rightarrow \rho^p$. The difference between the initial energy $E(\rho_0)$ and the final energy $E(\rho_n)$ estimates the ergotropy, i.e., $\mathcal{E}_{\text{est}}(\rho_0) = E(\rho_0) - E(\rho_n)$. The filled circles in Fig. 4.2 (c), plotting $\mathcal{E}_{\text{est}}(\rho_0)$ vs $\mathcal{E}_{\text{exact}}(\rho_0) = E(\rho_0) - E(\rho^p)$ confirm perfect estimation of ergotropy for all the random initial states.

Now we numerically analyze the robustness of FQErgo against potential imperfections in practical implementations. Firstly, being a feedback-based method, FQErgo is naturally robust against the drive amplitude. If the drive amplitude is lesser than the nominal, it still reaches the passive state but simply takes more iterations. To study the effect of more general errors, we introduce an error rotation of 5 degrees about a random direction in every FQErgo iteration. The system-energy curves in Fig. 4.2 (b) no longer exhibit a perfect monotonic decay, but neither show serious build-up of errors. The corresponding ergotropy values shown by filled triangles in Fig. 4.2 (c) show somewhat underestimated values, which is expected since circuit errors can only make the system settle in a higher energy state by preventing it from reaching the passive state.

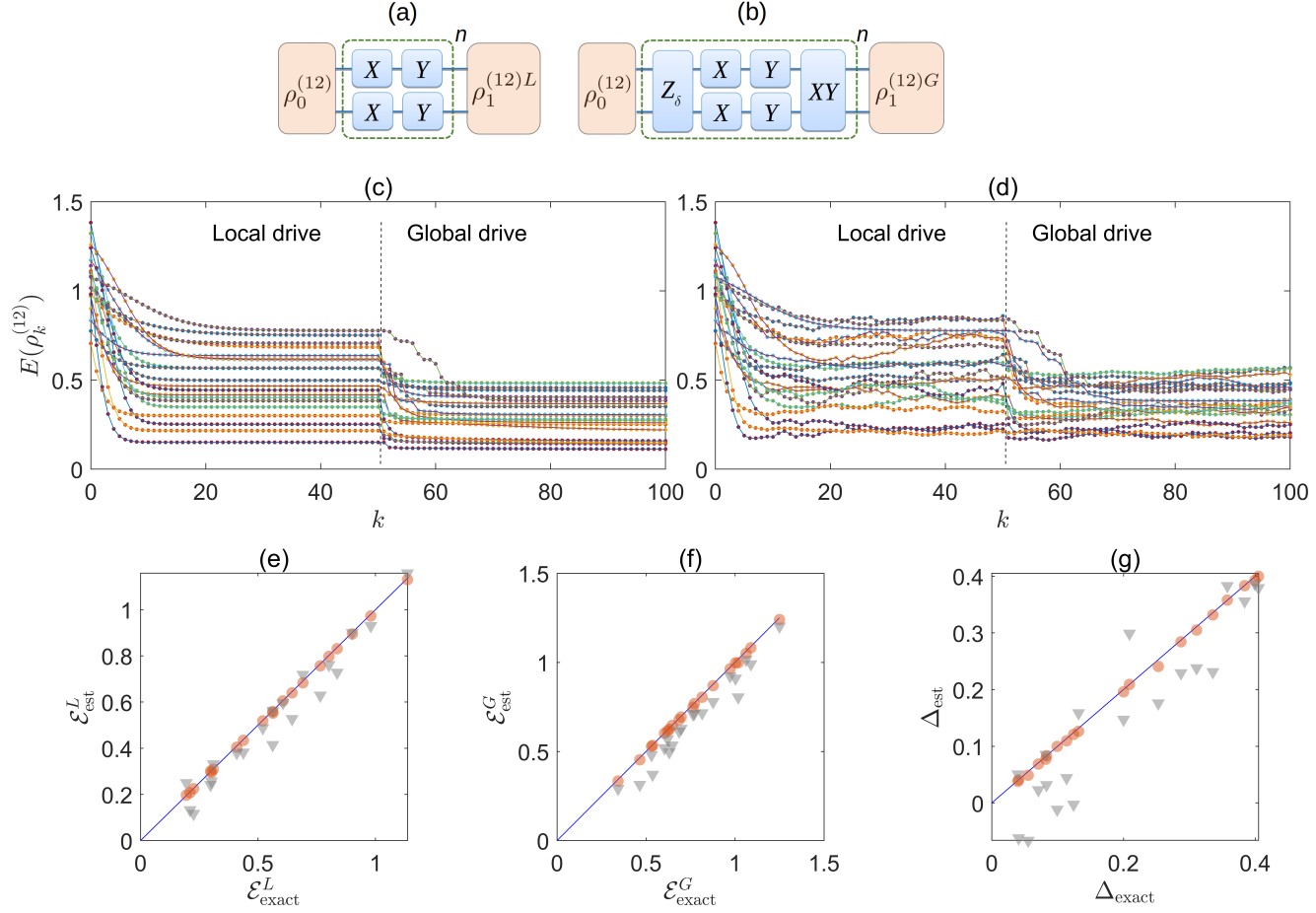


Figure 4.3: (a,b) FQErgo circuits for local (a) and global (b) energy extraction in two-qubits. Here, local drives X , Y suffice for reaching the local passive state $\rho^{(12)L}$ and estimating the local ergotropy $\mathcal{E}^L(\rho_0^{(12)})$ (a). In contrast, additional global drive such as XY and Z_δ [226] gates are necessary for reaching the global passive state $\rho^{(12)G}$ and estimating the global ergotropy $\mathcal{E}^G(\rho_0^{(12)})$ (b). (c,d) Simulated system-energy vs iteration number for the two-qubit ($\omega_0 = 1$ and $J = 0.01$) FQErgo from 20 random initial states without error (c) and with error (d). (e,f) The numerically estimated local (e) and global ergotropy (f) vs the exact values. (g) Ergotropy gap obtained from (e) and (f), vs the exact values. In (e-g), the filled circles are without random errors and filled triangles are with random errors.

4.3.2 Two qubit system

There is a fundamental distinction between work extraction in single-qubit and two-qubit systems. For two-qubit system ρ_{12} , energy can be extracted through either local unitaries $U_L = U_1 \otimes U_2$ or global unitaries $U_G = U_{12}$ applied to the entire system. For application of local unitaries, the system reaches the local passive state ρ^{pL} , giving local ergotropy $\mathcal{E}^L = E(\rho_0) - E(\rho^{pL})$. On the other hand, if global unitaries are applied, the system evolves to the global passive state ρ^{pG} , determining the global ergotropy, $\mathcal{E}^G = E(\rho_0) - E(\rho^{pG})$. The difference, $\Delta = \mathcal{E}^G - \mathcal{E}^L$, is referred to as the ergotropy gap which is always greater or equal to zero as $U_L \subseteq U_G$ [231].

Consider a two-qubit system with Hamiltonian $H_0 = \omega_0(\mathbf{I} \otimes \mathbf{I} - (\sigma_z \otimes \mathbf{I} + \mathbf{I} \otimes \sigma_z)/2) + J(\sigma_z \otimes \sigma_z)$ with $|J| \ll |\omega_0|$ and prepared in random initial states $\rho_0^{(12)}$. The ergotropy gap is now

$$\Delta = \mathcal{E}^G(\rho_0^{(12)}) - (\mathcal{E}^L(\rho_0^{(1)}) + \mathcal{E}^L(\rho_0^{(2)})). \quad (4.11)$$

Our goal is to use FQErgo for estimating both local and global ergotropies and thereby obtaining the ergotropy gap. As illustrated in Fig. 4.3 (a), we use four local drives $H_\gamma^{(1)} = \sigma_\gamma \otimes \mathbf{I}$ and $H_\gamma^{(2)} = \mathbf{I} \otimes \sigma_\gamma$, where $\gamma \in [x, y]$ over the first 30 iterations that saturated the energy and reached $\rho_{30} \approx \rho^{(12)pL}$, the local passive state. From the 31st iteration, we see a further reduction in energy as we apply a combination of global and local operations, as illustrated in Fig. 4.3 (b). It involves a tilted phase gate

$$Z_\delta = e^{-i\delta(I \otimes \sigma_y)} \left[|0\rangle\langle 0| \otimes I + |1\rangle\langle 1| \otimes e^{-i\sigma_z \pi/2} \right] e^{i\delta(I \otimes \sigma_y)}$$

with a fixed small angle δ [226], local gates, as well as the global XY gate,

$$U_{xy} = e^{-i\beta^{xy} H_{xy} \tau_{xy}} \text{ with } H_{xy} = \sigma_x \otimes \sigma_y + \sigma_y \otimes \sigma_x,$$

strength β^{xy} , and duration τ_{xy} . Finally, we find the second energy saturation over 60 iterations while reaching $\rho_{60} \approx \rho^{(12)pG}$, the global passive state. Fig. 4.3 (c) shows the monotonic energy decrease for 20 random initial states undergoing FQErgo iteration. For each initial state, we observe two minimum-energy states, one corresponding to the local passive state and the other to the global passive state. Figs. 4.3 (e-f) plot the estimated local and global ergotropies against their

exact values, and Fig. 4.3 (g) plots the estimated ergotropy gaps against exact values. Indeed, one can apply global energy extraction sequence Fig. 4.3 (b) directly from initial point and reach passive state much faster but here our focus is to estimate the ergotropy gap Δ .

We again study FQErgo robustness by introducing a random nonlocal error unitary $U_{err} = e^{-iH_{err}\eta}$ generated by a random unit-norm error Hamiltonian H_{err} and $\eta \equiv 2$ degrees in every FQErgo iteration. The system-energy curves shown in Fig. 4.3 (d) lose monotonicity in decay, but retain the overall trend. The error-affected local and global ergotropy values and the corresponding ergotropy gaps are shown by filled triangles in Fig. 4.3 (e-g). Likewise in one qubit case, the ergotropy values, particularly the global ergotropy values are underestimated, but the rms deviation of the ergotropy gap estimations from the ideal values remains below 0.07 indicating reasonable robustness of FQErgo against unitary errors.

4.3.3 Speed analysis

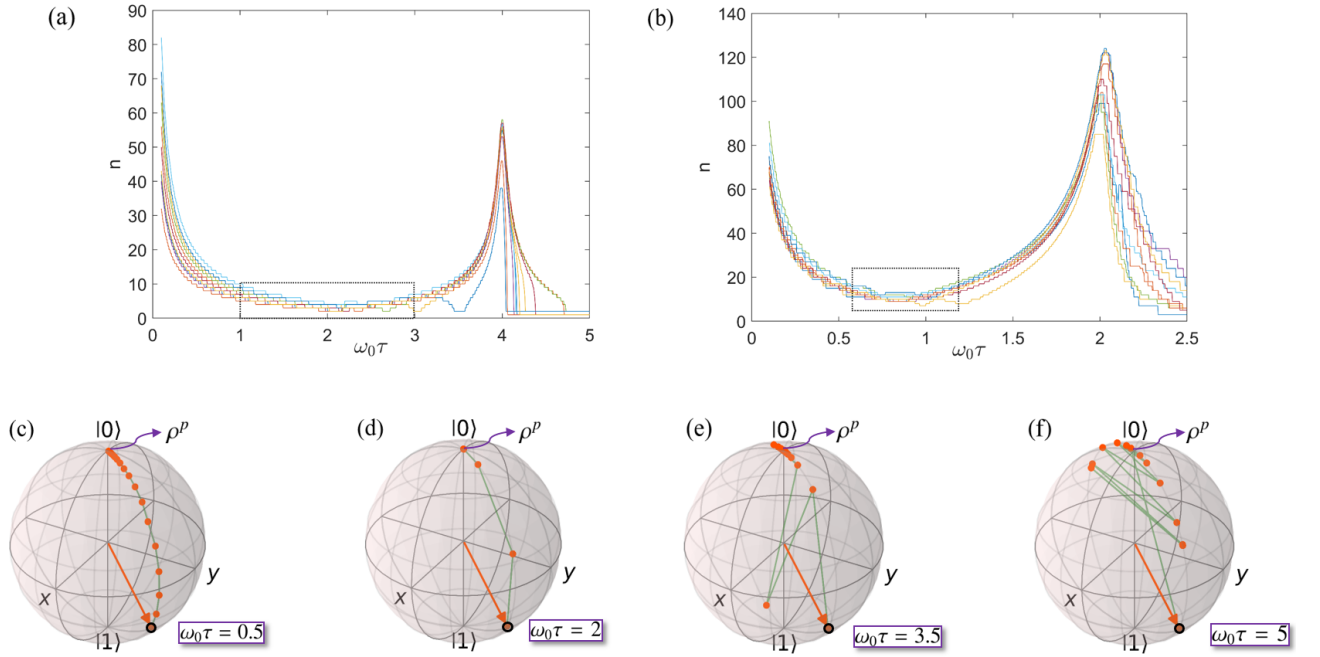


Figure 4.4: For one qubit (a) and two qubit (b), 10 arbitrary initial states are taken; these plot shows the minimum number of FQErgo iterations n required to reach the passive state v.s. $\omega_0 \tau$. (c-f) show Bloch vector evolution from initial state $|\psi\rangle = \cos(\pi/3)|0\rangle + e^{i\pi/3}\sin(\pi/3)|1\rangle$ to passive state ρ^p for different values of $\omega_0 \tau$. The area enclosed by dotted rectangles in plots (a) and (b) shows the approximate working regime for τ values to get the lowest possible FQErgo iteration, i.e., n ranges from (3, 10) for one and (6, 20) for two qubit systems.

How many feedback-iterations does FQErgo take to reach the passive state from an arbitrary initial state? Alternatively, we can ask what should be the optimal step size τ in $u_k = e^{-i\beta_k\tau H_d}$ that takes the minimum number of iterations n to reach the passive state. In the following, we describe numerical studies to gain insights into these questions. First, let us consider a one qubit system with $\omega_0 = 1$. Fig. 4.4 (a) shows the number of FQErgo iterations n vs $\omega_0\tau$ for 10 random initial states. Here we find that the optimal time-step corresponds to $\omega_0\tau$ in the range of 1 to 3. For example, consider the one-qubit initial state $|\psi\rangle = \cos(\pi/3)|0\rangle + e^{i\pi/3}\sin(\pi/3)|1\rangle$. Figs. 4.4 (c-f) illustrate Bloch vector evolutions for various step sizes τ such that $\omega_0\tau = 0.5, 2, 3.5$, and 5 respectively. Note that for $\omega_0\tau = 2$, it takes only three FQErgo iterations to reach the passive state. The behavior is similar in two qubits. Fig. 4.4 (b) shows the n vs $\omega_0\tau$ for 10 random two-qubit initial states. Here again, the optimal step is for $\omega_0\tau$ in the neighborhood of 1.

4.4 Experiments

4.4.1 Single-qubit ergotropy

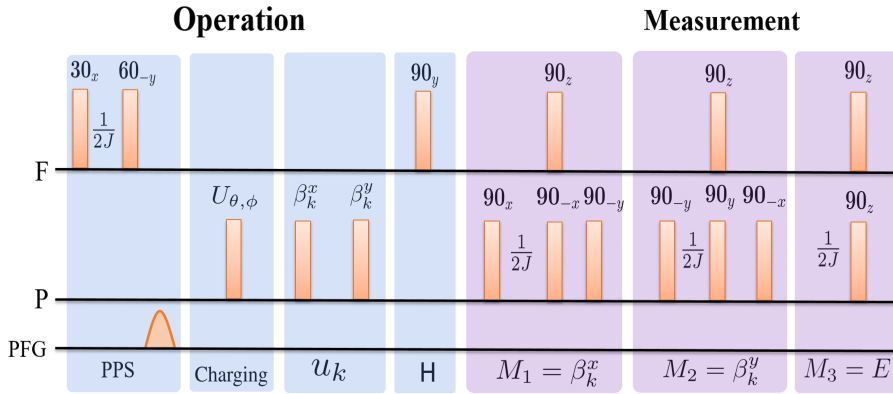


Figure 4.5: NMR pulse sequence for the 1-qubit FQErgo experiment. From thermal equilibrium state, we first prepare the $|00\rangle$ pseudopure state (PPS) which is rotated by $U_{\theta,\phi} = e^{-i\theta(I_x \cos \phi + I_y \sin \phi)}$ to realize the initial state ρ_0 . After FQErgo iterations $u_k = e^{-i\beta_k^x I_x \tau} e^{-i\beta_k^y I_y \tau}$ on the system qubit ^{31}P (only one iteration is shown) and Hadamard gate (H) on the probe, we extract (i) one of the drive amplitudes $\beta^{x(y)}$ or (ii) energy E . Here the measurement pulse-sequences implement one of $e^{-i\beta^{x(y)} I_{y(x)} \tau}$ and $e^{-iI_z \tau}$ acting on system ^{31}P qubit and controlled by ^{19}F qubit. Finally, σ_x measurements of ^{19}F qubit yields drive amplitudes $\beta^{x(y)}$ or energy E .

We now use sodium fluorophosphate (dissolved in D_2O ; Fig. 4.6(a)) as the two-qubit register, wherein ^{19}F nuclear spin is our probe qubit and ^{31}P nuclear spin is the system qubit. All

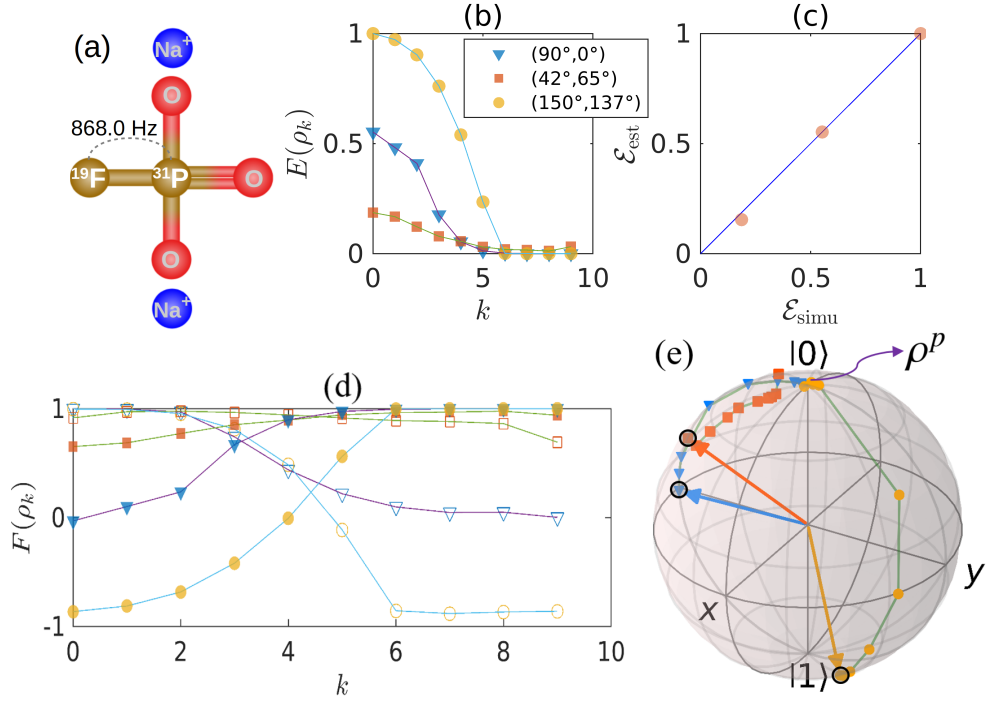


Figure 4.6: (a) Sodium fluorophosphate molecular structure with J_{FP} indicated. (b) The experimentally measured one-qubit energy (normalized) vs FQergo iterations for three initial states $\rho_{\theta,\phi} = |0\rangle\langle 0| \otimes U_{\theta,\phi}|0\rangle\langle 0|U_{\theta,\phi}^\dagger$ prepared by one of the RF rotations $U_{\theta,\phi} = e^{-i\theta(I_x \cos \phi + I_y \sin \phi)} \equiv (\theta, \phi)$ as indicated. (c) Ergotropy estimated from (b) vs simulated values. (d) Decaying fidelities of initial states ($F_0(\rho_k)$, open symbols) and corresponding growth of passive states ($F_p(\rho_k)$, filled symbols) for the same three cases as in (b). (e) Bloch sphere evolution from initial state to passive state for the same three cases.

the experiments were carried out on a 500 MHz Bruker NMR spectrometer at an ambient temperature of 300 K. The rotating frame Hamiltonian of the system consisting of the internal part and the RF drive is $H^{FP} = H_{\text{int}}^{FP} + H_{\text{RF}}^{FP}(t)$, where $H_{\text{int}}^{FP} = -\omega_F I_z^F - \omega_P I_z^P + 2\pi J_{FP} I_z^F I_z^P$ and $H_{\text{RF}}^{FP}(t) = \Omega_F(t) I_x^F + \Omega_P(t) I_x^P$, where $I_{x,y,z}$ are the spin operators. Here (ω_F, ω_P) and $(\Omega_F(t), \Omega_P(t))$ respectively denote the adjustable frequency offsets and time-dependent RF amplitudes of ^{19}F and ^{31}P spins, and $J_{FP} = 868.0$ Hz is the scalar coupling constant.

The pulse sequences for the NMR implementations of FQergo are described in Fig. 4.5. Starting from the thermal state, we prepare a pseudopure state (PPS) before energizing the system qubit ^{31}P into one of the three initial states ρ_0 as described in Fig. 4.6. For FQergo, we randomly choose the initial drives $\beta_0^x I_x$ and $\beta_0^y I_y$, and their strengths in the k th iteration are obtained by measuring the ancilla signal $\langle i[H_0, I_{x(y)}] \rangle \rho_{k-1} = \beta_k^{x(y)}$. Notice that all three different states reach their common passive state within 10 iterations in Fig. 4.6 (b). The corresponding ergotropy values show excellent agreement with the numerically simulated values in Fig. 4.6 (c), thus

demonstrating the successful implementation of FQErgo.

In this one qubit case, since we have now measured all three expectation values $\langle \sigma_{x,y,z} \rangle_{\rho_k}$, we can now reconstruct the density matrix and determine its state fidelities $F_0(\rho_k) = \text{Tr}(\rho_0 \rho_k)$ with the respective initial state, and $F_p(\rho_k) = \text{Tr}(\rho_p \rho_k)$ with the expected target passive state, at each iteration. The resulting fidelity profiles are shown in Fig. Fig. 4.6 (d). They indicate the gradual decay of the initial state fidelity and the corresponding buildup of the passive state fidelity. We clearly find high-fidelity passive states being prepared in each of the three cases.

4.4.2 Two-qubit ergotropy

To estimate two-qubit ergotropy, we use the three-spin NMR register dibromofluoromethane (dissolved in Acetone-D6; Fig. 4.8 (a)). We consider ^{13}C as the probe and ^1H , ^{19}F as the system qubits. The rotating frame Hamiltonian consisting of the internal part and the RF drive reads as $H^{\text{CHF}} = H_{\text{int}}^{\text{CHF}} + H_{\text{RF}}^{\text{CHF}}(t)$, where $H_{\text{int}}^{\text{CHF}} = -\omega_{\text{C}}I_z^{\text{C}} - \omega_{\text{H}}I_z^{\text{H}} - \omega_{\text{F}}I_z^{\text{F}} + 2\pi J_{\text{CH}}I_z^{\text{C}}I_z^{\text{H}} + 2\pi J_{\text{CF}}I_z^{\text{C}}I_z^{\text{F}} + 2\pi J_{\text{HF}}I_z^{\text{H}}I_z^{\text{F}}$ and $H_{\text{RF}}^{\text{CHF}}(t) = \Omega_{\text{C}}(t)I_x^{\text{C}} + \Omega_{\text{H}}(t)I_x^{\text{H}} + \Omega_{\text{F}}(t)I_x^{\text{F}}$. Here $(\omega_{\text{C}}, \omega_{\text{H}}, \omega_{\text{F}})$ and $(\Omega_{\text{C}}, \Omega_{\text{H}}, \Omega_{\text{F}})$, respectively denote the frequency offsets and RF amplitudes, while $(J_{\text{CH}}, J_{\text{CF}}, J_{\text{HF}})$ denote the scalar coupling constants, whose values are shown in Fig. 4.8 (a).

To demonstrate local and global ergotropy estimation, we prepare five initial states with varying degrees of entanglement between the system qubits H and F. The full NMR pulse-sequences are described in the Appendix. After preparing $|000\rangle\langle 000|$ we transform it to $|0\rangle\langle 0| \otimes \rho_0^{\text{HF}} = |0\rangle\langle 0| \otimes U_G|00\rangle\langle 00|U_G^\dagger$ using a global unitary U_G consisting of a Hadamard operator on H and a controlled $e^{-i\nu I_x}$ gate on F, where ν controls the degree of entanglement. That completes the initialization, and now we start work extraction by FQErgo. During the first 10 iterations, we extract work by using only local drives $I_{x(y)}^{\text{H}}, I_{x(y)}^{\text{F}}$ (similar as in Fig. 4.3 (a)) and realize the first energy minimization corresponding to the local passive state as shown in Fig. 4.8 (c). From 11th to 20th iterations, we extract further energy via the global drive $I_x^{\text{H}}I_y^{\text{F}} + I_y^{\text{H}}I_x^{\text{F}}$ along with the Z_δ gate and local drives as shown in Fig. 4.3 (b) and Fig. 4.7 (b). The global drive allows complete work extraction, eventually taking the system qubits to the second energy minimization corresponding to the global passive state ρ_{HF}^p . Fig. 4.8 (b) shows the normalized energies for both local and global extraction with initial states having varying entanglement entropy $S = -\text{Tr}[\rho_0^{\text{H}} \log \rho_0^{\text{H}}]$, where $\rho_0^{\text{H}} = \text{Tr}_{\text{F}}(\rho_0^{\text{HF}})$. Fig. 4.8 (c-d) plot the experimentally estimated local and global ergotropy

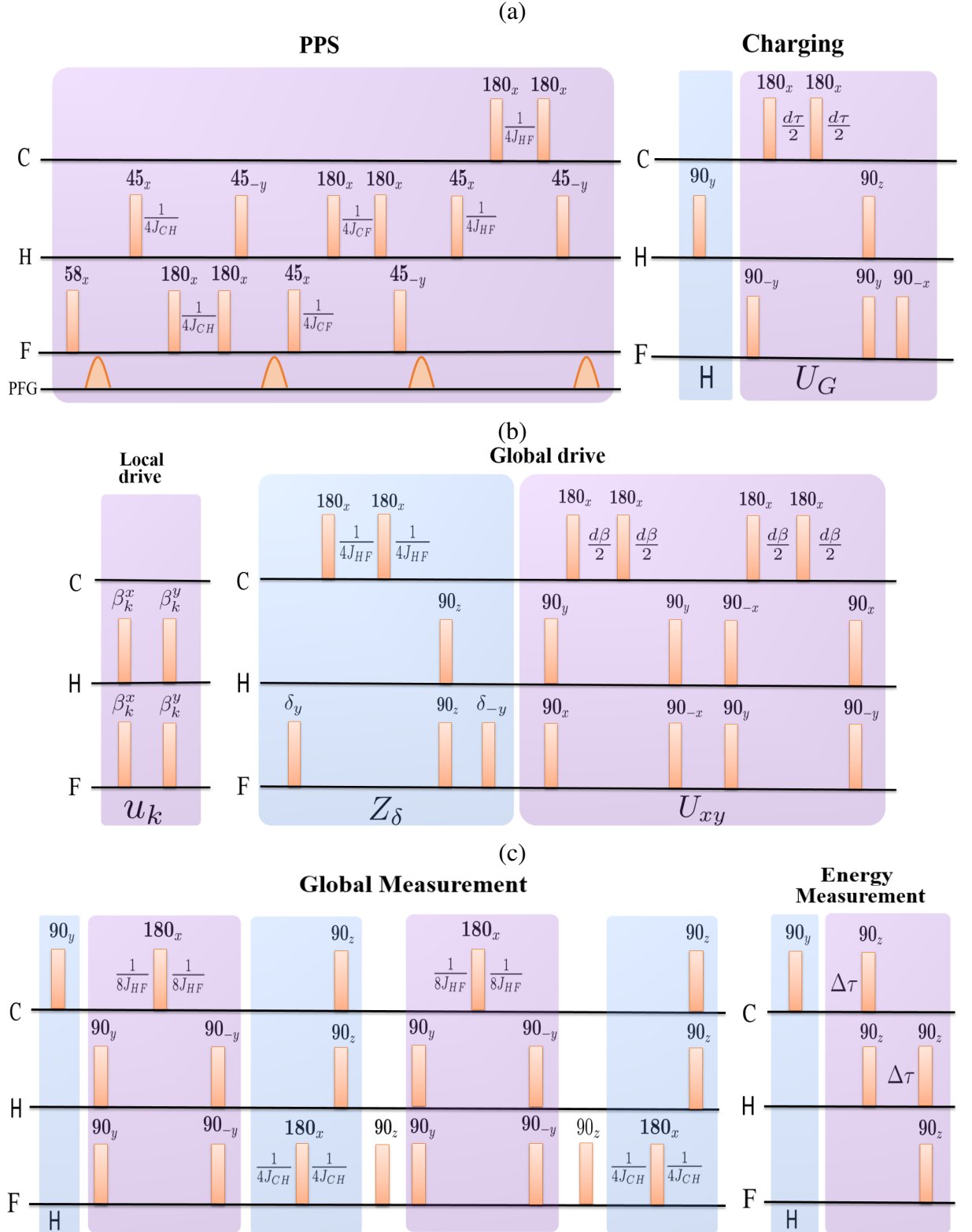


Figure 4.7: The NMR pulse sequences for 2-qubit (^1H , ^{19}F), FQErgo with one (^{13}C) probe qubit: (a) PPS preparation, initializing the system as ρ_0^{HF} using entangling unitary U_G after a pseudo-Hadamard on ^1H . Here delay $d\tau$ is varied to change entanglement entropy. (b) Local and global drives, where $\delta_y = e^{-i\delta I_y^F}$, $U_{xy} = e^{-i\beta^{xy} H_{xy} \tau_{xy}}$ and the delay $d\beta$ controls the strength of the global drive. (c) Extracting global drive strength β^{xy} and system energy.

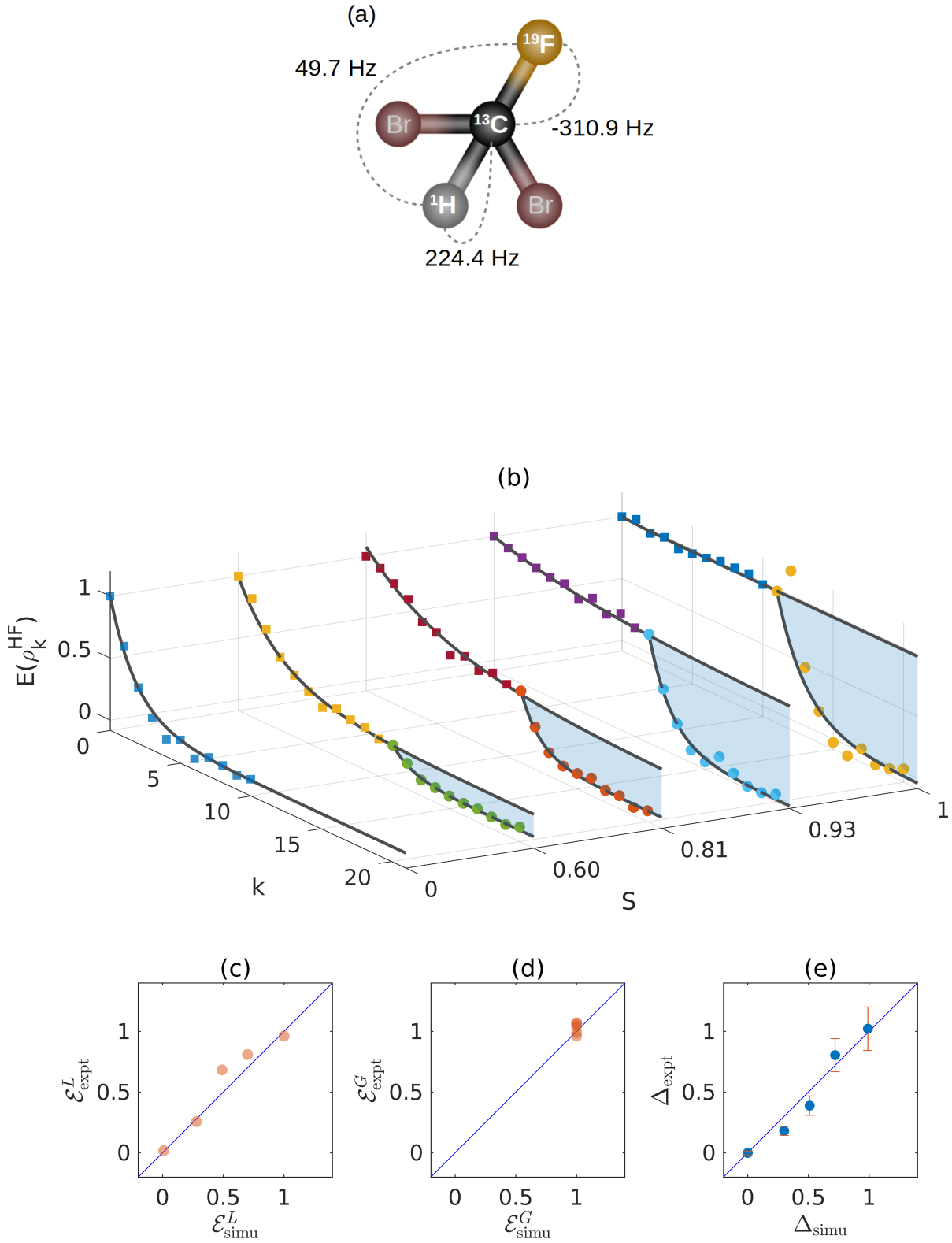


Figure 4.8: (a) Molecular structure of dibromofluoromethane, with various J couplings indicated. (b) The experimentally measured two-qubit energy (normalized) vs FQergo iterations for five initial states with varying entanglement entropy (S) as described in the text. (c,d) Local (c) and global (d) ergotropy experimentally estimated from (b) vs simulated values. (e) The experimental ergotropy gap obtained from (c,d) vs simulated values.

values vs simulated values and Fig. 4.8 (e) plots the experimentally obtained ergotropy gaps vs versus the simulated values. The good agreement between the estimated values and the simulated values confirms the successful demonstration of the FQErgo algorithm.

4.5 Summary and outlook

In summary, we have introduced a feedback-based algorithm, FQErgo to prepare the passive state and thereby quantify the ergotropy, the maximum unitarily extractable energy, of an unknown quantum state of a given system.

It is an iterative feedback algorithm that efficiently reads certain expectation values using a probe qubit and readjusts the subsequent drive strengths to extract further energy. The same probe qubit also allows regular monitoring of system energy throughout the process. By numerically implementing FQErgo over a set of random states in both one and two-qubit systems, we have verified robust passive state preparation and ergotropy estimation, even in the presence of circuit errors. We then experimentally implemented FQErgo on multiple initial states of two and three-qubit NMR registers, successfully prepared their passive states, and closely estimated their local and global ergotropies as well as the ergotropy gap.

We envisage several future directions. For instance, while ergotropy based thermodynamic quantities can form convenient entanglement witnesses, they required prior knowledge of the class of states (eg. [222]). FQErgo can overcome such limitations and pave the way to certify the entanglement for a completely unknown state. Since one probe-qubit suffices, irrespective of the system size, extending FQErgo to larger systems should be feasible without exponential complexity. The procedure for extracting work from an unknown state is crucial from the perspective of quantum batteries. Although a fully charged quantum battery may start from a known state, subsequently during storage or partial usage it may end up in an unknown state. Although the ensemble nature of NMR is advantageous here, the overall algorithm is general enough to adapt to other quantum architectures.

CHAPTER 5

Closing Remarks and Outlook

In this chapter, we conclude the thesis by summarizing key findings and discussing future research directions.

Results

In [Chapter 2](#), we investigated various aspects of quantum battery using nuclear spin systems in star-topology molecules in the context of NMR architecture. We theoretically and experimentally compared the efficiency of the collective charging scheme (involving quantum correlation) with parallel (classical) scheme and established the quantum advantage $\Gamma = \sqrt{N}$ of the collective charging scheme with N chargers. We monitored ergotropy during the whole charging dynamics experimentally, showing the amount of work available for extraction unitarily at each point of time. To avoid oscillatory charging, we proposed an asymptotic charging scheme to keep the battery in a charged steady state. Finally, we introduced a load spin to which the battery can deposit its energy after a suitable storage time, thus completing the complete charger-battery-load circuit. Using a 38-spin system, we showed that the battery spin can store energy for up to two minutes and yet was able to transfer the stored energy to the load spin.

In [Chapter 3](#), We proposed a less demanding thermodynamic criteria for entanglement certification using only energy measurements or diagonal tomography. We experimentally validate the proposed thermodynamic entanglement criterion in NMR architecture by considering particular classes of 2-qubit, 3-qubit, and 10-qubit noisy entangled states. Our method achieves certification for multi-qubit mixed states with three different bounds based on the thermodynamic quantifiers of the system. Given the entanglement class of the states, i.e., Bell diagonal, Werner, GHZ, etc., our thermodynamic approach opens up an easy avenue to certify entanglement even when the

knowledge about the state in question is not available.

In [Chapter 4](#), we introduced an all-quantum feedback-based algorithm, FQErgo which requires no classical optimization for ergotropy estimation from an unknown quantum state of a given system. By numerically implementing FQErgo over a set of arbitrary states in both one- and two-qubit systems, we have verified robust passive state preparation and ergotropy estimation, even in the presence of circuit errors. We then experimentally implemented FQErgo on multiple initial states of two and three-qubit NMR registers, successfully prepared their passive states, and closely estimated their local and global ergotropies as well as the ergotropy gap.

Future Research Directions

A. Quantum battery– In [Chapter 2](#), we experimentally verified that the quantum battery can store the charge for up to 2 minutes. We can envisage several extensions of this work. For example, if we consider a two-qubit system as a quantum battery in NMR, one can reach even longer storage time by creating the charged state as long-lived states [\[172\]](#). In this thesis, we have experimentally verified the working of the very basic quantum charger-battery load circuit. One can extend this circuit by adding quantum diodes, quantum transistors, etc., to realize a bigger circuit and pave the way to put forth a foundation of quantum electronics. It will be interesting to experimentally investigate a quantum battery in the presence of external noise [\[232\]](#).

B. Entanglement certification – There are a number of other questions for future research. For instance, generalizing our criteria discussed in [Chapter 3](#) for systems with arbitrary local dimensions and generalizing to capture more exotic kinds of entanglement, such as genuine multi-partite entanglement, would be quite important. While the local passivity in [Chapter 3](#) is studied under local unitary operations, more general notion of strong local passivity is introduced by considering more general local quantum operations [\[49, 193, 194\]](#). Obtaining entanglement certification criteria under this generic consideration could also be quite interesting. Our proposed thermodynamic quantities can also be helpful to identify the faithful signature of nonclassical correlations [\[233\]](#). In [Chapter 3](#) the entanglement cer-

tification scheme requires information on the class of the entangled states, Using FQErgo discussed in Chapter 4 for reaching passive state one can certify entanglement even without knowing the class of entangled states. Such experimental findings will create a great impact among scientific communities.

C. Feedback method– In chapter 4, we have carried out a feedback experiment to transform a quantum system in an arbitrary unknown initial state to its passive state, and thereby determined its ergotropy. In principle, this feedback method can be extended to other tasks in quantum information processing or quantum simulations.

Bibliography

- [1] Richard P Feynman. Simulating physics with computers. *International Journal of Theoretical Physics*, 21(6/7), 1982.
- [2] David Deutsch and Richard Jozsa. Rapid solution of problems by quantum computation. *Proceedings of the Royal Society of London. Series A: Mathematical and Physical Sciences*, 439(1907):553–558, 1992.
- [3] Lov K. Grover. A fast quantum mechanical algorithm for database search. In *Proceedings of the Twenty-Eighth Annual ACM Symposium on Theory of Computing*, STOC '96, page 212–219, New York, NY, USA, 1996. Association for Computing Machinery.
- [4] Charles H. Bennett and Gilles Brassard. Quantum cryptography: Public key distribution and coin tossing. *Theoretical Computer Science*, 560:7–11, 2014. Theoretical Aspects of Quantum Cryptography – celebrating 30 years of BB84.
- [5] P.W. Shor. Algorithms for quantum computation: discrete logarithms and factoring. In *Proceedings 35th Annual Symposium on Foundations of Computer Science*, pages 124–134, 1994.
- [6] David G. Cory, Amr F. Fahmy, and Timothy F. Havel. Ensemble quantum computing by nmr spectroscopy. *Proceedings of the National Academy of Sciences*, 94(5):1634–1639, 1997.
- [7] Neil A. Gershenfeld and Isaac L. Chuang. Bulk spin-resonance quantum computation. *Science*, 275(5298):350–356, 1997.
- [8] Emanuel Knill, Raymond Laflamme, and Gerald J Milburn. A scheme for efficient quantum computation with linear optics. *nature*, 409(6816):46–52, 2001.
- [9] Jeremy L. O’Brien. Optical quantum computing. *Science*, 318(5856):1567–1570, 2007.

- [10] Pieter Kok, W. J. Munro, Kae Nemoto, T. C. Ralph, Jonathan P. Dowling, and G. J. Milburn. Linear optical quantum computing with photonic qubits. *Rev. Mod. Phys.*, 79:135–174, Jan 2007.
- [11] Stefanie Barz. Quantum computing with photons: introduction to the circuit model, the one-way quantum computer, and the fundamental principles of photonic experiments. 48(8):083001, mar 2015.
- [12] D. Jaksch and P. Zoller. The cold atom hubbard toolbox. *Annals of Physics*, 315(1):52–79, 2005. Special Issue.
- [13] Maciej Lewenstein, Anna Sanpera, Veronica Ahufinger, Bogdan Damski, Aditi Sen(De), and Ujjwal Sen. Ultracold atomic gases in optical lattices: mimicking condensed matter physics and beyond. *Advances in Physics*, 56(2):243–379, 2007.
- [14] Immanuel Bloch, Jean Dalibard, and Sylvain Nascimbene. Quantum simulations with ultracold quantum gases. *Nature Physics*, 8(4):267–276, 2012.
- [15] Daniel Loss and David P. DiVincenzo. Quantum computation with quantum dots. *Phys. Rev. A*, 57:120–126, Jan 1998.
- [16] Guido Burkard, Hans-Andreas Engel, and Daniel Loss. Spintronics and quantum dots for quantum computing and quantum communication. *Fortschritte der Physik*, 48(9-11):965–986.
- [17] Christoph Kloeffer and Daniel Loss. Prospects for spin-based quantum computing in quantum dots. *Annual Review of Condensed Matter Physics*, 4(1):51–81, 2013.
- [18] J. I. Cirac and P. Zoller. Quantum computations with cold trapped ions. *Phys. Rev. Lett.*, 74:4091–4094, May 1995.
- [19] Colin D Bruzewicz, John Chiaverini, Robert McConnell, and Jeremy M Sage. Trapped-ion quantum computing: Progress and challenges. *Applied Physics Reviews*, 6(2):021314, 2019.

- [20] Yasunobu Nakamura, Yu A Pashkin, and JS Tsai. Coherent control of macroscopic quantum states in a single-cooper-pair box. *nature*, 398(6730):786–788, 1999.
- [21] G Wendin. Quantum information processing with superconducting circuits: a review. *Reports on Progress in Physics*, 80(10):106001, sep 2017.
- [22] Ibm, the quantum experience.
- [23] Frank Arute, Kunal Arya, Ryan Babbush, Dave Bacon, Joseph C Bardin, Rami Barends, Rupak Biswas, Sergio Boixo, Fernando GSL Brandao, David A Buell, et al. Quantum supremacy using a programmable superconducting processor. *Nature*, 574(7779):505–510, 2019.
- [24] D-wave systems.
- [25] Ionq, trapped ion quantum computing.
- [26] Rigetti computing: Quantum computing.
- [27] Psiquantum: fault tolerant quantum computing.
- [28] Michael A. Nielsen and Isaac L. Chuang. *Quantum Computation and Quantum Information: 10th Anniversary Edition*. Cambridge University Press, 2010.
- [29] Oleg Kupervasser. Chapter 3 - principal paradoxes of quantum mechanics. In Oleg Kupervasser, editor, *Application of New Cybernetics in Physics*, pages 73 – 120. Elsevier, Amsterdam, 2017.
- [30] Ryszard Horodecki, Paweł Horodecki, Michał Horodecki, and Karol Horodecki. Quantum entanglement. *Rev. Mod. Phys.*, 81:865–942, Jun 2009.
- [31] Gerardo Adesso, Thomas R Bromley, and Marco Cianciaruso. Measures and applications of quantum correlations. *Journal of Physics A: Mathematical and Theoretical*, 49(47):473001, 2016.
- [32] Charles H. Bennett, David P. DiVincenzo, Christopher A. Fuchs, Tal Mor, Eric Rains, Peter W. Shor, John A. Smolin, and William K. Wootters. Quantum nonlocality without entanglement. *Phys. Rev. A*, 59:1070–1091, Feb 1999.

- [33] J. Niset and N. J. Cerf. Multipartite nonlocality without entanglement in many dimensions. *Phys. Rev. A*, 74:052103, Nov 2006.
- [34] B. P. Lanyon, M. Barbieri, M. P. Almeida, and A. G. White. Experimental quantum computing without entanglement. *Phys. Rev. Lett.*, 101:200501, Nov 2008.
- [35] Kavan Modi, Aharon Brodutch, Hugo Cable, Tomasz Paterek, and Vlatko Vedral. The classical-quantum boundary for correlations: Discord and related measures. *Rev. Mod. Phys.*, 84:1655–1707, Nov 2012.
- [36] T. S. Mahesh, C. S. Sudheer Kumar, and Udaysinh T. Bhosale. *Quantum Correlations in NMR Systems*, pages 499–516. Springer International Publishing, Cham, 2017.
- [37] Harold Ollivier and Wojciech H Zurek. Quantum discord: a measure of the quantumness of correlations. *Physical review letters*, 88(1):017901, 2001.
- [38] Hemant Katiyar, Soumya Singha Roy, T. S Mahesh, and Apoorva Patel. Evolution of quantum discord and its stability in two-qubit nmr systems. *Physical Review A*, 86(1):012309, 2012.
- [39] Martin B. Plenio and S. Virmani. An introduction to entanglement measures. 2005.
- [40] Asher Peres. Separability criterion for density matrices. *Phys. Rev. Lett.*, 77:1413–1415, Aug 1996.
- [41] G. Vidal and R. F. Werner. Computable measure of entanglement. *Phys. Rev. A*, 65:032314, Feb 2002.
- [42] Armen E Allahverdyan, Roger Balian, and Th M Nieuwenhuizen. Maximal work extraction from finite quantum systems. *EPL (Europhysics Letters)*, 67(4):565, 2004.
- [43] Wiesław Pusz and Stanisław L Woronowicz. Passive states and kms states for general quantum systems. *Communications in Mathematical Physics*, 58(3):273–290, 1978.
- [44] AW Marshall. Inequalities: Theory of majorization and its applications, 1979.
- [45] LD Landau and EM Lifshitz. Statistical physics, 2nd revised and enl. ed. translated from the russian by jb sykes and m. j. kearsley oxford, 1978.

- [46] W. Pusz and S. L. Woronowicz. Passive states and KMS states for general quantum systems. *Commun. Math. Phys.*, 58(3):273–290, October 1978.
- [47] M. Perarnau-Llobet, K. V. Hovhannisyanyan, M. Huber, P. Skrzypczyk, N. Brunner, and A. Acín. Extractable work from correlations. *Phys. Rev. X*, 5:041011, Oct 2015.
- [48] Robert Alicki and Mark Fannes. Entanglement boost for extractable work from ensembles of quantum batteries. *Physical Review E*, 87(4):042123, 2013.
- [49] M. Frey, K. Funo, and M. Hotta. Strong local passivity in finite quantum systems. *Phys. Rev. E*, 90:012127, Jul 2014.
- [50] Anatole Abragam. *The principles of nuclear magnetism*. Number 32. Oxford university press, 1961.
- [51] J. Cavanagh, W. J. Fairbrother, A. G. Palmer III, and N. J. Skelton. *Protein NMR spectroscopy: principles and practice*. Elsevier, 1995.
- [52] M. H. Levitt. *Spin dynamics: basics of nuclear magnetic resonance*. John Wiley and Sons, 2001.
- [53] Charles P Slichter. *Principles of magnetic resonance*, volume 1. Springer Science & Business Media, 2013.
- [54] E. Knill and R. Laflamme. Power of one bit of quantum information. *Phys. Rev. Lett.*, 81:5672–5675, Dec 1998.
- [55] Ivan Oliveira, Roberto Sarthour Jr, Tito Bonagamba, Eduardo Azevedo, and Jair CC Freitas. *NMR quantum information processing*. Elsevier, 2011.
- [56] D.G. Cory, R. Laflamme, E. Knill, L. Viola, T.F. Havel, N. Boulant, G. Boutis, E. Fortunato, S. Lloyd, R. Martinez, C. Negrevergne, M. Pravia, Y. Sharf, G. Teklemariam, Y.S. Weinstein, and W.H. Zurek. Nmr based quantum information processing: Achievements and prospects. *Fortschritte der Physik*, 48(9-11):875–907, 2000.

- [57] Abhishek Shukla, Manvendra Sharma, and T.S. Mahesh. Noon states in star-topology spin-systems: Applications in diffusion studies and rf inhomogeneity mapping. *Chemical Physics Letters*, 592:227–231, 2014.
- [58] Deepak Khurana, V. R. Krithika, and T. S. Mahesh. Unambiguous measurement of information scrambling in a hierarchical star-topology system, 2019.
- [59] T S Mahesh, Deepak Khurana, V R Krithika, G J Sreejith, and C S Sudheer Kumar. Star-topology registers: Nmr and quantum information perspectives. *Journal of Physics: Condensed Matter*, 33(38):383002, jul 2021.
- [60] David P. DiVincenzo. The physical implementation of quantum computation. *Fortschritte der Physik*, 48(9-11):771–783, 2000.
- [61] E. Knill, I. Chuang, and R. Laflamme. Effective pure states for bulk quantum computation. *Phys. Rev. A*, 57:3348–3363, May 1998.
- [62] Soumya Singha Roy and T.S. Mahesh. Density matrix tomography of singlet states. *Journal of Magnetic Resonance*, 206(1):127–133, 2010.
- [63] Abhishek Shukla, K. Rama Koteswara Rao, and T. S. Mahesh. Ancilla-assisted quantum state tomography in multiqubit registers. *Phys. Rev. A*, 87:062317, Jun 2013.
- [64] Michael A Nielsen and Isaac Chuang. Quantum computation and quantum information, 2002.
- [65] Hoi-Kwong Lo, Tim Spiller, and Sandu Popescu. *Introduction to quantum computation and information*. World Scientific, 1998.
- [66] Hai-Tao Quan, Yu-xi Liu, Chang-Pu Sun, and Franco Nori. Quantum thermodynamic cycles and quantum heat engines. *Physical Review E*, 76(3):031105, 2007.
- [67] Himangshu Prabal Goswami and Upendra Harbola. Thermodynamics of quantum heat engines. *Physical Review A*, 88(1):013842, 2013.
- [68] Carmen Palacios-Berraquero. Atomically-thin quantum light emitting diodes. In *Quantum Confined Excitons in 2-Dimensional Materials*, pages 71–89. Springer, 2018.

- [69] Shuji Nakamura, Masayuki Senoh, Shin-ichi Nagahama, Naruhito Iwasa, Takao Yamada, Toshio Matsushita, Hiroyuki Kiyoku, and Yasunobu Sugimoto. Ingan-based multi-quantum-well-structure laser diodes. *Japanese Journal of Applied Physics*, 35(1B):L74, 1996.
- [70] Linda Geppert. Quantum transistors: toward nanoelectronics. *IEEE Spectrum*, 37(9):46–51, 2000.
- [71] Gian Marcello Andolina, Donato Farina, Andrea Mari, Vittorio Pellegrini, Vittorio Giovannetti, and Marco Polini. Charger-mediated energy transfer in exactly solvable models for quantum batteries. *Physical Review B*, 98(20):205423, 2018.
- [72] Gian Marcello Andolina, Maximilian Keck, Andrea Mari, Michele Campisi, Vittorio Giovannetti, and Marco Polini. Extractable work, the role of correlations, and asymptotic freedom in quantum batteries. *Physical review letters*, 122(4):047702, 2019.
- [73] Johan Åberg. Truly work-like work extraction via a single-shot analysis. *Nature communications*, 4(1):1–5, 2013.
- [74] Felix C Binder, Sai Vinjanampathy, Kavan Modi, and John Goold. Quantacell: powerful charging of quantum batteries. *New Journal of Physics*, 17(7):075015, 2015.
- [75] Francesco Campaioli, Felix A Pollock, Felix C Binder, Lucas Céleri, John Goold, Sai Vinjanampathy, and Kavan Modi. Enhancing the charging power of quantum batteries. *Physical review letters*, 118(15):150601, 2017.
- [76] Dario Ferraro, Michele Campisi, Gian Marcello Andolina, Vittorio Pellegrini, and Marco Polini. High-power collective charging of a solid-state quantum battery. *Physical review letters*, 120(11):117702, 2018.
- [77] Gian Marcello Andolina, Maximilian Keck, Andrea Mari, Vittorio Giovannetti, and Marco Polini. Quantum versus classical many-body batteries. *Physical Review B*, 99(20):205437, 2019.
- [78] Francesco Campaioli, Felix A. Pollock, and Sai Vinjanampathy. Quantum batteries - review chapter, 2018.

- [79] Sai Vinjanampathy and Janet Anders. Quantum thermodynamics. *Contemporary Physics*, 57(4):545–579, Jul 2016.
- [80] Ronnie Kosloff. Quantum thermodynamics: A dynamical viewpoint. *Entropy*, 15(6):2100–2128, 2013.
- [81] Sebastian Deffner and Steve Campbell. *Quantum Thermodynamics: An introduction to the thermodynamics of quantum information*. Morgan & Claypool Publishers, 2019.
- [82] FH Kamin, FT Tabesh, S Salimi, and Alan C Santos. Entanglement, coherence, and charging process of quantum batteries. *Physical Review E*, 102(5):052109, 2020.
- [83] Juliette Monsel, Marco Fellous-Asiani, Benjamin Huard, and Alexia Auffèves. The energetic cost of work extraction. *Physical review letters*, 124(13):130601, 2020.
- [84] FH Kamin, FT Tabesh, S Salimi, F Kheirandish, and Alan C Santos. Non-markovian effects on charging and self-discharging process of quantum batteries. *New Journal of Physics*, 22(8):083007, 2020.
- [85] Faezeh Pirmoradian and Klaus Mølmer. Aging of a quantum battery. *Physical Review A*, 100(4):043833, 2019.
- [86] Xiang Zhang et al. Enhanced energy transfer in a dicke quantum battery. *arXiv preprint arXiv:1812.10139*, 2018.
- [87] A Crescente, M Carrega, M Sassetti, and D Ferraro. Charging and energy fluctuations of a driven quantum battery. *New Journal of Physics*, 22(6):063057, 2020.
- [88] Sergi Julià-Farré, Tymoteusz Salamon, Arnau Riera, Manabendra N Bera, and Maciej Lewenstein. Bounds on the capacity and power of quantum batteries. *Physical Review Research*, 2(2):023113, 2020.
- [89] Brij Mohan and Arun K Pati. Reverse quantum speed limit: How slowly a quantum battery can discharge. *Physical Review A*, 104(4):042209, 2021.

- [90] Wolfgang Niedenzu, Victor Mukherjee, Arnab Ghosh, Abraham G Kofman, and Gershon Kurizki. Quantum engine efficiency bound beyond the second law of thermodynamics. *Nature communications*, 9(1):1–13, 2018.
- [91] Francesco Caravelli, Ghislaine Coulter-De Wit, Luis Pedro García-Pintos, and Alioscia Hama. Random quantum batteries. *Physical Review Research*, 2(2):023095, 2020.
- [92] Thao P Le, Jesper Levinsen, Kavan Modi, Meera M Parish, and Felix A Pollock. Spin-chain model of a many-body quantum battery. *Physical Review A*, 97(2):022106, 2018.
- [93] Srijon Ghosh, Titas Chanda, Aditi Sen, et al. Enhancement in the performance of a quantum battery by ordered and disordered interactions. *Physical Review A*, 101(3):032115, 2020.
- [94] Fang Zhao, Fu-Quan Dou, and Qing Zhao. Quantum battery of interacting spins with environmental noise. *Phys. Rev. A*, 103:033715, Mar 2021.
- [95] Davide Rossini, Gian Marcello Andolina, and Marco Polini. Many-body localized quantum batteries. *Physical Review B*, 100(11):115142, 2019.
- [96] Shadab Zakavati, Fatemeh T Tabesh, and Shahriar Salimi. Bounds on charging power of open quantum batteries. *Physical Review E*, 104(5):054117, 2021.
- [97] Srijon Ghosh, Titas Chanda, Shiladitya Mal, Aditi Sen, et al. Fast charging of a quantum battery assisted by noise. *Physical Review A*, 104(3):032207, 2021.
- [98] Alan C Santos, Andreia Saguia, and Marcelo S Sarandy. Stable and charge-switchable quantum batteries. *Physical Review E*, 101(6):062114, 2020.
- [99] Davide Rossini, Gian Marcello Andolina, Dario Rosa, Matteo Carrega, and Marco Polini. Quantum advantage in the charging process of sachdev-ye-kitaev batteries. *Physical Review Letters*, 125(23):236402, 2020.
- [100] Dario Rosa, Davide Rossini, Gian Marcello Andolina, Marco Polini, and Matteo Carrega. Ultra-stable charging of fast-scrambling syk quantum batteries. *Journal of High Energy Physics*, 2020(11):1–29, 2020.

- [101] Yu-Yu Zhang, Tian-Ran Yang, Libin Fu, and Xiaoguang Wang. Powerful harmonic charging in a quantum battery. *Physical Review E*, 99(5):052106, 2019.
- [102] Jie Chen, Liyao Zhan, Lei Shao, Xingyu Zhang, Yuyu Zhang, and Xiaoguang Wang. Charging quantum batteries with a general harmonic driving field. *Annalen der Physik*, 532(4):1900487, 2020.
- [103] JQ Quach, KE McGhee, Lucia Ganzer, DM Rouse, BW Lovett, EM Gauger, Jonathan Keeling, Giulio Cerullo, DG Lidzey, and Tersilla Virgili. An organic quantum battery. *arXiv preprint arXiv:2012.06026*, 2020.
- [104] T S Mahesh, Deepak Khurana, V R Krithika, G J Sreejith, and C S Sudheer Kumar. Star-topology registers: NMR and quantum information perspectives. *Journal of Physics: Condensed Matter*, 33(38):383002, jul 2021.
- [105] Varad R Pande, Gaurav Bhole, Deepak Khurana, and TS Mahesh. Strong algorithmic cooling in large star-topology quantum registers. *Physical Review A*, 96(1):012330, 2017.
- [106] Hans Georg Krojanski and Dieter Suter. Reduced decoherence in large quantum registers. *Physical review letters*, 97(15):150503, 2006.
- [107] Alan C Santos, Barış Çakmak, Steve Campbell, and Nikolaj T Zinner. Stable adiabatic quantum batteries. *Physical Review E*, 100(3):032107, 2019.
- [108] Fu-Quan Dou, Yuan-Jin Wang, and Jian-An Sun. Highly efficient charging and discharging of three-level quantum batteries through shortcuts to adiabaticity. *Frontiers of Physics*, 17(3):1–9, 2022.
- [109] Alan C Santos. Quantum advantage of two-level batteries in the self-discharging process. *Physical Review E*, 103(4):042118, 2021.
- [110] Jia-Xuan Liu, Hai-Long Shi, Yun-Hao Shi, Xiao-Hui Wang, and Wen-Li Yang. Entanglement and work extraction in the central-spin quantum battery. *Phys. Rev. B*, 104:245418, Dec 2021.

- [111] J. Cavanagh, W. J. Fairbrother, A. G. Palmer III, and N. J. Skelton. *Protein NMR spectroscopy: principles and practice*. Academic press, 1996.
- [112] Daniel Manzano. A short introduction to the lindblad master equation. *AIP Advances*, 10(2):025106, 2020.
- [113] Matteo Carrega, Alba Crescente, Dario Ferraro, and Maura Sassetti. Dissipative dynamics of an open quantum battery. *New Journal of Physics*, 22(8):083085, 2020.
- [114] Ahmed A Zahia, MY Abd-Rabbou, and Ahmed M Megahed. Entanglement-driven energy exchange in a two-qubit quantum battery. *Journal of Physics B: Atomic, Molecular and Optical Physics*, 58(6):065501, 2025.
- [115] Andrea Canzio, Vasco Cavina, Marco Polini, and Vittorio Giovannetti. Single-atom dissipation and dephasing in dicke and tavis-cummings quantum batteries. *Physical Review A*, 111(2):022222, 2025.
- [116] Javier Carrasco, Jerónimo R Maze, Carla Hermann-Avigliano, and Felipe Barra. Collective enhancement in dissipative quantum batteries. *Physical Review E*, 105(6):064119, 2022.
- [117] Borhan Ahmadi, Paweł Mazurek, Shabir Barzanjeh, and Paweł Horodecki. Superoptimal charging of quantum batteries via reservoir engineering: Arbitrary energy transfer unlocked. *Physical Review Applied*, 23(2):024010, 2025.
- [118] A. Einstein, B. Podolsky, and N. Rosen. Can quantum-mechanical description of physical reality be considered complete? *Phys. Rev.*, 47:777–780, May 1935.
- [119] N. Bohr. Can quantum-mechanical description of physical reality be considered complete? *Phys. Rev.*, 48:696–702, Oct 1935.
- [120] E. Schrödinger. Probability relations between separated systems. *Math. Proc. Cambridge Philos. Soc.*, 32(3):446–452, October 1936.
- [121] J. S. Bell. On the problem of hidden variables in quantum mechanics. *Rev. Mod. Phys.*, 38:447–452, Jul 1966.

- [122] A. K. Ekert. Quantum cryptography based on bell’s theorem. *Phys. Rev. Lett.*, 67:661–663, Aug 1991.
- [123] C. H. Bennett and S. J. Wiesner. Communication via one- and two-particle operators on einstein-podolsky-rosen states. *Phys. Rev. Lett.*, 69:2881–2884, Nov 1992.
- [124] C. H. Bennett, G. Brassard, C. Crépeau, R. Jozsa, A. Peres, and W. K. Wootters. Teleporting an unknown quantum state via dual classical and einstein-podolsky-rosen channels. *Phys. Rev. Lett.*, 70:1895–1899, Mar 1993.
- [125] D. Deutsch. Quantum theory, the church–turing principle and the universal quantum computer. *Proc. Math. Phys. Eng. Sci.*, 400(1818):97–117, July 1985.
- [126] B. Yurke. Input states for enhancement of fermion interferometer sensitivity. *Phys. Rev. Lett.*, 56:1515–1517, Apr 1986.
- [127] V. Giovannetti, S. Lloyd, and L. Maccone. Quantum-enhanced measurements: Beating the standard quantum limit. *Science*, 306(5700):1330–1336, November 2004.
- [128] Yi Xia, Aman R. Agrawal, Christian M. Pluchar, Anthony J. Brady, Zhen Liu, Quntao Zhuang, Dalziel J. Wilson, and Zheshen Zhang. Entanglement-enhanced optomechanical sensing. *Nature Photonics*, April 2023.
- [129] R. Horodecki, P. Horodecki, M. Horodecki, and K. Horodecki. Quantum entanglement. *Rev. Mod. Phys.*, 81:865–942, Jun 2009.
- [130] W. Dür, G. Vidal, and J. I. Cirac. Three qubits can be entangled in two inequivalent ways. *Phys. Rev. A*, 62:062314, Nov 2000.
- [131] F. Verstraete, J. Dehaene, B. De Moor, and H. Verschelde. Four qubits can be entangled in nine different ways. *Phys. Rev. A*, 65:052112, Apr 2002.
- [132] J. I. Cirac, P. Zoller, H. J. Kimble, and H. Mabuchi. Quantum state transfer and entanglement distribution among distant nodes in a quantum network. *Phys. Rev. Lett.*, 78:3221–3224, Apr 1997.

- [133] R. Raussendorf and H. J. Briegel. A one-way quantum computer. *Phys. Rev. Lett.*, 86:5188–5191, May 2001.
- [134] P. Arrighi and L. Salvail. Blind quantum computation. *Int. J. Quantum Inf.*, 04(05):883–898, October 2006.
- [135] H. J. Kimble. The quantum internet. *Nature*, 453(7198):1023–1030, June 2008.
- [136] S. Wehner, D. Elkouss, and R. Hanson. Quantum internet: A vision for the road ahead. *Science*, 362(6412):eaam9288, October 2018.
- [137] S. Agrawal, S. Halder, and M. Banik. Genuinely entangled subspace with all-encompassing distillable entanglement across every bipartition. *Phys. Rev. A*, 99:032335, Mar 2019.
- [138] S. Saha, S. S. Bhattacharya, T. Guha, S. Halder, and M. Banik. Advantage of quantum theory over nonclassical models of communication. *Annalen der Physik*, 532(12):2000334, November 2020.
- [139] S. Rout, A. G. Maity, A. Mukherjee, S. Halder, and M. Banik. Multiparty orthogonal product states with minimal genuine nonlocality. *Phys. Rev. A*, 104:052433, Nov 2021.
- [140] M. Banik, T. Guha, M. Alimuddin, G. Kar, S. Halder, and S. S. Bhattacharya. Multicopy adaptive local discrimination: Strongest possible two-qubit nonlocal bases. *Phys. Rev. Lett.*, 126:210505, May 2021.
- [141] S. S. Bhattacharya, A. G. Maity, T. Guha, G. Chiribella, and M. Banik. Random-receiver quantum communication. *PRX Quantum*, 2:020350, Jun 2021.
- [142] L. Gurvits. Classical deterministic complexity of edmonds' problem and quantum entanglement. In *Proceedings of the thirty-fifth annual ACM symposium on Theory of computing*. ACM, June 2003.
- [143] Michał Horodecki, Paweł Horodecki, and Ryszard Horodecki. Separability of mixed states: necessary and sufficient conditions. *Physics Letters A*, 223(1-2):1–8, November 1996.

- [144] B. Dirkse, M. Pompili, R. Hanson, M. Walter, and S. Wehner. Witnessing entanglement in experiments with correlated noise. *Quantum Sci. Technol.*, 5(3):035007, May 2020.
- [145] C. H. Bennett, D. P. DiVincenzo, J. A. Smolin, and W. K. Wootters. Mixed-state entanglement and quantum error correction. *Phys. Rev. A*, 54:3824–3851, Nov 1996.
- [146] Igor Devetak and Andreas Winter. Distillation of secret key and entanglement from quantum states. *Proc. R. Soc. A: Math. Phys. Eng. Sc.*, 461(2053):207–235, January 2005.
- [147] A. Mukherjee, A. Roy, S. S. Bhattacharya, and M. Banik. Presence of quantum correlations results in a nonvanishing ergotropic gap. *Phys. Rev. E*, 93:052140, May 2016.
- [148] M. Alimuddin, T. Guha, and P. Parashar. Bound on ergotropic gap for bipartite separable states. *Phys. Rev. A*, 99:052320, May 2019.
- [149] M. Alimuddin, T. Guha, and P. Parashar. Independence of work and entropy for equal-energetic finite quantum systems: Passive-state energy as an entanglement quantifier. *Phys. Rev. E*, 102:012145, Jul 2020.
- [150] M. Alimuddin, T. Guha, and P. Parashar. Structure of passive states and its implication in charging quantum batteries. *Phys. Rev. E*, 102:022106, Aug 2020.
- [151] S. Puliylil, M. Banik, and M. Alimuddin. Thermodynamic signatures of genuinely multipartite entanglement. *Phys. Rev. Lett.*, 129:070601, Aug 2022.
- [152] X. Yang, Y. H. Yang, M. Alimuddin, R. Salvia, S. M. Fei, L. M. Zhao, S. Nimmrichter, and M. X. Luo. The battery capacity of energy-storing quantum systems. *arXiv:2302.09905*, 2023.
- [153] A. E Allahverdyan, R Balian, and Th. M Nieuwenhuizen. Maximal work extraction from finite quantum systems. *Europhysics Letters (EPL)*, 67(4):565–571, August 2004.
- [154] J. A. Jones, S. D. Karlen, J. Fitzsimons, A. Ardavan, S. C. Benjamin, G. A. D. Briggs, and J. J. L. Morton. Magnetic field sensing beyond the standard quantum limit using 10-spin NOON states. *Science*, 324(5931):1166–1168, May 2009.

- [155] TS Mahesh, Deepak Khurana, CS Kumar, et al. Star-topology registers: Nmr and quantum information perspectives. *arXiv preprint arXiv:2102.05203*, 2021.
- [156] A. Shukla, M. Sharma, and T.S. Mahesh. NOON states in star-topology spin-systems: Applications in diffusion studies and RF inhomogeneity mapping. *Chem. Phys. Lett.*, 592:227–231, January 2014.
- [157] A. W. Marshall, I. Olkin, and B. C. Arnold. *Inequalities: Theory of Majorization and its Applications*, volume 143. Springer, second edition, 2011.
- [158] M. A. Nielsen and J. Kempe. Separable states are more disordered globally than locally. *Phys. Rev. Lett.*, 86:5184–5187, May 2001.
- [159] M. A. Nielsen. Conditions for a class of entanglement transformations. *Phys. Rev. Lett.*, 83:436–439, Jul 1999.
- [160] M. Horodecki, P. Horodecki, and J. Oppenheim. Reversible transformations from pure to mixed states and the unique measure of information. *Phys. Rev. A*, 67:062104, Jun 2003.
- [161] A. Winter and D. Yang. Operational resource theory of coherence. *Phys. Rev. Lett.*, 116:120404, Mar 2016.
- [162] M. Horodecki and J. Oppenheim. Fundamental limitations for quantum and nanoscale thermodynamics. *Nature communications*, 4(1):2059, 2013.
- [163] W. Dür and J. I. Cirac. Classification of multiqubit mixed states: Separability and distillability properties. *Phys. Rev. A*, 61:042314, Mar 2000.
- [164] O. Gühne and M. Seevinck. Separability criteria for genuine multiparticle entanglement. *New J. Phys.*, 12(5):053002, may 2010.
- [165] A. Lenard. Thermodynamical proof of the gibbs formula for elementary quantum systems. *J. Stat. Phys.*, 19(6):575–586, December 1978.
- [166] J. Åberg. Truly work-like work extraction via a single-shot analysis. *Nat. Commun.*, 4(1):1925, June 2013.

- [167] P. Skrzypczyk, A. J. Short, and S. Popescu. Work extraction and thermodynamics for individual quantum systems. *Nat. Commun.*, 5(1), June 2014.
- [168] P. Skrzypczyk, R. Silva, and N. Brunner. Passivity, complete passivity, and virtual temperatures. *Phys. Rev. E*, 91:052133, May 2015.
- [169] J. Joshi and T. S. Mahesh. Experimental investigation of a quantum battery using star-topology nmr spin systems. *Phys. Rev. A*, 106:042601, Oct 2022.
- [170] David G. Cory, Amr F. Fahmy, and Timothy F. Havel. Ensemble quantum computing by NMR spectroscopy. *Proc. Natl. Acad. Sci.*, 94(5):1634–1639, March 1997.
- [171] S. S. Roy and T.S. Mahesh. Density matrix tomography of singlet states. *J. Magn. Reson.*, 206(1):127–133, September 2010.
- [172] M. Carravetta and M. H. Levitt. Long-lived nuclear spin states in high-field solution NMR. *J. Am. Chem. Soc.*, 126(20):6228–6229, May 2004.
- [173] VR Krithika, S. Pal, R. Nath, and TS Mahesh. Observation of interaction induced blockade and local spin freezing in a nmr quantum simulator. *Phys. Rev. Research*, 3(3):033035, 2021.
- [174] J. M. Raimond, M. Brune, and S. Haroche. Manipulating quantum entanglement with atoms and photons in a cavity. *Rev. Mod. Phys.*, 73:565–582, Aug 2001.
- [175] P. Kok, W. J. Munro, K. Nemoto, T. C. Ralph, J. P. Dowling, and G. J. Milburn. Linear optical quantum computing with photonic qubits. *Rev. Mod. Phys.*, 79:135–174, Jan 2007.
- [176] D. Lu, A. Brodutch, J. Park, H. Katiyar, T. Jochym-O’Connor, and R. Laflamme. Nmr quantum information processing, 2015.
- [177] Z-L Xiang, S Ashhab, J. Q. You, and F. Nori. Hybrid quantum circuits: Superconducting circuits interacting with other quantum systems. *Rev. Mod. Phys.*, 85:623–653, Apr 2013.
- [178] A. Aspect, P. Grangier, and G. Roger. Experimental tests of realistic local theories via bell’s theorem. *Phys. Rev. Lett.*, 47:460–463, Aug 1981.

- [179] A. Aspect, J. Dalibard, and G. Roger. Experimental test of bell’s inequalities using time-varying analyzers. *Phys. Rev. Lett.*, 49:1804–1807, Dec 1982.
- [180] A. Aspect, P. Grangier, and G. Roger. Experimental realization of einstein-podolsky-rosen-bohm gedankenexperiment: A new violation of bell’s inequalities. *Phys. Rev. Lett.*, 49:91–94, Jul 1982.
- [181] D. Bouwmeester, J-W Pan, M. Daniell, H. Weinfurter, and A. Zeilinger. Observation of three-photon greenberger-horne-zeilinger entanglement. *Phys. Rev. Lett.*, 82:1345–1349, Feb 1999.
- [182] J-W Pan, D. Bouwmeester, M.Daniell, H. Weinfurter, and A. Zeilinger. Experimental test of quantum nonlocality in three-photon greenberger–horne–zeilinger entanglement. *Nature*, 403(6769):515–519, February 2000.
- [183] Z. Zhao, T. Yang, Y-A Chen, A-N Zhang, M. Żukowski, and J-W Pan. Experimental violation of local realism by four-photon greenberger-horne-zeilinger entanglement. *Phys. Rev. Lett.*, 91:180401, Oct 2003.
- [184] M-C Chen, D Wu, Z-E Su, X-D Cai, X-L Wang, T. Yang, L. Li, N-L Liu, C-Y Lu, and J-W Pan. Efficient measurement of multiparticle entanglement with embedding quantum simulator. *Phys. Rev. Lett.*, 116:070502, Feb 2016.
- [185] J. C. Loredó, M. P. Almeida, R. Di Candia, J. S. Pedernales, J. Casanova, E. Solano, and A. G. White. Measuring entanglement in a photonic embedding quantum simulator. *Phys. Rev. Lett.*, 116:070503, Feb 2016.
- [186] A. Singh, K. Dorai, and Arvind. Experimentally identifying the entanglement class of pure tripartite states. *Quan. Inf. Process.*, 17(12), oct 2018.
- [187] S. Xue, Y. Huang, D. Zhao, C. Wei, J. Li, Y. Dong, J. Gao, D. Lu, T. Xin, and Gui-Lu Long. Experimental measurement of bipartite entanglement using parameterized quantum circuits. *Sci. China Phys. Mech. Astron.*, 65(8):280312, 2022.

- [188] T. Xie, Z. Zhao, X. Kong, W. Ma, M. Wang, X. Ye, P. Yu, Z. Yang, S. Xu, P. Wang, Y. Wang, F. Shi, and J. Du. Beating the standard quantum limit under ambient conditions with solid-state spins. *Sci. Adv.*, 7(32):eabg9204, August 2021.
- [189] G. M. Andolina, M. Keck, A. Mari, M. Campisi, V. Giovannetti, and M. Polini. Extractable work, the role of correlations, and asymptotic freedom in quantum batteries. *Phys. Rev. Lett.*, 122:047702, Feb 2019.
- [190] G. Francica, F. C. Binder, G. Guarnieri, M. T. Mitchison, J. Goold, and F. Plastina. Quantum coherence and ergotropy. *Phys. Rev. Lett.*, 125:180603, Oct 2020.
- [191] S. Tirone, R. Salvia, and V. Giovannetti. Quantum energy lines and the optimal output ergotropy problem. *Phys. Rev. Lett.*, 127:210601, Nov 2021.
- [192] D. Šafránek, D. Rosa, and F. C. Binder. Work extraction from unknown quantum sources. *Phys. Rev. Lett.*, 130:210401, May 2023.
- [193] Á. M. Alhambra, G. Styliaris, N. A. Rodríguez-Briones, J. Sikora, and E. Martín-Martínez. Fundamental limitations to local energy extraction in quantum systems. *Phys. Rev. Lett.*, 123:190601, Nov 2019.
- [194] N. A. Rodríguez-Briones, H. Katiyar, E. Martín-Martínez, and R. Laflamme. Experimental activation of strong local passive states with quantum information. *Phys. Rev. Lett.*, 130:110801, Mar 2023.
- [195] Ronnie Kosloff and Amikam Levy. Quantum heat engines and refrigerators: Continuous devices. *Annual Review of Physical Chemistry*, 65:365–393, 2014.
- [196] Mark T Mitchison. Quantum thermal absorption machines: refrigerators, engines and clocks. *Contemporary Physics*, 60(2):164–187, 2019.
- [197] Karen V Hovhannisyanyan, Martí Perarnau-Llobet, Marcus Huber, and Antonio Acín. Entanglement generation is not necessary for optimal work extraction. *Physical review letters*, 111(24):240401, 2013.

- [198] RR Rodriguez, Borhan Ahmadi, Gerardo Suárez, Paweł Mazurek, S Barzanjeh, and Paweł Horodecki. Optimal quantum control of charging quantum batteries. *New Journal of Physics*, 26(4):043004, 2024.
- [199] Chang-Kang Hu, Jiawei Qiu, Paulo JP Souza, Jiahao Yuan, Yuxuan Zhou, Libo Zhang, Ji Chu, Xianchuang Pan, Ling Hu, Jian Li, et al. Optimal charging of a superconducting quantum battery. *Quantum Science and Technology*, 7(4):045018, 2022.
- [200] Tanoy Kanti Konar, Leela Ganesh Chandra Lakkaraju, Srijon Ghosh, and Aditi Sen. Quantum battery with ultracold atoms: Bosons versus fermions. *Physical Review A*, 106(2):022618, 2022.
- [201] Felipe Barra, Karen V Hovhannisyan, and Alberto Imparato. Quantum batteries at the verge of a phase transition. *New Journal of Physics*, 24(1):015003, 2022.
- [202] Francesco Campaioli, Stefano Gherardini, James Q Quach, Marco Polini, and Gian Marcello Andolina. Colloquium: quantum batteries. *Reviews of Modern Physics*, 96(3):031001, 2024.
- [203] Lei Gao, Chen Cheng, Wen-Bin He, Rubem Mondaini, Xi-Wen Guan, and Hai-Qing Lin. Scaling of energy and power in a large quantum battery-charger model. *Physical Review Research*, 4(4):043150, 2022.
- [204] Ju-Yeon Gyhm, Dominik Šafránek, and Dario Rosa. Quantum charging advantage cannot be extensive without global operations. *Physical Review Letters*, 128(14):140501, 2022.
- [205] Raffaele Salvia, Martí Perarnau-Llobet, Géraldine Haack, Nicolas Brunner, and Stefan Nimmrichter. Quantum advantage in charging cavity and spin batteries by repeated interactions. *Physical Review Research*, 5(1):013155, 2023.
- [206] Ricard Ravell Rodriguez, Borhan Ahmadi, Paweł Mazurek, Shabir Barzanjeh, Robert Al-icki, and Paweł Horodecki. Catalysis in charging quantum batteries. *Physical Review A*, 107(4):042419, 2023.

- [207] Salvatore Tirone, Raffaele Salvia, Stefano Chessa, and Vittorio Giovannetti. Work extraction processes from noisy quantum batteries: The role of nonlocal resources. *Physical Review Letters*, 131(6):060402, 2023.
- [208] Jia-Xuan Liu, Hai-Long Shi, Yun-Hao Shi, Xiao-Hui Wang, and Wen-Li Yang. Entanglement and work extraction in the central-spin quantum battery. *Physical Review B*, 104(24):245418, 2021.
- [209] Paranjoy Chaki, Aparajita Bhattacharyya, Kornikar Sen, and Ujjwal Sen. Positive and non-positive measurements in energy extraction from quantum batteries, 2024.
- [210] Paranjoy Chaki, Aparajita Bhattacharyya, Kornikar Sen, and Ujjwal Sen. Auxiliary-assisted stochastic energy extraction from quantum batteries, 2023.
- [211] John Goold, Marcus Huber, Arnau Riera, Lídia Del Rio, and Paul Skrzypczyk. The role of quantum information in thermodynamics—a topical review. *Journal of Physics A: Mathematical and Theoretical*, 49(14):143001, 2016.
- [212] Manabendra N Bera, Arnau Riera, Maciej Lewenstein, and Andreas Winter. Generalized laws of thermodynamics in the presence of correlations. *Nature communications*, 8(1):2180, 2017.
- [213] Gonzalo Manzano, Francesco Plastina, and Roberta Zambrini. Optimal work extraction and thermodynamics of quantum measurements and correlations. *Physical Review Letters*, 121(12):120602, 2018.
- [214] Giuseppe Vitagliano, Claude Klöckl, Marcus Huber, and Nicolai Friis. Trade-off between work and correlations in quantum thermodynamics. *Thermodynamics in the Quantum Regime: Fundamental Aspects and New Directions*, pages 731–750, 2018.
- [215] Giulia Gemme, Michele Grossi, Dario Ferraro, Sofia Vallecorsa, and Maura Sassetti. Ibm quantum platforms: A quantum battery perspective. *Batteries*, 8(5):43, 2022.
- [216] Fu-Quan Dou, Hang Zhou, and Jian-An Sun. Cavity heisenberg-spin-chain quantum battery. *Physical Review A*, 106(3):032212, 2022.

- [217] Fu-Quan Dou, You-Qi Lu, Yuan-Jin Wang, and Jian-An Sun. Extended dicke quantum battery with interatomic interactions and driving field. *Physical Review B*, 105(11):115405, 2022.
- [218] Fu-Quan Dou and Fang-Mei Yang. Superconducting transmon qubit-resonator quantum battery. *Physical Review A*, 107(2):023725, 2023.
- [219] Mir Alimuddin, Tamal Guha, and Preeti Parashar. Bound on ergotropic gap for bipartite separable states. *Phys. Rev. A*, 99:052320, May 2019.
- [220] Xue Yang, Yan-Han Yang, Shao-Ming Fei, and Ming-Xing Luo. Multiparticle entanglement classification with the ergotropic gap. *Phys. Rev. A*, 109:062427, Jun 2024.
- [221] Samgeeth Puliyl, Manik Banik, and Mir Alimuddin. Thermodynamic signatures of genuinely multipartite entanglement. *Phys. Rev. Lett.*, 129:070601, Aug 2022.
- [222] Jitendra Joshi, Mir Alimuddin, T. S. Mahesh, and Manik Banik. Experimental verification of many-body entanglement using thermodynamic quantities. *Phys. Rev. A*, 109:L020403, Feb 2024.
- [223] Alicia B. Magann, Kenneth M. Rudinger, Matthew D. Grace, and Mohan Sarovar. Feedback-based quantum optimization. *Phys. Rev. Lett.*, 129:250502, Dec 2022.
- [224] Sen Kuang and Shuang Cong. Lyapunov control methods of closed quantum systems. *Automatica*, 44(1):98–108, 2008.
- [225] Shao-Chen Hou, MA Khan, XX Yi, Daoyi Dong, and Ian R Petersen. Optimal lyapunov-based quantum control for quantum systems. *Physical Review A—Atomic, Molecular, and Optical Physics*, 86(2):022321, 2012.
- [226] Duc Tuan Hoang, Friederike Metz, Andreas Thomasen, Tran Duong Anh-Tai, Thomas Busch, and Thom  s Fogarty. Variational quantum algorithm for ergotropy estimation in quantum many-body batteries. *Phys. Rev. Res.*, 6:013038, Jan 2024.
- [227] Dominik   afr  nek, Dario Rosa, and Felix C. Binder. Work extraction from unknown quantum sources. *Phys. Rev. Lett.*, 130:210401, May 2023.

- [228] Osama Moussa, Colm A Ryan, David G Cory, and Raymond Laflamme. Testing contextuality on quantum ensembles with one clean qubit. *Physical review letters*, 104(16):160501, 2010.
- [229] Sharad Joshi, Abhishek Shukla, Hemant Katiyar, Anirban Hazra, and T. S. Mahesh. Estimating franck-condon factors using an nmr quantum processor. *Phys. Rev. A*, 90:022303, Aug 2014.
- [230] TS Mahesh, Abhishek Shukla, Swathi S Hegde, CS Kumar, Hemant Katiyar, Sharad Joshi, and KR Rao. Ancilla assisted measurements on quantum ensembles: General protocols and applications in nmr quantum information processing. *arXiv preprint arXiv:1509.04506*, 2015.
- [231] Martí Perarnau-Llobet, Karen V. Hovhannisyan, Marcus Huber, Paul Skrzypczyk, Nicolas Brunner, and Antonio Acín. Extractable work from correlations. *Phys. Rev. X*, 5:041011, Oct 2015.
- [232] Rahul Shastri, Chao Jiang, Guo-Hua Xu, B Prasanna Venkatesh, and Gentaro Watanabe. Dephasing enabled fast charging of quantum batteries. *arXiv preprint arXiv:2402.16999*, 2024.
- [233] Mir Alimuddin, Snehasish Roy Chowdhury, Ram Krishna Patra, Subhendu B Ghosh, Tommaso Tufarelli, Gerardo Adesso, and Manik Banik. Nonlocal locking of observable quantities: A faithful signature of nonclassical correlations. *arXiv preprint arXiv:2407.08292*, 2024.